Developing a Permanent Magnet Zeeman Slower and Investigating the Background Scattering Effect on Efimov Scenarios

Fatema Hamodi-Gzal
Department of Physics

Ph.D. Thesis

Submitted to the Senate of Bar-Ilan University

Ramat-Gan, Israel May 30, 2024

This work was carried out under the supervision of

Prof. Lev Khaykovich

Department of Physics,
Bar-Ilan University.

The Outcome of This Work

The work presented in the current thesis has resulted in the following outcomes:

- Paper: "Effect of Background Scattering on Efimov Scenario for Overlapping Narrow Feshbach Resonances." Fatema Hamodi-Gzal, Lev Khaykovich, submitted to Few-Body Systems journal (2024).
- Paper: "Spin-Flip Transverse Field Zeeman Slower for ^{7}Li Based on Permanent Magnets", Fatema Hamodi-Gzal, Roy Elbaz, Majdi Gzal and Lev Khaykovich, in preparation (2024).

Contents

Abstract **i**

1 Introduction and Motivation **1**

I Transverse Field Zeeman Slower for ^{7}Li Based on Permanent Magnets 5

2 Laser Cooling and Trapping of Atoms **6**
- 2.1 Spontaneous Force 6
- 2.2 Doppler Cooling 7
- 2.3 Zeeman Shift 9
- 2.4 Zeeman Slower 10
- 2.5 Magneto-Optical Trap 13

3 Overview of Lithium Experimental Setup and Key Considerations **16**
- 3.1 Experimental Setup Overview 17
- 3.2 ^{7}Li Level Structure & Properties 17
- 3.3 Li Oven: Velocity Distribution 19
- 3.4 Loading Rate 20

4 Permanent Magnets Zeeman Slower (PMZS): Design & Simulation **23**
- 4.1 Magnetic Field of Cuboid Permanent Magnets 23
- 4.2 Spatial Arrangement of Permanent Magnets 26
- 4.3 Magnetic Field Calculation of the PMZS 29
- 4.4 Optimization Procedure for the PMZS 31
- 4.5 Simulated Magnetic Field Parameters 33
- 4.6 Ideal Magnetic Field Parameters 34
- 4.7 Optimization Results 35
- 4.8 Analysis of Magnetic Field Profiles in the PMZS: Simulated vs. Ideal Comparisons 37

5 Constructing the PMZS: Mechanical Design and Resulting Magnetic Field Measurements **40**
- 5.1 Mechanical Design 40
- 5.2 Tolerable Measured Magnetic Field Deviations 46
- 5.3 Comparison of Measured and Simulated Magnetic Field Profiles in the PMZS 47

6 Testing and characterization of the PMZS: Monte-Carlo Simulation **50**
- 6.1 Numerical Solution Along the Z Axis 52
- 6.2 General Numerical Solution (3D Motion Considered) 54

7 Zeeman Slower Performance: Velocity Measurements 56
7.1 Optical Density . . . 56
7.2 Measurement Apparatus . . . 57
7.3 Measurement Results . . . 59

8 Magneto-optical trap (MOT) 62
8.1 Exact Field of a Circular Current Loop . . . 62
8.2 Anti-Helmholtz Coil Configuration . . . 62
8.3 MOT Design . . . 63

II Influence of Background Scattering on Efimov Scenario for Two Overlapping Feshbach Resonances 66

9 Resonant Regimes in Few-Body Physics 67
9.1 Feshbach Resonances . . . 67
9.2 Efimov Resonances . . . 69
9.3 Two-Channel Model . . . 70

10 Three-Channel Model 74
10.1 Phenomenology of Three-Channel Model . . . 74
10.2 Hamiltonian . . . 74
10.3 Two-Body Sector . . . 75
10.4 Three-Body Sector: Efimov Trimers . . . 77

11 Two-Channel Model with background Scattering 79
11.1 Hamiltonian . . . 79
11.2 Two-Body Sector . . . 80
11.3 Three-Body Sector: Efimov Trimers . . . 82

12 Two-Channel Model with background Scattering Versus Three-Channel Model 85
12.1 Definition of Model Systems . . . 85
12.2 Approximation of the Model Systems by the 2CMbg . . . 87
12.3 Two-Body Sector . . . 88
12.4 Three-Body Sector . . . 89

13 Three-Channel Model with background Scattering 91
13.1 Hamiltonian . . . 91
13.2 Two-Body Sector . . . 92
13.3 Three-Body Sector: Efimov Trimers . . . 94

14 Efimov Scenario in Bosonic Lithium 96
14.1 ^{7}Li *bb*-Channel . . . 96
14.2 ^{7}Li *aa*-Channel . . . 99

15 Summary & Conclusions 101

Bibliography 103

Hebrew Abstract א

List of Figures

2.1 A two-level atom under red-detuned counter-propagating laser beams in different reference frames 7
2.2 Formation of optical molasses by spontaneous force from counterpropagating laser beams 8
2.3 Zeeman slower types 13
2.4 A simple 1-dimensional model of a magneto-optical trap with a single ground state and triplet split excited states 14
2.5 Principle of the Magneto-optical trap 15

3.1 Lithium experimental design from different views. 16
3.2 Energy level diagram for ^{7}Li 18
3.3 Lithium evaporation oven design 19
3.4 Distribution functions of ^{7}Li atoms leaving the oven 20
3.5 Trajectory of the atoms 21

4.1 Cuboid magnet 23
4.2 Schematic representation of the Halbach configuration 25
4.3 Magnetic field produced by permanent magnets 25
4.4 Transverse cross section of an 8-pole Halbach configuration 27
4.5 Magnets design parameters 27
4.6 Illustration of R_{n+1} calculation 28
4.7 Illustration of Z_{n+1} calculation 29
4.8 Conceptual representation of the initial design 32
4.9 Two views of permanent magnets design 37
4.10 Simulated magnetic field vs ideal magnetic field 39
4.11 Deviation between simulated and ideal magnetic fields 39

5.1 3D model of the total assembly of the PMZS 41
5.2 Upper and lower sub-assemblies of the PMZS 41
5.3 Side holder assembly of the PMZS 42
5.4 Assembly of magnets holder type I 43
5.5 Exploded isometric view of magnets holder type I 44
5.6 Assembly of magnets holder type II 44
5.7 Exploded isometric view of magnets holder type II 44
5.8 Photograph of magnet holder assembly 45
5.9 Photograph of total assembly of the PMZS 45
5.10 Simulated magnetic field vs Measured magnetic field 47
5.11 Deviation between simulated and measured magnetic fields 48

6.1 Velocity vs. z coordinate with simulated magnetic field, assuming on-axis motion . . . 52
6.2 Velocity vs. z coordinates with interpolated magnetic field function, assuming on-axis motion . . . 53
6.3 Random initial velocity v_x, v_y . . . 54
6.4 Velocity vs. z coordinate with simulated magnetic field (3D motion considered) . . . 54

7.1 The measurement apparatus . . . 58
7.2 Measurement example . . . 59
7.3 Transition of the slowing laser beam . . . 61
7.4 Optical density as function of velocity . . . 61

8.1 Magnetic field of a single circular current loop . . . 63
8.2 Magneto optical trap . . . 64
8.3 Variation of the magnetic field B_z across the Z-axis in the MOT . . . 65
8.4 Gradient of the magnetic field along the Z-axis in the MOT . . . 65

9.1 Basic two-channel model of a magnetically tunable Feshbach resonance. 67
9.2 Feshbach resonance properties . . . 68
9.3 Efimov energy spectrum . . . 70

10.1 Depiction of the three-body sector involving overlapping Feshbach resonances . . . 75

12.1 Two-body sectors of the NB and BN models . . . 86
12.2 Three-body binding energies for the NB and BN models . . . 90

14.1 Two-body sector of ^{7}Li *bb*-channel . . . 97
14.2 The position of the Efimov resonances for the ^{7}Li *bb*-channel . . . 98
14.3 Two-body sector of ^{7}Li *aa*-channel . . . 100
14.4 ^{7}Li *aa*-channel: variation of a_- . . . 100

List of Tables

4.1 Radial and axial coordinates for the Halbach rings 30
4.2 Zeeman slower design parameters 36
4.3 Geometric arrangement parameters for the PMZS 38

12.1 Parameters of the NB and BN model systems 85
12.2 2CMbg parameters obtained from the fit to the 3CM binding energies for two model systems 88

14.1 Fitting parameters of the ^{7}Li coupled-channel calculations. 98
14.2 Bare parameters of the 3CMBg for ^{7}Li *bb*- and *aa*-channels. 98

List of Acronyms

2CM Two-Channel Model

2CMbg Two-Channel Model with background

2D/3D Two/Three Dimensional

3CM Three-Channel Model

3CMbg Three-Channel Model with background

BN Broad Narrow

MOT Magneto Optical Trap

NB Narrow Broad

OD Optical Density

PBS Polarizing Beam Splitter

PMZS Permanent Magnet Zeeman Slower

Res Resonance

Abstract

The current thesis is divided into two main parts, each dedicated to exploring different aspects of ultracold atomic gas research. The first part describes the development of a new experimental setup for producing and studying ultracold atomic gases of bosonic lithium. This work primarily involves constructing and optimizing a transverse field Zeeman slower that utilizes permanent magnets, as well as designing a magneto-optical trap (MOT). The second part focuses on investigating the effect of background scattering on the Efimov scenario in the context of overlapping narrow Feshbach resonances.

The first part details the innovative design, optimization, and assembly of a spin-flip Zeeman slower that employs permanent magnets, a pivotal component in the production and study of ultracold atomic gases. Traditional methods of decelerating atomic beams for cooling and trapping often rely on electrically powered, wire-wound configurations that require continuous water cooling. Our approach diverges by utilizing a permanent magnet-based Zeeman slower, eliminating the need for electrical power and water cooling, thereby simplifying the operational complexity and maintenance requirements. The proposed design facilitates vacuum maintenance by allowing easy assembly and disassembly of the Zeeman slower.

Focusing on ^{7}Li atoms, the developed spin-flip Zeeman slower is capable of efficiently reducing the velocity of a hot atomic beam from several hundreds meters per second to tens of meters per second. This significant reduction in speed enhances the loading efficiency and maximizes the achievable atom number within a magneto-optical trap (MOT). The adoption of a Halbach configuration for the magnets ensures a smooth magnetic field. The overall magnetic field can be fine-tuned by the strategic addition of Halbach rings around the Zeeman slower if necessary.

A key advantage of our approach is providing a stable and adjustable magnetic field, for operating the slower near theoretical deceleration limits. This results in a more compact and efficient system. Utilizing 3D printing technology for the construction of the Zeeman slower, we present a cost-effective solution that can be readily adapted by other research groups for various cold-atom experiments. Our novel use of permanent magnets also paves the way for future advancements in creating highly uniform and stable magnetic fields around a science chamber, achieving a remarkable stability of less than 1 mG within a field strength of 850 Gauss.

Sharing our mechanical design and insights, we aim to facilitate broader research endeavors in the field, enhancing the understanding and application of permanent magnet-based systems for ultracold atomic studies. Additionally, this work extends to the design and optimization of a magneto-optical trap (MOT).

The second part deals with theoretical modeling of the Efimov physics in the vicinity of two overlapping narrow Feshbach resonances, which can be explored within the framework of a three-channel model where a non-interacting open channel is coupled to two closed molecular channels. Here, we determine how it compares to the extended two-channel model, which includes an open channel with finite background scattering and a single molecular channel. We identify the parameter range in which the three-channel model surpasses the extended two-channel model. Furthermore, the three-channel model is extended to include background scattering, and then both models are applied to the experimentally relevant system of bosonic lithium atoms polarized on two different energy levels, with an isolated and two overlapping narrow Feshbach resonances, respectively. We confirm, in agreement with previous studies, that being small, the background scattering length in lithium has a negligible effect on the Efimov features in the case of isolated resonance. However, in the case of overlapping Feshbach resonances, the inclusion of background scattering improves the performance of the theory with respect to the experimentally measured position of the Efimov resonance.

Chapter 1

Introduction and Motivation

First Part

Ultra-cold atoms are a very useful physical platform for many areas of research, such as atomic clocks, precision metrology, quantum simulation, quantum chemistry, quantum entanglement, Bose-Hubbard physics, matter wave solitons, and Efimov physics [1–6] are only a few of a long list of different research fields.

An essential first step in the production of these ultra-cold atomic gases is rapid loading of a magneto-optical trap (MOT) followed by an evaporative cooling step in a magnetic or optical dipole trap allowing the quantum degeneracy regime to be reached. During evaporation, a very large fraction of the atoms initially trapped are lost. It is therefore essential that the cloud captured by the magneto-optical trap contains enough atoms so that the condensate has an appreciable size. The MOT loading time can be dramatically reduced, and much larger MOT atom numbers can be reached by adding a separate source of pre-cooled atoms; this is done in general by adding 2D MOT or Zeeman slower.

Zeeman slowers are a popular widely used technology. It uses a position-dependent magnetic field to shift the energy levels of the atom to compensate for the Doppler shift, so the atoms remain in resonance with the laser and continue to be slowed. In most cases Zeeman slowers are made using currents running in wires, where numerous coils with differing numbers of turns of wire create a spatially varying axial magnetic field. Such slowers often require significant currents and therefore large power supply, which causes heating that necessitates using a water cooling to regulate the temperature. However, this could introduce noise into the atom sample. In addition, the field profile can be difficult to tune, and the coil windings fully enclose the atomic beam tube, restricting both optical access and the ability to remove the slower from the vacuum apparatus without disassembly.

To overcome these constraints, designs based on permanent magnets have recently been suggested and implemented [7–14].

Permanent magnet Zeeman slower (PMZS) designs do not require a power source or cooling water, do not heat the chamber (which can lead to vacuum degradation), and can be easily attached and removed without breaking the vacuum of the experimental enclosure. They offer robustness, ease of maintenance, tunability (which can be achieved by adding or subtracting individual magnetic elements), no perturbations, low cost, and, above all, provide a very smooth and homogeneous magnetic field profile.

PMZS can be classified on the basis of the direction of the magnetic field relative to the beam axis, either longitudinal or transverse, which depends on the positioning of the magnets.

In this thesis, we examine a transversal spin-flip Zeeman slower for ^{7}Li atoms utilizing a Halbach configuration. We provide a comprehensive analysis of the Zeeman slower, its optimization process, detailed mechanical design, and its performance. We chose spin-flip Zeeman slower, or zero crossing design, due to its advantages, which will be emphasized later in this thesis. It is worth mentioning that no design similar to ours has been found in any publications, making our design potentially the first of its kind to be suggested. We believe that such designs have not been proposed mainly due to two reasons. First, from the laser system's perspective, as mentioned in [15], lithium has an essential splitting of the ground state, thus a transverse Zeeman slower prevents it from optically pumping atoms to the correct (slowed) magnetic substate in the region where the magnetic field turns to zero, leading to a loss of decelerated atoms in that region. This issue was resolved and is explained in detail in the chapter on Zeeman performance. The second challenge arises because lithium is a very light atom, causing it to reach very high thermal velocities. To slow it down, a very high amplitude as well as a high magnetic field gradient are needed, which makes the design challenging. This issue will also be explained in detail later in the thesis.

Second Part

In this part we theoretically consider the Efimov scenario in the vicinity of two overlapping narrow Feshbach resonances. Magnetic Feshbach resonances are one of the most salient features underlying ultracold collisions [16]. Intuitively, they can be understood within a simple two-channel model. Consider a pair of atoms that interact in an open channel at such a low kinetic energy that their scattering is fully described by the s-wave scattering length a. If a closed channel with a nearly degenerate bound state is coupled to the open channel, the scattering length is resonantly enhanced. The relative energy between the closed and open channels is tuned by the external magnetic field, and the functional form of $a(B)$ assumes the following form [16]:

$$a = a_{bg}\left(1 - \frac{\Delta B}{B - B^{(res)}}\right), \tag{1.1}$$

where a_{bg} represents the off-resonant background scattering length, and ΔB indicates the magnetic field interval between the position of the resonance $B^{(res)}$ and $a = 0$ (the resonance width).

Ultracold atoms exhibiting Feshbach resonances have opened a new avenue for studying the universal spectrum of three-body Efimov states. This effect was first proposed by Efimov in the context of nuclear physics [17], and predicts that near-resonant two-body interactions induce an infinite ladder of three-body bound states separated by a universal scaling factor. Consequently, a single three-body parameter determines the entire three-body spectrum. The three-body parameter is often determined by the scattering length value $a_-^{(0)}$ at which the lowest Efimov trimer state meets the three-body continuum and leads to an Efimov resonance. Extensive experimental efforts across many ultracold atomic species have focused on measuring $a_-^{(0)}$ and mapping the Efimov spectrum [18–20].

The basic phenomenology of an isolated s-wave Feshbach resonance and Efimov-related physics can be described within the framework of a two-channel model. In its simplest form, an open channel with no background scattering ($a_{bg} = 0$) is coupled to a closed channel that can be fine-tuned by a magnetic-field-dependent binding energy level [21]. Although $a_{bg} = 0$ leads to the absence of the magnetic field at which $a = 0$, Eq. (1.1) remains valid because when $a_{bg} \to 0$, the resonance width $\Delta B \to \infty$ such that $\Delta = a_{bg}\Delta B$ remains finite. The two-channel model has been intensively studied in the past, and various few- and many-body scenarios in bosonic and fermionic gases have been investigated within its framework [22–27]. The model can be extended to include background scattering in the open channel [28–30], thus reintroducing the $a = 0$ condition and improving its performance in the low scattering length limit.

The two-channel model remains a simplified framework for a generally multi-channel two-body scattering problem. For example, a frequently occurring situation of overlapping Feshbach resonances is already beyond the scope of the two-channel model. Detailed incorporation of all possible channels in different theoretical approaches usually leads to heavy numerical calculations [31–38]. In contrast, the simplest way to extend the phenomenology of the two-channel model to three channels has been suggested in [39] and successfully applied to the Efimov scenario of two overlapping Feshbach resonances in ^{6}Li-^{133}Cs mixture [40]. Although an open channel with no interaction is used in this model, an additional close channel regenerates the $a = 0$ limit between the overlapping resonances and improves the performance of the model [39].

A direct question which arises from these studies is to what extent the results of the three-channel model can be reproduced by those of the two-channel model extended to include the background scattering. In what limits does the three-channel model go beyond the latter? Here, we investigate these questions by directly comparing the results of both approaches. We identify the region where the three-channel model surpasses the performance of the extended two-channel model. Moreover, we generalize the three-channel model to include the background scattering and apply it to the relevant scenario in lithium atoms.

Part I

Transverse Field Zeeman Slower for ^{7}Li Based on Permanent Magnets

Chapter 2

Laser Cooling and Trapping of Atoms

Investigating the cooling and control of atomic particles reveals a deep engagement with the interplay between light and matter. This intricate dance is driven primarily by two forces: the dipole force, which emerges from the coherent absorption and stimulated emission of photons, and the scattering force, derived from spontaneous emission events. This chapter offers a concise review of these fundamental forces and the associated techniques critical to the laser cooling and trapping of atoms.

2.1 Spontaneous Force

The spontaneous force emerges due to the interaction between an atom and the photons of a laser beam. When an atom absorbs a photon, it transitions from the ground state to an excited state and later emits a photon to return to the ground state. The absorption process is directional, aligning with the incoming laser, while the emission is isotropic. The accumulation of such events results in a net force in the direction of the laser, termed the spontaneous force.

The scattering rate Γ_s for this absorption-emission process is expressed as:

$$\Gamma_s = \frac{\Gamma}{2} \frac{I/I_{sat}}{1 + I/I_{sat} + (2\delta/\Gamma)^2}, \tag{2.1}$$

where Γ is the decay rate of the excited state, I the intensity of the incoming light, I_{sat} the saturation intensity, and δ the detuning of the laser frequency from the atomic transition.

The spontaneous force, $\vec{F}_s$, that acts on the atom is then given by the momentum exchange associated with the emission and absorption of photons.

$$\vec{F}_s = \hbar k \Gamma_s, \tag{2.2}$$

with $\hbar k$ representing the photon momentum.

For a laser intensity much greater than the saturation intensity ($I \gg I_{sat}$), the spontaneous force reaches its maximum:

$$F_{s,max} = \frac{\hbar k \Gamma}{2}. \tag{2.3}$$

This force is pivotal in the domain of laser cooling, a technique instrumental in reducing the kinetic energy of atoms.

2.2 Doppler Cooling

2.2.1 Doppler Shift

In laser cooling applications, the directionality of a laser beam in relation to an atom's motion is crucial due to the Doppler effect. If the propagation of the laser beam is parallel to the atom's velocity vector, denoted by $\vec{k}$ and $\vec{v}$, the atom experiences a decrease in the perceived light frequency, leading to a Doppler shift quantified by $-kv$. In contrast, if the laser beam and the atom's velocity are antiparallel, the resulting Doppler shift is quantified by $+kv$.

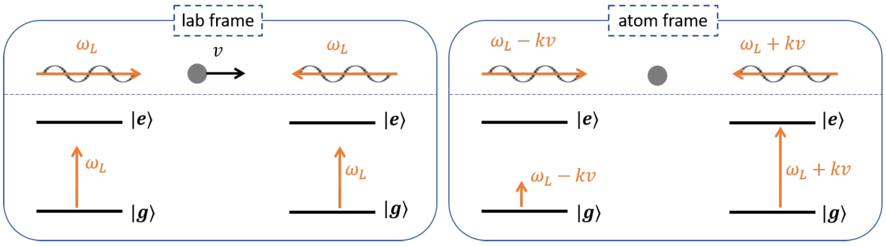

Figure 2.1: A two-level atom subject to red-detuned counter-propagating laser beams in the lab frame and in the atom rest frame. (From [41]).

The laser cooling technique employs a configuration (see Fig. 2.1) in which the atom is simultaneously exposed to two laser beams from opposite directions. The frequency of these lasers is set slightly below the atomic resonance frequency, $\omega_L < \omega_A$, optimizing the Doppler effect to favor the absorption of photons from the beam moving counter to the atom's trajectory. This selective absorption induces a net force in the opposite direction of the atom's motion, effectively slowing it down due to the conservation of momentum.

The Doppler shift thus introduces an additional term to the effective detuning of the laser frequency as it interacts with the moving atoms, described by the equation:

$$\delta' = \delta - \vec{k} \cdot \vec{v}, \tag{2.4}$$

where δ' denotes the adjusted detuning, δ is the initial detuning, and $\vec{k}$ represents the wave vector of the laser.

2.2.2 Optical Molasses

In the case of two laser beams with k-vectors k, the spontaneous force of both beams add up to:

$$F = F_+ + F_- = \hbar k \frac{\Gamma}{2} \left(\frac{I/I_{sat}}{1 + I/I_{sat} + \left(\frac{2(\delta+kv)}{\Gamma}\right)^2} - \frac{I/I_{sat}}{1 + I/I_{sat} + \left(\frac{2(\delta-kv)}{\Gamma}\right)^2} \right). \tag{2.5}$$

For an atom, the total force is then $\vec{F}_{\text{molasses}} = \vec{F}_+ + \vec{F}_-$. For small velocities $\vec{k} \cdot \vec{v} \ll \Gamma$, this term can be expanded to

$$\vec{F}_{\text{molasses}} = \frac{8\hbar k^2 \delta I/I_{sat}}{\Gamma(1 + I/I_{sat} + (2\delta/\Gamma)^2)^2} \vec{v} \approx -\beta \vec{v}. \tag{2.6}$$

Because this combined force damps motion in a way similar to that of a viscous fluid, it is called optical molasses.

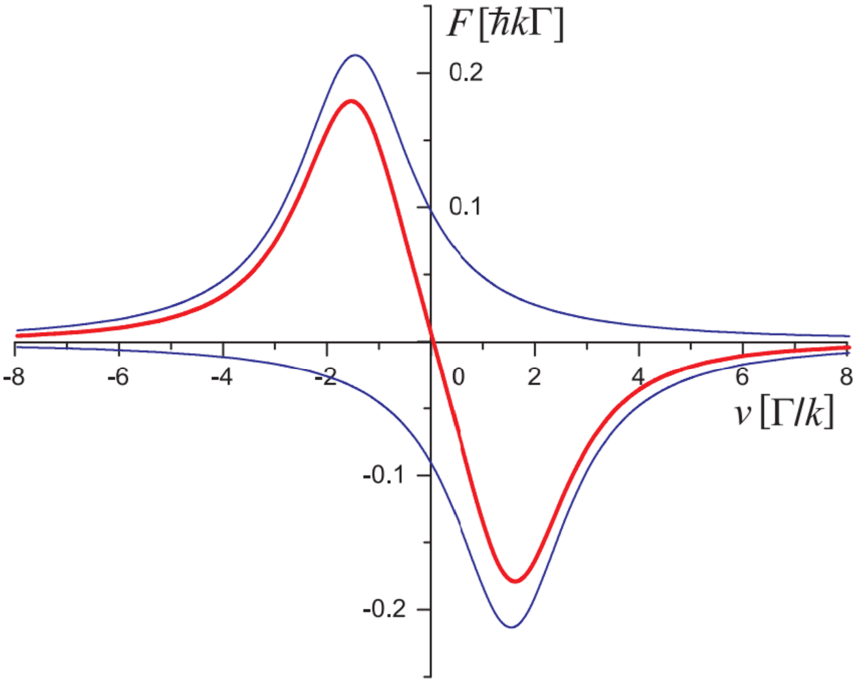

Figure 2.2: The addition of the spontaneous force from two counterpropagating laser beams results in a force $F = -\frac{v}{\lambda}$ forming an optical molasses. (From [42]).

2.3 Zeeman Shift

The Zeeman effect plays a crucial role in manipulating the behavior of fast-moving atoms, particularly in two key applications: compensating for the Doppler shift within a Zeeman slower and confining atoms in a magneto-optical trap. This phenomenon is a direct consequence of the presence of a magnetic field, which induces a shift in the energy levels of an atom, known as the Zeeman shift.

Valence electrons in atoms without nuclear spin exhibit a magnetic moment that is a function of orbital angular momentum (L) and spin (S). This magnetic moment is described by :

$$\mu = -\frac{g_L \mu_B}{\hbar} L - \frac{g_s \mu_B}{\hbar} S, \tag{2.7}$$

where μ_B is the Bohr magneton, $g_L \approx 1$ is the electron orbital g factor and $g_S \approx 2$ is the electron spin g factor. When the energy of the Zeeman shift is less than that of the spin-orbit coupling, the first-order energy perturbation due to the Zeeman effect can be represented by:

$$E_{\text{Zeeman}} = g_J m_J \mu_B B, \tag{2.8}$$

here, $\hat{J}$ denotes the total angular momentum operator, and g_J is the Landé g-factor, determined by the following relationship:

$$g_J = \frac{3J(J+1) - L(L+1) + S(S+1)}{2J(J+1)}. \tag{2.9}$$

The magnetic field in this scenario has magnitude B and is assumed to be aligned along the $\hat{z}$-axis.

For atoms with non-zero nuclear spin I, and in low external magentic field, the Zeeman shift is similarly given by:

$$E_{\text{Zeeman}} = g_F m_F \mu_B B, \tag{2.10}$$

with the Landé g factor for the total angular momentum F defined as:

$$g_F = g_J \frac{F(F+1) - I(I+1) + J(J+1)}{2F(F+1)} + g_I \frac{F(F+1) + I(I+1) - J(J+1)}{2F(F+1)}. \tag{2.11}$$

Since $\frac{g_I}{g_J} = \frac{m_e}{m_p} \ll 1$, the second term can be ignored. This Zeeman shift is referred to as the Zeeman effect of hyperfine splitting.

In a strong external-field regime, the magnetic interaction exceeds the hyperfine structure splitting. Consequently, the quantum number F cannot be used as a good quantum number. The strong magnetic field disrupts the coupling between the orbital and the spin angular momentum. Instead, J becomes a good quantum number.

2.4 Zeeman Slower

The Zeeman slower is a pivotal device in ultracold atoms experiments, designed to decelerate high-velocity atoms to speeds suitable for trapping in a magneto-optical trap (MOT). This deceleration is crucial; in our system, atoms are emitted from an oven at a mean velocity of 1500 m/s, a speed that exceeds by far the capture velocity threshold of most MOTs, which is around 50 m/s.

By applying a spatially varying magnetic field, the Zeeman slower exploits the Zeeman effect to precisely counterbalance the Doppler shift. This shift occurs as the atoms decelerate, altering their resonance frequency with respect to a counterpropagating laser beam. The magnetic field is carefully adjusted along the atom's path to maintain resonance, ensuring effective deceleration. This process effectively brings a significant fraction of the atomic beam within the MOT's capture velocity, thereby enhancing the overall efficiency of atom trapping.

2.4.1 The Magnetic Field Profile in a Zeeman Slower

In a two-level atom, the mean radiation pressure force resulting from the absorption-emission cycles reads:

$$F = \frac{\hbar k \Gamma}{2} \cdot \frac{\frac{I}{I_{sat}}}{1 + \frac{I}{I_{sat}} + \frac{4\delta^2}{\Gamma^2}}, \tag{2.12}$$

where the detuning δ takes into accounts the Doppler and Zeeman shifts:

$$\delta = \omega_L - \omega_A = \delta_0 + kv(z) - \mu' B(z)/\hbar, \tag{2.13}$$

where δ_0 is the shift-free laser detuning from the transition.

We can see from Eq. (2.12) that the deceleration is most efficient when atoms are in resonance with the laser beam:

$$\delta = \delta_0 + kv(z) - \mu^{'} B(z)/\hbar = 0. \tag{2.14}$$

In addition, when $\frac{I}{I_{sat}} \gg 1$ deceleration becomes independent of the laser parameters and reaches its maximum:

$$a_{\max} = \frac{\hbar k \Gamma}{2m}. \tag{2.15}$$

We assume a constant deceleration in the Zeeman slower which is equal to:

$$a = -\eta a_{\max}, \tag{2.16}$$

where $\eta < 1$ quantifies the fraction of the scattering rate-limited maximum deceleration $-a_{\max}$ required for the atoms to remain at resonance and continue the slowing trajectory.

To meet the condition in Eq. (2.14) the magnetic field along Zeeman slower should be:

$$B(z) = [\delta_0 + kv(z)]\frac{\hbar}{\mu'}, \tag{2.17}$$

where:

$$\mu' = \left((m_F g_F)_e - (m_F g_F)_g\right)\mu_B \simeq -\mu_B. \tag{2.18}$$

The subscripts g and e indicate the ground and excited state, and g_F is defined in Eq. (2.11).

Following Eq. (2.16), we can write the well-known kinematic equation for velocity in constant deceleration as:

$$v(z) = \sqrt{2az + v_c^2}, \tag{2.19}$$

where $v_c = v(z = 0)$ is the capture velocity (the largest velocity class addressed by the slowing process). Substituting this in Eq. (2.17) gives:

$$B(z) = \frac{\hbar}{\mu'}[\delta_0 + k\sqrt{2az + v_c^2}], \tag{2.20}$$

we can rewrite Eq. (2.20) as:

$$B(z) = \frac{\hbar\delta_0}{\mu'} + \frac{\hbar k v_c}{\mu'}\sqrt{1 - \frac{z}{L_{\text{stop}}}}, \tag{2.21}$$

where $L_{\text{stop}} = -\frac{v_c^2}{2a}$. L_{stop} is the distance required to bring the atoms to rest with constant deceleration $-\eta a_{\max}$.

However, it is necessary for the atoms to be extracted from the slower at a non-zero final velocity v_f. The slowing length required to reach v_f is $L = L_{\text{stop}} - \frac{v_f^2}{2\eta a_{\max}} < L_{\text{stop}}$.

Finally, we can write the magnetic field as:

$$B(z) = \begin{cases} B_0 + B_L\sqrt{1 - \frac{z}{L_{\text{stop}}}}, & \text{if } 0 < z < L, \\ 0, & \text{otherwise.} \end{cases} \tag{2.22}$$

The degrees of freedom of the design are the offset of the field $B_0 = \frac{\hbar\delta_0}{\mu'}$ and the amplitude $B_L = \frac{\hbar k v_c}{\mu'}$. The field profile is truncated to $z = L < L_{\text{stop}}$ to extract the slow atoms. The field therefore varies from $B_0 + B_L$ at $z = 0$ to $B_0 + \frac{\hbar k v_f}{\mu'}$ at $z = L$.

2.4.2 Zeeman Slower Types

By selecting the detuning of the slowing laser, three distinct types of Zeeman slowers can be implemented, each having its distinct benefits and disadvantages. Magnetic fields of these different types are shown in Fig. 2.3.

1. **Decreasing Field Zeeman Slower:** In a decreasing field Zeeman slower, the initial magnetic field strength is maximized to offset the Doppler shift of the fastest atoms, ensuring that the slowing laser, operating at a slight red detuning, resonates with atoms reaching their final velocity under zero-field conditions. This configuration, characterized by a gradual reduction in magnetic field strength toward the trap center, allows for efficient deceleration of atoms with a minimal magnetic field near the magneto-optical trap (MOT), thereby reducing the need for compensation of stray magnetic fields and minimizing heat production near the experimental chamber. The disadvantage of this approach is the small detuning necessary to achieve low final velocities; as the slower laser beam must traverse the MOT region, it can perturb the trapped atoms due to additional light pressure, leading to potential overheating and reduced availability of light for further deceleration. This issue can be mitigated by adjusting the detuning of the slowing laser and applying offset fields, yet the undefined end of the slowing length poses a risk of over-slowing and pushing atoms in the opposite direction.

2. **Increased Magnetic Field Zeeman Slower:** In an increasing field Zeeman slower, the magnetic field starts at zero and intensifies towards the end, peaking at the exit near the MOT chamber to counteract the Doppler shift of the fastest atoms. This setup necessitates the slowing laser to be significantly red-detuned, ensuring that atoms quickly fall out of resonance once they exit the slower. The configuration facilitates the extraction of slow atoms due to a well-defined field maximum, allowing for a swift transition out of resonance. However, a significant disadvantage is the generation of strong residual magnetic fields at the MOT (Magneto-Optical Trap) location, necessitating the use of powerful compensation coils to mitigate potential disturbances. Despite the substantial distance between the end of the Zeeman slower and the center of the MOT in some setups, which minimizes the impact of leaking fields, the need for careful compensation remains crucial to prevent disruption to the trapped atoms. Moreover, increasing the distance between the MOT and the Zeeman slower can cause the atomic beam to diverge, thereby reducing the flux into the MOT.

3. **Spin Flip Zeeman Slower:** This type merges the benefits of both increasing and decreasing field configurations by initially deploying a decreasing magnetic field that transitions through zero (zero-crossing) and then reverses direction, culminating in a maximum value. This design is characterized by a red-detuned slowing beam and necessitates lower initial magnetic fields. The crucial advantage of the spin-flip approach is its ability to minimize high magnetic-field gradients near the MOT, facilitating a controlled conclusion of the slowing process while allowing for adjustments in the final velocity of the atoms. The precise placement of the zero-crossing point, critical for maintaining resonance conditions without unintended deviations, is determined by the available laser detuning. Despite these benefits, the spin-flip slower introduces challenges, particularly in maintaining effective cooling transitions in regions of low magnetic field strength. Specifically, in such regions, atoms are prone to transitions into dark states, necessitating the use of a repumper laser to maintain them in the bright state. However, the effective magnetic moment for the repumping transition differs from that of the slowing transition, complicating the task of keeping the repumper beam in resonance across the entire magnetic field range.

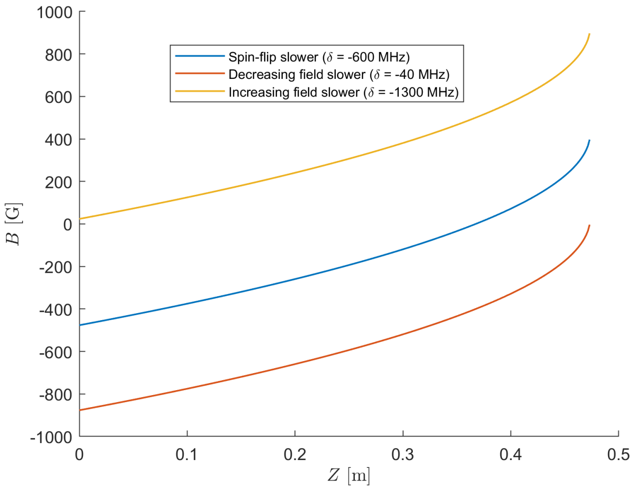

Figure 2.3: Zeeman slower types (for negative detuning).

2.5 Magneto-Optical Trap

The optical molasses technique, as detailed in Section 2.2.2, is highly effective in cooling the atoms. However, the force acting on the atoms exhibits only a velocity-dependent component. To confine the atoms spatially, a force dependent on the spatial coordinates becomes necessary. Interestingly, this requirement can be met by employing a straightforward magnetic field configuration along with the same laser setup as in optical molasses. This realization is commonly referred to as a magneto-optical trap (MOT). The following section describes the principles and characteristics of MOT.

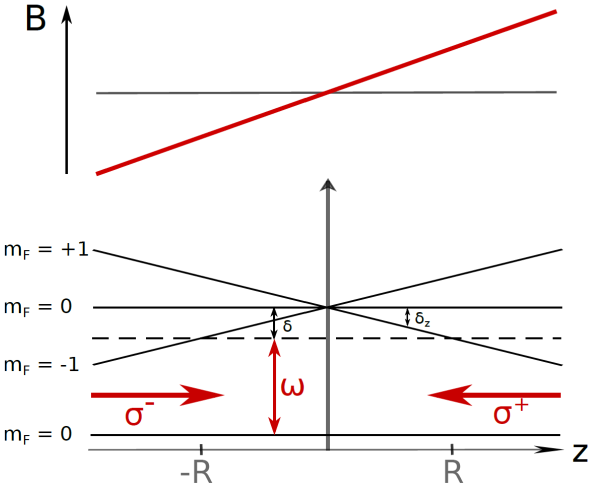

Figure 2.4: A simple 1-dimensional model of a magneto-optical trap with a single ground state and triplet split excited states. Atoms at positive (negative) positions relative to the zero of the magnetic field are tuned into resonance with the red-detuned laser. The σ^+ polarised laser only acts on the $\Delta m = +1$ and the $-\sigma^-$ polarised laser on the $\Delta m = -1$ state according to the selection rules. (From [43]).

In the MOT setup, a quadrupole magnetic field created by anti-Helmholtz coil configuration produces a linear gradient $B_z = B' \cdot z$, where $B' = \frac{dB}{dz}$, ensuring that the magnetic field at the trap's center ($z = 0$) is zero.

To understand the mechanism by which a magnetic field induces a position-dependent force in the MOT, refer to the energy diagram depicted in Fig. 2.4. This figure illustrates a one-dimensional MOT employing two counter-propagating laser beams with opposite circular polarizations (σ^+ and σ^-) and red-detuned ($\delta < 0$) from resonance. For simplicity, consider the atom's energy levels as being reduced to an $F = 0$ ground state and an $F = 1$ triplet excited state. At the trap's center, where $\delta = 0$, atoms resonate equally with both beams. As an atom drifts towards the positive z-axis, the magnetic field causes the energy of the $m_F = -1$ excited state to shift further from laser resonance, whereas the $m_F = +1$ state shifts closer. Given that the σ^- beam cannot excite the $m_F = +1$ state, atoms predominantly absorb photons from the σ^+ beam. This asymmetry in photon absorption exerts a scattering force that pushes the atom back towards the magnetic field's center. In contrast, for atoms moving towards $z < 0$, the σ^- beam becomes more effective, directing the force towards the center of the trap.

The Doppler shift of the red-detuned optical molasses and the Zeeman shift result in a total detuning:

$$\delta_{\pm}^{MOT} = \delta_0 \mp k \cdot v \pm \frac{\mu' B' z}{\hbar}. \tag{2.23}$$

The effective magnetic moment of the transition μ' is defined in Eq. (2.18).

When incorporating the spatial dependence due to the Zeeman effect, Eq. (2.5) undergoes a modification to

$$\vec{F}(\vec{v}, \vec{z}) = \frac{\hbar k \Gamma}{2} \left(\frac{I/I_{sat}}{1 + I/I_{sat} + \left(\frac{2\delta_+}{\Gamma}\right)^2} - \frac{I/I_{sat}}{1 + I/I_{sat} + \left(\frac{2\delta_-}{\Gamma}\right)^2} \right). \tag{2.24}$$

When both the Doppler and Zeeman shifts are small compared to the laser detuning δ_0, the dominator of the force can be expanded and the force becomes:

$$\vec{F} = -\kappa \vec{z} - \beta \vec{v}, \tag{2.25}$$

with the spring constant κ of an harmonic oscillator

$$\kappa = \frac{\mu'}{\hbar k} B' \beta. \tag{2.26}$$

Extending the MOT into three dimensions is achieved by adding similar beams and magnetic fields from the $\hat{x}$ and $\hat{y}$ directions. The magnetic field can be generated by a set of anti-Helmholtz coils, which produce magnetic fields $\vec{B}(x, y, z) = B_0(\hat{x}x + \hat{y}y - 2\hat{z}z)$ near the zero in the center of the structure (see Fig. 2.5)

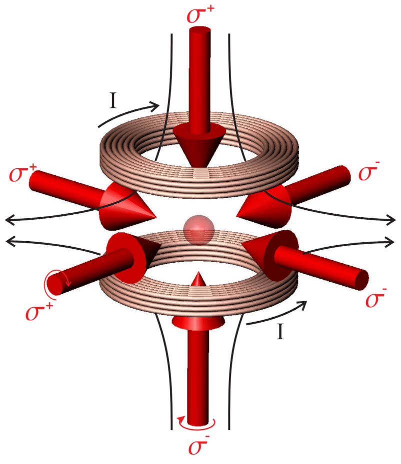

Figure 2.5: Principle of the magneto-optical trap: A pair of anti-Helmholtz coils generates a spherical quadrupole magnetic field. Three pairs of red-detuned counterpropagating beams of circularly polarized laser light provides the trapping force. (From [44]).

Chapter 3

Overview of Lithium Experimental Setup and Key Considerations

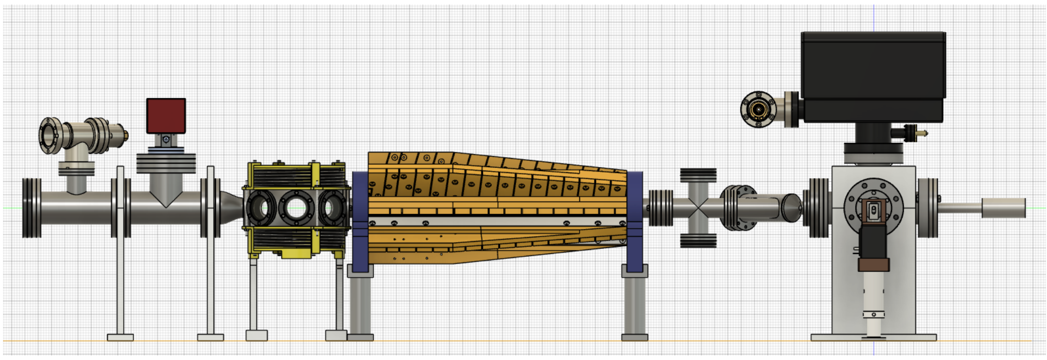

(a) Lithium experimental design - side view.

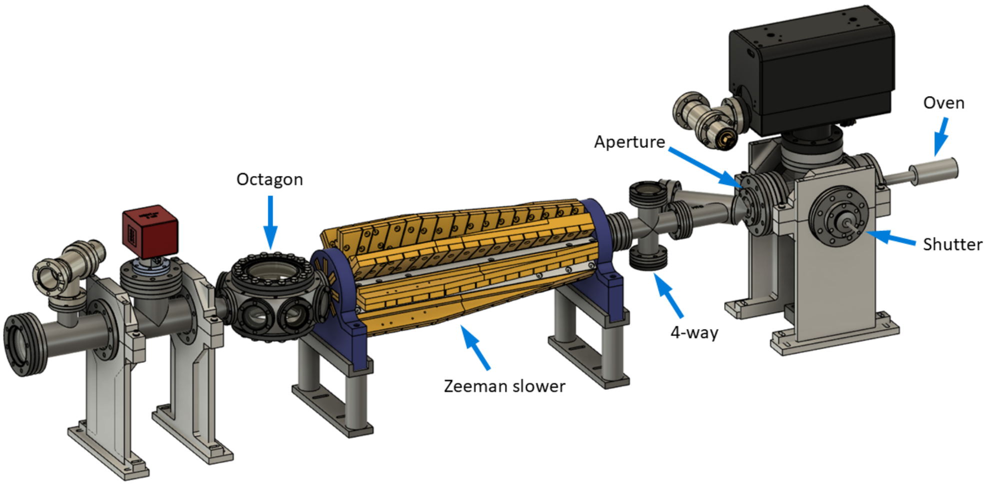

(b) Lithium experimental design - isometric view.

Figure 3.1: Lithium experimental design from different views.

3.1 Experimental Setup Overview

Figure 3.1 displays our Lithium experimental setup, which comprises several key components to manage and control lithium atoms throughout the experiment. The setup begins with an oven that heats lithium to create a beam of lithium atoms. These atoms are injected into a four-way chamber, where a shutter mechanism controls the flow of the atoms, allowing precise timing for their entry into the subsequent sections.

Following the four-way chamber, the atoms pass through an aperture that limits their angular distribution. This serves as a collimation setup for the atomic beam, effectively aligning the atoms to move primarily in the axial (z) direction and minimizing their velocities in the x and y directions.

This collimated beam of atoms then enters the Zeeman slower, which uses a magnetic field produced by permanent magnets to gradually reduce the velocity of the lithium atoms. After the Zeeman slower, the atoms enter the octagonal chamber, which houses the Magneto-Optical Trap (MOT).

The entire setup is maintained under high vacuum conditions, which is essential for high-precision atomic experiments. An ion pump, along with a rotary pump initially used for rough pumping, ensures the required vacuum level by removing unwanted particles and contaminants from the system.

The detailed design and operation of the Zeeman slower and MOT will be covered in the subsequent chapters of this thesis.

3.2 ^{7}Li Level Structure & Properties

Lithium (Li) is the third element in the periodic system with its three electrons (or the nuclear charge of $Z = 3$). Lithium is the lightest alkali-metal atom, with a standard atomic weight of 6.94 amu. Lithium has two stable isotopes: ^{7}Li, a boson with nuclear spin of $I = \frac{3}{2}$, and ^{6}Li, a fermion with nuclear spin of $I = 1$. Both isotopes exhibit a hyperfine structure and have been cooled to quantum degeneracy. ^{7}Li has a natural abundance of approximately 92.5% while ^{6}Li has 7.5%. We are constructing a new apparatus capable of trapping and cooling ^{7}Li.

As an alkali metal, ^{7}Li has a single valence electron, which exists in a $2s$ shell when unexcited, so $S = \frac{1}{2}$, $L = 0$, and $J = \frac{1}{2}$, giving a Russell-Saunders term $^2S_{1/2}$. The ground state of ^{7}Li splits into two hyperfine levels, denoted as $F = 2$ and $F = 1$, with a frequency difference of 803.5 MHz between them. Optical transitions of interest typically occur between the hyperfine manifolds of the $2s$ and $2p$ levels. These transitions are closely spaced, within about 10 GHz, at a wavelength near 671 nm, and exhibit linewidths of 5.9 MHz.

The energy level (2p) splits into two fine-structure states, separated by 10.052 GHz.

This separation has historically been observed as a double peak in atomic fluorescence spectra. Transitions from the $^2S_{1/2}$ state to the $^2P_{1/2}$ state are designated as D1 transitions, while transitions to the $^2P_{3/2}$ state are referred to as D2 transitions. The $^2P_{1/2}$ state is further divided into hyperfine levels $F' = 2$ and $F' = 1$, and the $^2P_{3/2}$ state into four hyperfine levels, marked $F = 0, 1, 2,$ and 3. The hyperfine splitting in the $^2P_{1/2}$ level amounts to 92.03 MHz, while the splittings in the $^2P_{3/2}$ level are significantly smaller.

Hyperfine levels $F' = 2$ and $F' = 3$ are the most experimentally relevant states that exhibit a separation of 9.39 MHz. This gap is of the same magnitude as the linewidths associated with these transitions, making it indistinct in measurements. For a visual representation of these energy levels in ^{7}Li, refer to Fig. 3.2, which encapsulates these specifics.

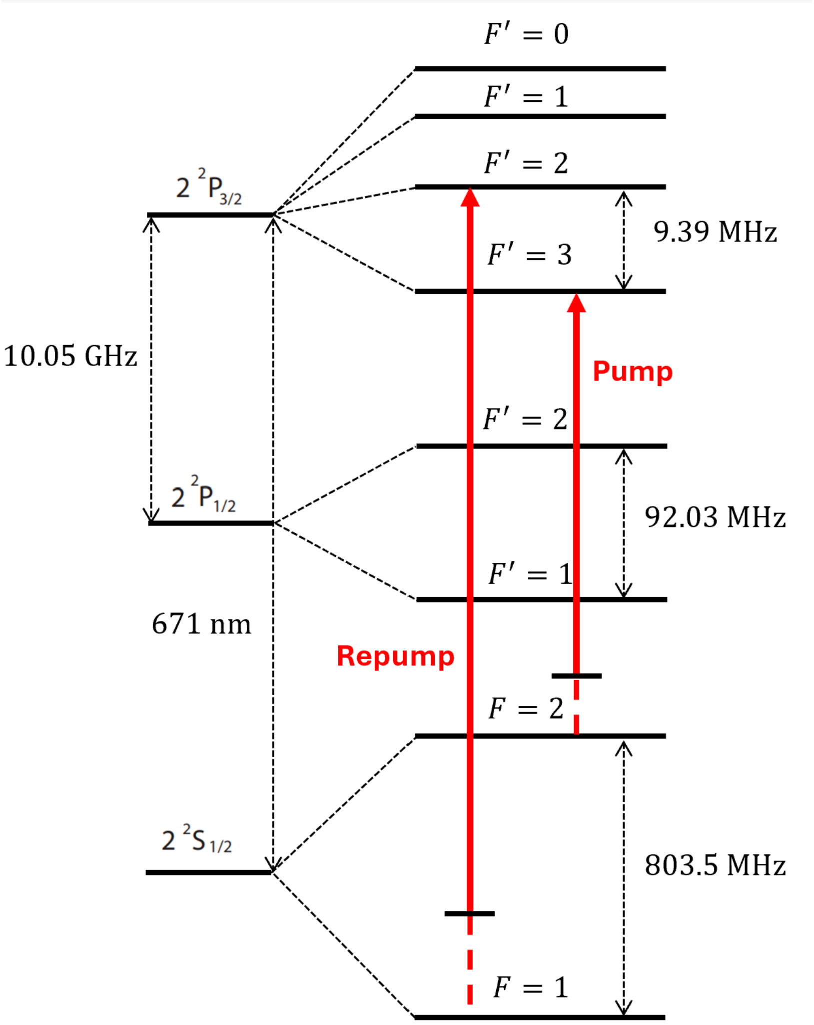

Figure 3.2: A level diagram depicting experimentally relevant energy levels in ^{7}Li.

The only pumping transitions available are the $\sigma_\pm$ D2 transitions between $^2S_{1/2}\,|F = 2, m_F = \pm 2\rangle$ and $^2P_{3/2}\,|F' = 3, m_{F'} = \pm 3\rangle$ hyperfine sub-levels. However, in practice, since the splitting between the $F' = 3$ and $F' = 2$ manifolds in the $^2P_{3/2}$ state is only

9.39 MHz, imperfect polarization leads to the population of the $F' = 2$ sub-levels, which introduces a leak into the ground-state $F = 1$ manifold. In order to scatter sufficient photons off of ^{7}Li atoms to slow, cool, or image them, a "repump" laser is required. Resonant with the D2 transition from $^2S_{1/2}\, F = 1 \rightarrow {}^2P_{3/2}\, F' = 2$, and 812.9 MHz detuned from the pump.

3.3 Li Oven: Velocity Distribution

The oven is meticulously engineered to hold about 5 grams of lithium, which is placed inside at an initial temperature of $25°C$. Then it is heated to $400°C$ to enable the evaporation process. The oven's dimensions are precisely calculated; its length is designed to contain the entire amount of lithium in one single rod form, with a diameter of 1.27 cm, and the length of the oven at room temperature measures 7.39 cm (approximately 2.91 inches). This ensures that the lithium, once introduced, is fully accommodated within the oven. When lithium is heated and melts, its volume expands from 9.363 mL at $25°C$ to 10.204 mL at $400°C$. The design incorporates an oven depth that is calculated to be sufficiently deep to prevent any spillage of the molten lithium over the edges, ensuring safety and efficiency throughout the evaporation process. The design considerations are depicted in the accompanying Fig. 3.3.

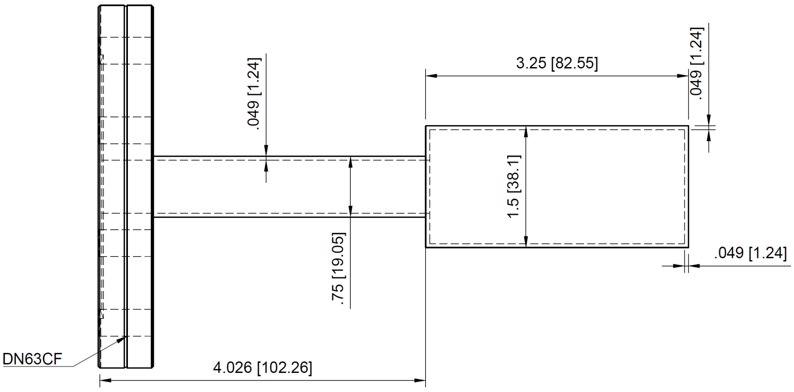

Figure 3.3: Cross-sectional view of the lithium evaporation oven design, with dimensions provided in inches [mm].

The ^7Li atoms are extracted from the oven in the form of an atomic beam with the modified Maxwell-Boltzmann velocity distribution [45]:

$$f(v) = 2\left(\frac{m}{2k_BT}\right)^2 v^3 e^{-\frac{mv^2}{2k_BT}}, \tag{3.1}$$

where $f(v,T)dv$ gives the probability for an atom to have a velocity between v and $v+dv$ at a temperature T, m is the mass of the atom and k_B is Boltzmann's constant.

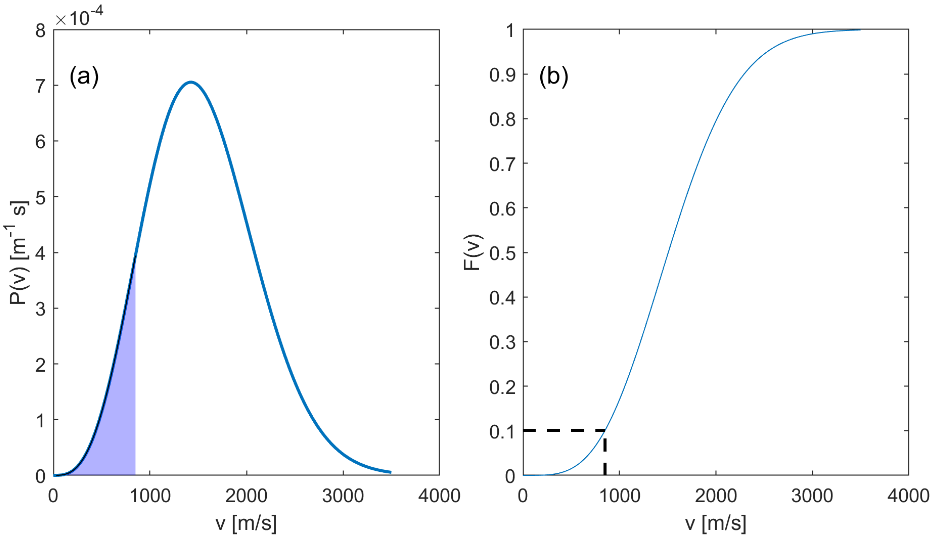

Figure 3.4: (a) Velocity distribution for an escaping effusive atomic jet from the oven at temperature $T = 300\,°\mathrm{C}$. The blue zone marks the velocity classes slowed down by our Zeeman slower, assuming a capture velocity of $v_c = 850\,\mathrm{m\,s^{-1}}$ and an exit velocity of $v_f = 30\,\mathrm{m\,s^{-1}}$. (b) The distribution function of velocities. The proportion of atoms slowed in the Zeeman slower amounts to approximately 10 %

.

By integrating Eq. (3.1) on the velocities, we obtain the distribution function $F(v)$ which corresponds to the fraction of atoms whose velocity is less than or equal to v:

$$F(v) = 1 - \left(1 + \frac{mv^2}{2k_BT}\right)\exp\left(-\frac{mv^2}{2k_BT}\right). \tag{3.2}$$

The functions $P(v)$ and $F(v)$ are shown, respectively, in Figs. 3.4 (a) and (b) for an effusive jet leaving the oven at a temperature $T = 300\,°\mathrm{C}$. By the definition of the distribution function, the portion of the slowed atoms is given by $F(v_c) - F(v_f)$. For $T = 300\,°\mathrm{C}$, assuming $v_c = 850\,\mathrm{m\,s^{-1}}$ and $v_f = 30\,\mathrm{m\,s^{-1}}$, approximately 10% of the atoms are slowed down to the final velocity v_f.

3.4 Loading Rate

We can determine the MOT loading rate f, by calculating the flux of atoms that are slowed to a velocity less than or equal to the MOT capture velocity, v_c^{MOT}.

To calculate the loading rate I follow the the equations presented in the Friedhelm Serwane Diploma thesis [46]. We begin by estimating the atomic flux of atoms exiting the oven. This flux is limited by the oven's aperture, which has an area A. In our case, $A = (2\,\mathrm{mm})^2\pi$, and the flux can be estimated as follows:

$$f_{\text{oven}} = \frac{n\overline{v}A}{4}, \tag{3.3}$$

where

$$n = \frac{p}{k_B T}, \tag{3.4}$$

and the atomic density n at vapor pressure p is derived using the ideal gas law. The mean atomic velocity, represented by $\overline{v}$, is determined by the equation $\overline{v} = \sqrt{\frac{2k_BT}{m}}$. For a temperature of $T = 400\,°\mathrm{C}$, this results in a mean velocity for $\overline{v} = 1263\,\mathrm{m/s}$, resulting in the following atomic flux:

$$f_{\text{oven}} = 1.17 \times 10^{16}\,\frac{\text{atom}}{\text{sec}}. \tag{3.5}$$

The number of atoms exiting the oven per second with both longitudinal and transversal velocities, and in directions specified by angles θ (polar) and ϕ (azimuthal), is given by:

$$\dot{N}_{v,\theta,\phi} = \frac{nA}{\pi^{3/2}\overline{v}^3} v \exp\left(\frac{-v^2}{\overline{v}^2}\right) \cos\theta v^2 \sin\theta\, dv\, d\theta\, d\phi. \tag{3.6}$$

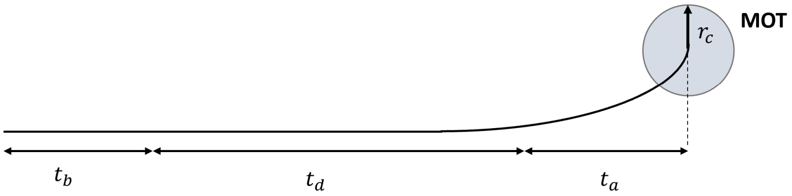

Figure 3.5: Trajectory of the atoms.

Because only the atom's axial velocity v_z decreases as it moves through the slower, the atom does not follow a straight trajectory through the slower. Rather, the trajectory curves increasingly outward during deceleration, as shown in Fig. 3.5. This leads to a divergence of the atomic beam after a certain time of flight. When the divergence is larger than the capture radius of the MOT r_c, the flux of trappable atoms is reduced: Only atoms with a small transverse velocity can be trapped in the MOT. The maximum transverse velocity v_r depends strongly on the atom's time of flight:

$$v_r \leq v_{r,max} = \frac{r_c}{t_b + t_d + t_a}, \tag{3.7}$$

where $r_c \approx 1cm$, and the atom's time of light: (b)efore, (d)uring, and (a)fter deceleration which depends on the radial velocity. Specifically, the time of flight from the end of the slower to the MOT is defined as $t_a = \frac{d_a}{v_{end}}$, where d_a is the distance between the Zeeman slower's endpoint and the center of the MOT. The atom's flight duration within the slower, t_d, can be calculated using kinematics:

$$t_d = \frac{1}{a}\left(\sqrt{v_f^2 + 2aL} - v_f\right). \tag{3.8}$$

This formula accounts for the atom's final velocity v_f, the acceleration a, and the length of the slower L, to determine t_d, the time spent during the deceleration.

$$t_d = \frac{1}{a}(\sqrt{v_f^2 + 2aL} - v_f). \tag{3.9}$$

Following the above equations, we can rewrite the maximum radial velocity as:

$$v_{r,\max} = \frac{r_c}{\frac{d_b}{\sqrt{v_f^2+2aL}} + \frac{1}{a}\left(\sqrt{v_f^2 + 2aL} - v_f\right) + \frac{d_a}{v_f}}, \tag{3.10}$$

where a is the deceleration given by:

$$a = \frac{\hbar k \Gamma}{2m} \frac{\frac{I}{I_{sat}}}{1 + \frac{I}{I_{sat}}}. \tag{3.11}$$

The total number of atoms per second trappable by the MOT can be calculated by calculating the integrals of Eq. (3.6) over angles and velocities using the limits for $v_r^{\max}$ and $v_z^{\max}$, where $v_z^{\max}$ is the maximum axial velocity that can be slowed in the Zeeman slower (the Zeeman-slower capture velocity).

$$f = f_{\text{oven}} \cdot \left(1 - e^{-\left(\frac{v_{z,\max}^2}{\overline{v}^2}\right)}\right) \cdot \left(1 - e^{-\left(\frac{v_{r,\max}^2}{\overline{v}^2}\right)}\right). \tag{3.12}$$

Eq. (3.12) is crucial in determining the optimal length of the Zeeman slower, a key component in achieving a high atom loading rate in MOT. This equation allows us to understand the relationship between the Zeeman slower's length and the MOT's loading rate. After establishing the Zeeman slower's length, the equation helps identify the optimal distance between the MOT and the Zeeman slower, including how much deviation from this distance can be tolerated without significant atom loss. In addition, it provides information on the impact of varying capture velocities on the loading rate. Furthermore, the equations presented in this section will be utilized subsequently to assess the performance of our Zeeman slower.

Chapter 4

Permanent Magnets Zeeman Slower (PMZS): Design & Simulation

4.1 Magnetic Field of Cuboid Permanent Magnets

Permanent magnets, particularly rare-earth magnets such as neodymium (NdFeB), have become increasingly affordable and compact. Due to their superior magnetic properties, they are widely used across various industries.

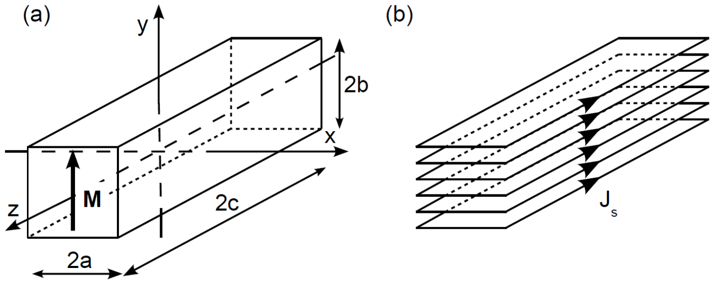

Figure 4.1: Left: conventions and notations for a block magnet. Right: equivalent rectangular solenoid. (From [7]).

Given cuboid magnets with dimensions $2a \times 2b \times 2c$ and magnetization oriented along the y-axis, as shown in Fig. 4.1(a), the magnetic field produced by these magnets can be calculated. By applying Biot-Savart's law to a single coil and integrating along the y-axis, we determine the magnetic field characteristic of a rectangular solenoid. The expression for this field is provided by [7]:

$$B_{\text{sol}}(x, y, z) = \mu_0 J_s \sum_{n,p,q=0}^{1} (-1)^{n+p+q} \mathbf{B}(x - (-1)^p a, y - (-1)^n b, z - (-1)^q c), \tag{4.1}$$

where **B** is a vector field whose coordinates are:

$$\begin{aligned} B_x(X,Y,Z) &= \frac{1}{2}\log\left(\frac{\sqrt{X^2+Y^2+Z^2}-Z}{\sqrt{X^2+Y^2+Z^2}+Z}\right), \\ B_y(X,Y,Z) &= -\arctan\left(\frac{Y\sqrt{X^2+Y^2+Z^2}}{XZ}\right), \\ B_z(X,Y,Z) &= B_x(Z,Y,X). \end{aligned} \tag{4.2}$$

In Eq. (4.1), J_s is the surface current density whose magnitude in our considered cuboid case (see Fig. 4.1 (b)) is given by $\mu J_s = \mu_0 M$ where μ_0 represents the magnetic permeability of the vacuum.

Eqs. (4.1, 4.2) show that the field produced by a permanent magnet is not uniform and exhibits components along the three spatial directions. Consequently, it is essential to devise a configuration of multiple strategically placed magnets to achieve the uniform field required to construct an ideal field profile for lithium. This topic will be explored in the following section.

4.1.1 Halbach Configuration

Drawing on the principles outlined by K. Halbach [47] and further explored by P. Cheiney [7], we consider a Halbach array to create a uniform magnetic field in a transverse cross section. This configuration involves a hollow magnetic cylinder with an internal radius R_{int} and an external radius R_{ext}, where the magnetization **M** at a given point, defined by the angle θ from the y-axis, is oriented at an angle 2θ with respect to the same axis, as shown in Fig. 4.2(a). Such an arrangement is essential for applications like the Zeeman slower, where a highly uniform field is critical. The Halbach cylinder, leveraging the rotational symmetry of magnetization, ensures that the magnetic field within the cylinder is homogeneous and decreases to zero outside, adhering to the desired field characteristics for optimal operation. The expression for this field is given by:

$$\mathbf{B}_{\text{Hal}}(r) = \begin{cases} \mathbf{0} & \text{for } r > R_{\text{ext}} \\ B_R \ln\left(\frac{R_{\text{ext}}}{R_{\text{int}}}\right)\hat{\mathbf{y}} & \text{for } r < R_{\text{int}}, \end{cases} \tag{4.3}$$

where BR is the remanent field of the magnet, which is given by: $B_R = \mu_0 M$

Adopting the eight-pole Halbach configuration, inspired by [7] and shown in Fig. 4.2(b), we arrange eight magnets at 45-degree intervals. This setup produces a magnetic field with the same properties as the Halbach cylinder, as detailed by Eq. (4.3). It generates a strong and homogeneous field with an intensity that quickly drops outside the magnetic ring. This behavior is verified in the right panel of Fig. 4.3, which

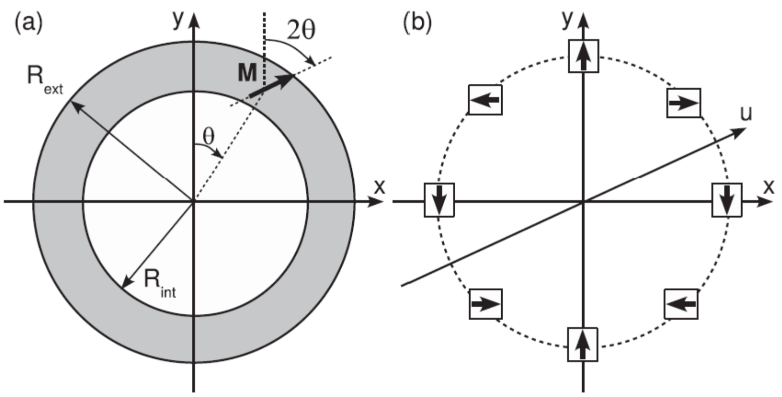

Figure 4.2: (a) Schematic representation of the Halbach configuration making it possible to create a homogeneous magnetic field oriented along the y-axis inside the hollow cylindrical magnet, and nothing outside. (b) The transverse section shows the configuration adopted in our setup to produce the magnetic field, which takes Halbach geometry by reducing the continuous magnetic cylinder to a set of discreet eight permanent magnets. (From [7])

.

displays the magnetic field created by this type of setup in a plane perpendicular to the atomic jet. Furthermore, as shown in Fig. 4.3, the field's strength rapidly falls from several thousand gauss to just a few gauss within a few centimeters. This rapid decrease in field strength is particularly important as it ensures that the magnetic field does not interfere with the operation of a nearby magneto-optical trap (MOT), especially when Halbach rings are positioned close to the MOT.

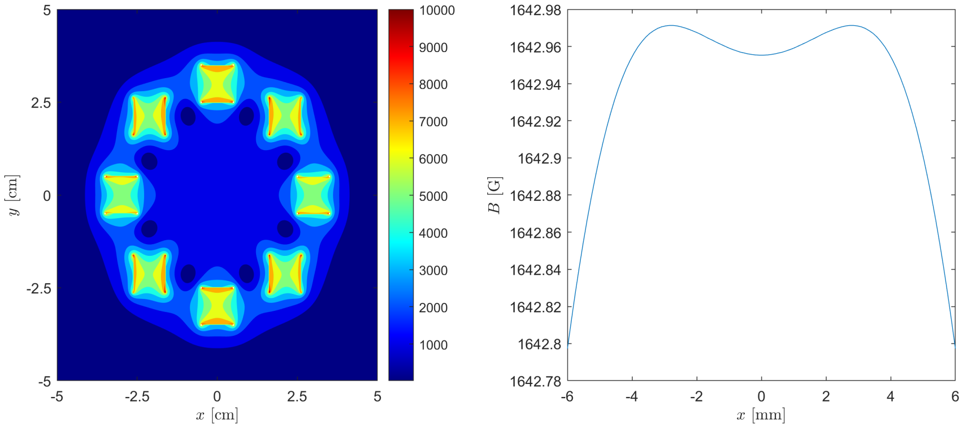

Figure 4.3: Left: representation of the magnetic field's magnitude in the x, y plane. The squares indicate the positions of the magnets, arranged on a circle with a radius of $R = 3$ cm around the axis. The field decreases rapidly outside the system composed of eight magnets, diminishing within a few centimeters. Right: cross-section of the magnetic field along the x-axis in the area close to the atoms, showing excellent homogeneity.

4.2 Spatial Arrangement of Permanent Magnets

In this section, I provide an in-depth explanation of the Zeeman slower design process, including the following:

- Defining the precise spatial arrangement of the magnets.
- Establishing the connection between the magnets' positions based on their respective rotational angles around the x-axis.
- Identifying the essential parameters required to create a magnetic field that closely aligns with the theoretical magnetic field.

In our general setup, we consider a sequence of N consecutive Halbach rings. Figure 4.4 illustrates one such Halbach ring, labeled as 'n,' comprising eight magnetic bars. These magnets are strategically placed along a circular path with a radius denoted as R_n. Within this ring, each magnet center is located at a specific angle θ relative to the y-axis, where $\theta_i = (i-1) \cdot \frac{2\pi}{8}$ for $i = 1$ to 8.

To specify the center of each magnet relative to the laboratory frame, we use the coordinates (x_i, y_i, z_n), where:

$x_i = R_n \cdot \sin(\theta_i)$,

$y_i = R_n \cdot \cos(\theta_i)$,

and z_n is the same for all magnet centers within the same Halbach ring.

Furthermore, we have opted to employ a left-handed Cartesian coordinate system. In this system, the positive z-coordinates are directed inwards into the page. This choice ensures that the z-coordinates of the magnets within the Zeeman slower are regarded as positive.

After analyzing the transverse cross-section in the xy-plane and establishing the positions of each magnet within the Halbach ring, we now turn our attention to the longitudinal cross-section in the zy-plane. In Figure 4.5, we depict two of eight magnets that belong to four consecutive Halbach rings. We have chosen to illustrate only two magnets from each Halbach ring for the sake of clarity.

In the construction of the Halbach ring, we utilize identical permanent magnets characterized by dimensions $[a, b, c]$. These magnets are uniformly rotated by an angle α with respect to the x-axis, as shown in Fig. 4.5. With knowledge of the angles α for all N Halbach rings, as well as the initial radius R_n and its corresponding z-axis position z_n for the first Halbach ring, our objective is to determine the radius R_{n+1} and the position z_{n+1} for the subsequent Halbach ring.

To achieve this, we consider two adjacent magnets within each Halbach ring, specifically magnets n and $n+1$, each positioned at angles α_n and α_{n+1}, respectively, relative to the x-axis. Our calculations cover all possible scenarios, accounting for whether

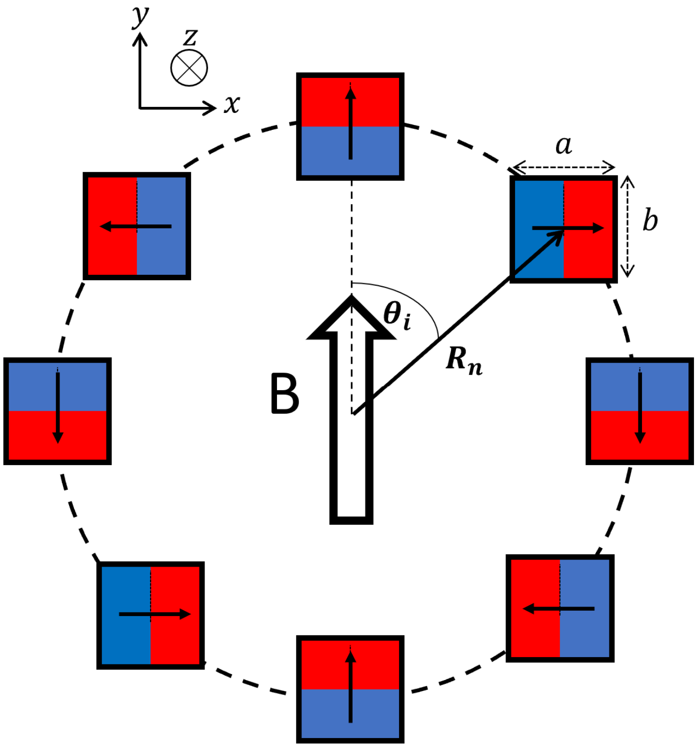

Figure 4.4: Transverse cross section showing a 8-pole Halbach configuration.

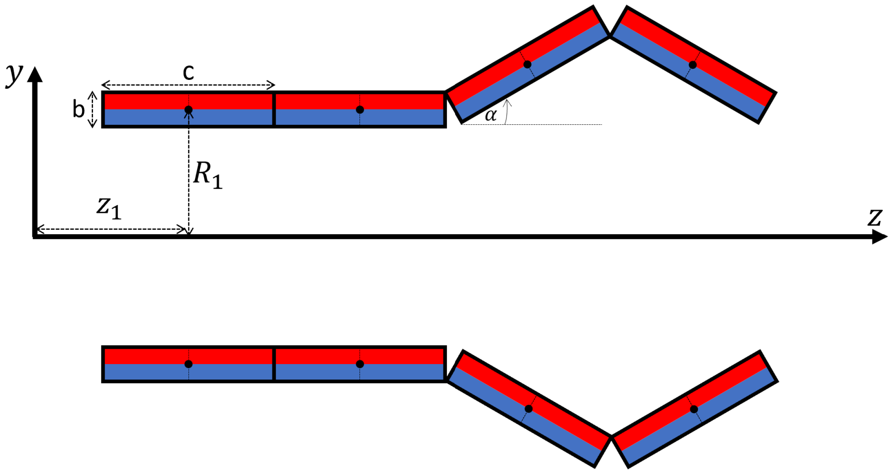

Figure 4.5: Magnets design parameters.

α_n is greater than, smaller than, or equal to α_{n+1}, while also considering the signs of these angles, as detailed in Table 4.1.

Given the initial values of R_n and z_n for magnet n, we determine the values of R_{n+1} and z_{n+1} for the subsequent magnets. We present a comprehensive calculation for one specific case — for clarity and brevity — in which α_{n+1} is greater than α_n, both angles are positive. The methodology is visually illustrated in Figs. 4.6 and 4.7.

We begin by expressing the radial coordinate of the Halbach ring number n, de-

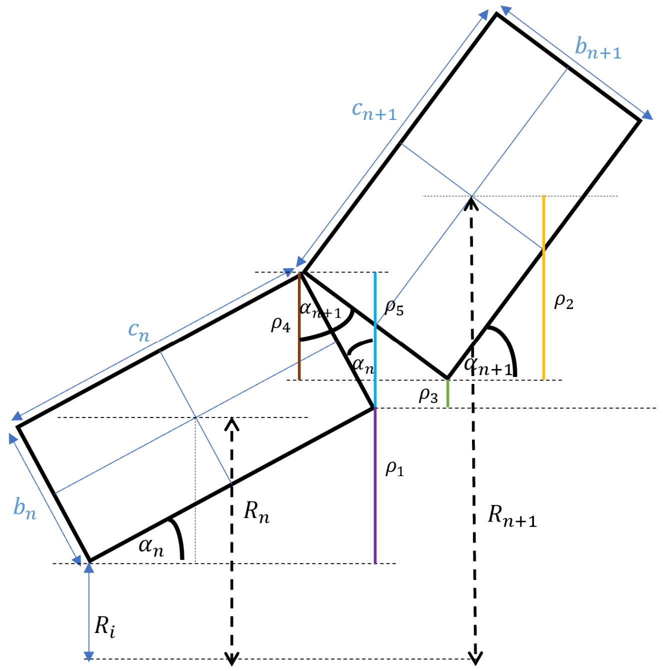

Figure 4.6: Illustration of R_{n+1} calculation given R_n for $\alpha_{n+1} > \alpha_n$ with positive angles.

noted as R_n, relative to the reference point R_i, based on Fig. 4.6, as follows:

$$R_n = R_i + \frac{1}{2}c_n \sin(\alpha_n) + \frac{1}{2}b_n \cos(\alpha_n). \tag{4.4}$$

Additionally, the Halbach radius of the next loop, R_{n+1} is given by:

$$R_{n+1} = R_i + \rho_1 + \rho_2 + \rho_3, \tag{4.5}$$

where:

$$\begin{aligned} \rho_1 &= c_n \sin(\alpha_n), \\ \rho_2 &= \frac{1}{2}c_{n+1} \sin(\alpha_{n+1}) + \frac{1}{2}b_{n+1} \cos(\alpha_{n+1}), \\ \rho_3 &= \rho_5 - \rho_4 = b_n \cos(\alpha_n) - b_{n+1} \cos(\alpha_{n+1}). \end{aligned} \tag{4.6}$$

By substituting Eqs. (4.6, 4.5) in Eq. (4.4) and arranging the equation, we obtain:

$$R_{n+1} = R_n + \frac{1}{2}c_n \sin(\alpha_n) + \frac{1}{2}b_n \cos(\alpha_n) + \frac{1}{2}c_{n+1} \sin(\alpha_{n+1}) - \frac{1}{2}b_{n+1} \cos(\alpha_{n+1}). \tag{4.7}$$

To determine the Z coordinate of Halbach ring number n, denoted as z_n, we extract it from Fig. 4.7 relative to the reference point z_i using the following expression:

$$z_n = z_i + \frac{1}{2}c_n \cos(\alpha_n) - \frac{1}{2}b_n \sin(\alpha_n). \tag{4.8}$$

we also deduce the expression for z_{n+1}:

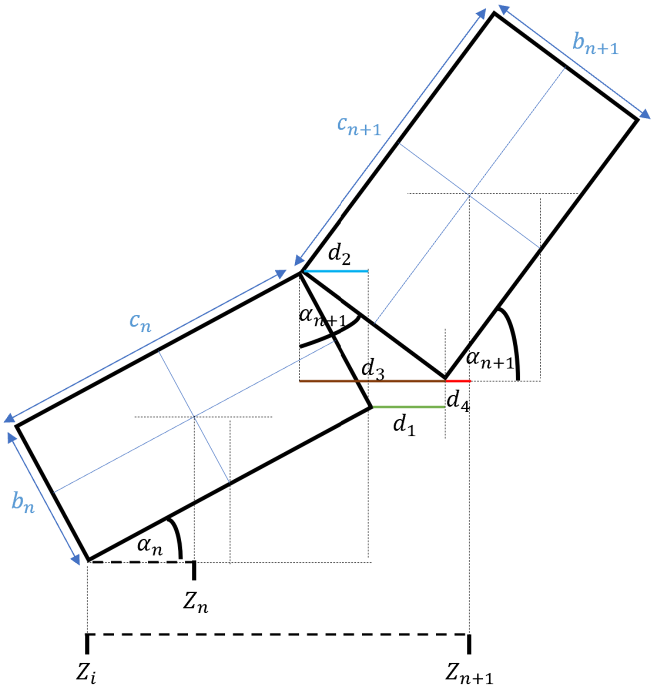

Figure 4.7: Illustration of Z_{n+1} calculation for $\alpha_{n+1} > \alpha_n$ with positive angles.

$$z_{n+1} = z_i + c_n \cos(\alpha_n) + d_4 + d_1, \tag{4.9}$$

where:

$$d_1 = d_3 - d_2 = b_{n+1} \sin(\alpha_{n+1}) - b_n \sin(\alpha_n), \tag{4.10}$$

$$d_4 = \frac{1}{2} c_{n+1} \cos(\alpha_{n+1}) - \frac{1}{2} b_{n+1} \sin(\alpha_{n+1}). \tag{4.11}$$

Substituting Eq. (4.11) and Eq. (4.9) into Eq. (4.8) and reorganizing the terms yields the following expression:

$$z_{n+1} = z_n + \frac{1}{2} c_n \cos(\alpha_n) - \frac{1}{2} b_n \sin(\alpha_n) + \frac{1}{2} c_{n+1} \cos(\alpha_{n+1}) + \frac{1}{2} b_{n+1} \sin(\alpha_{n+1}). \tag{4.12}$$

4.3 Magnetic Field Calculation of the PMZS

In Section 4.1, we discussed the equations for calculating the magnetic field vector $\vec{B}$ with respect to the permanent magnet's reference frame. To compute the magnetic field at an arbitrary point (x, y, z) in the laboratory frame, we must first transform to the magnet's reference frame and subsequently reverse the transformation to return to the lab frame.

Here is a step-by-step summary of the process for calculating the magnetic field:

Angles		Radial Coordinate	Axial Coordinate
sign	size		
$\alpha_{n+1} > 0,\ \alpha_n > 0$	$\alpha_{n+1} > \alpha_n$	$R_{n+1} = R_n + \frac{1}{2}c_n \sin(\alpha_n) + \frac{1}{2}b_n \cos(\alpha_n) + \frac{1}{2}c_{n+1} \sin(\alpha_{n+1}) - \frac{1}{2}b_{n+1} \cos(\alpha_{n+1})$	$z_{n+1} = z_n + \frac{1}{2}c_n \cos(\alpha_n) - \frac{1}{2}b_n \sin(\alpha_n) + \frac{1}{2}c_{n+1} \cos(\alpha_{n+1}) + \frac{1}{2}b_{n+1} \sin(\alpha_{n+1})$
$\alpha_{n+1} > 0,\ \alpha_n < 0$	$\alpha_{n+1} > \alpha_n$		
$\alpha_{n+1} < 0,\ \alpha_n < 0$	$\alpha_{n+1} > \alpha_n$		
$\alpha_{n+1} > 0,\ \alpha_n > 0$	$\alpha_{n+1} = \alpha_n$		
$\alpha_{n+1} < 0,\ \alpha_n < 0$	$\alpha_{n+1} = \alpha_n$		
$\alpha_{n+1} < 0,\ \alpha_n > 0$	$\alpha_{n+1} < \alpha_n$	$R_{n+1} = R_n + \frac{1}{2}c_n \sin(\alpha_n) - \frac{1}{2}b_n \cos(\alpha_n) + \frac{1}{2}c_{n+1} \sin(\alpha_{n+1}) + \frac{1}{2}b_{n+1} \cos(\alpha_{n+1})$	$z_{n+1} = z_n + \frac{1}{2}c_n \cos(\alpha_n) + \frac{1}{2}b_n \sin(\alpha_n) + \frac{1}{2}c_{n+1} \cos(\alpha_{n+1}) - \frac{1}{2}b_{n+1} \sin(\alpha_{n+1})$
$\alpha_{n+1} > 0,\ \alpha_n > 0$	$\alpha_{n+1} < \alpha_n$		
$\alpha_{n+1} < 0,\ \alpha_n < 0$	$\alpha_{n+1} < \alpha_n$		

Table 4.1: Radial and axial coordinates for the Halbach rings

- **Defining the Transformation Matrix from Lab Frame to Magnet Frame:**

  The Halbach configuration employs a sequence of three rotational matrices for each magnet: an initial rotation about the z-axis by θ_i, which aligns the magnet's magnetization vector, followed by a rotation about the x-axis by α_n, and a subsequent rotation about the z-axis again by θ_i. The angle θ_i is defined as $\theta_i = (i-1)\cdot\frac{2\pi}{8}$, where i ranges from 1 to 8, corresponding to the eight magnets in a single Halbach ring. The angle α_n is defined for each of the N Halbach rings, where n varies from 1 to N.

  In the adopted left-handed coordinate system, the composite transformation matrix for the nth ring and the ith magnet, denoted as $R_n(i)$, is constructed as follows:

$$R_n(i) = R_z(\theta_i)\cdot R_x(\alpha_n)\cdot R_z(\theta_i) =$$

$$\begin{bmatrix} \cos(\theta_i) & \sin(\theta_i) & 0 \\ -\sin(\theta_i) & \cos(\theta_i) & 0 \\ 0 & 0 & 1 \end{bmatrix} \cdot \begin{bmatrix} 1 & 0 & 0 \\ 0 & \cos(\alpha_n) & \sin(\alpha_n) \\ 0 & -\sin(\alpha_n) & \cos(\alpha_n) \end{bmatrix} \cdot \begin{bmatrix} \cos(\theta_i) & \sin(\theta_i) & 0 \\ -\sin(\theta_i) & \cos(\theta_i) & 0 \\ 0 & 0 & 1 \end{bmatrix}$$

$$\begin{bmatrix} \cos^2(\theta_i) - \cos(\alpha_n)\sin^2(\theta_i) & \cos(\theta_i)\sin(\theta_i) + \cos(\alpha_n)\cos(\theta_i)\sin(\theta_i) & \sin(\alpha_n)\sin(\theta_i) \\ -\cos(\theta_i)\sin(\theta_i) - \cos(\alpha_n)\cos(\theta_i)\sin(\theta_i) & \cos(\alpha_n)\cos^2(\theta_i) - \sin^2(\theta_i) & \sin(\alpha_n)\cos(\theta_i) \\ \sin(\alpha_n)\sin(\theta_i) & -\sin(\alpha_n)\cos(\theta_i) & \cos(\alpha_n) \end{bmatrix}$$

  This matrix effectively transforms vectors from the lab frame to the magnet frame.

- **Expressing the Translation Vector T:**

  For the nth ring and the ith magnet, the translation vector $\vec{T_n}(i)$ is essential for understanding the location of each magnet's center in the Halbach ring relative to the lab frame:

$$\vec{T_n}(i) = \begin{bmatrix} \sin(\theta_i)R_n(i) \\ \cos(\theta_i)R_n(i) \\ z_n \end{bmatrix}$$

- **Calculating the Distance Vector d:** To determine the magnetic field at a point $r = (x, y, z)$ in the lab frame, the distance from this point to the center of the magnet is represented by the vector $\vec{d}$:

$$\vec{d_n}(i) = \begin{bmatrix} x - \sin(\theta_i)R_n(i) \\ y - \cos(\theta_i)R_n(i) \\ z - z_n \end{bmatrix}$$

- **Transforming d to the Magnet Frame:** The transformation of $\vec{d}$ to the magnet frame is achieved by:

$$\vec{d_n^m}(i) = R_n^{-1}(i) \cdot \vec{d_n}(i)$$

- **Substituting $\vec{d_n^m}(i)$ into Magnet Frame Equations (see Section 4.1):** The magnetic field equations from Section 4.1 are applied using $\vec{d_n^m}(i)$.

- **Transforming the Magnetic Field to the Lab Frame:** The resulting magnetic field in the lab frame is given by:

$$\vec{B}_{\text{lab}} = R_n(i) \cdot \vec{B}_{\text{magnet}}$$

4.4 Optimization Procedure for the PMZS

Starting with an ideal magnetic field graph, our objective was to simulate a Zeeman slower constructed from permanent magnets, aiming to closely match the resulting magnetic field with the ideal one. This journey was marked by numerous challenges, but we persevered in our search for an effective solution. Notably, we are not aware of any other laboratories worldwide that have developed a Zeeman slower for ^{7}Li using permanent magnets. Although we drew insights from prior research on other elements, adapting existing designs proved challenging due to the specific requirements of our lithium Zeeman slower. Namely, our choice to employ a spin-flip Zeeman slower further compounded the complexity, and given the need for a considerably high magnetic field Amplitude, around 1000 Gauss, to achieve our objectives.

Initially, we adopted the design concept proposed in [7], their design was built to cool rabidium ^{87}Rb which mainly revolves around the utilization of elongated permanent magnets set at a single angle, in order to simplify mechanical construction. You can refer to our initial design in Fig. 4.8, which visually illustrates the concept outlined in the paper.

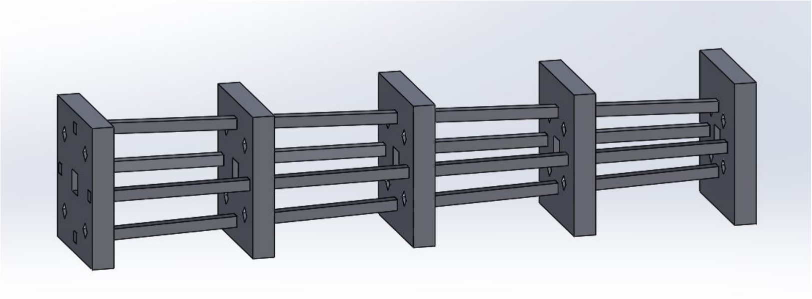

Figure 4.8: Conceptual representation of the initial design inspired by [7].

The construction of a Zeeman slower for rubidium is notably facilitated by the possibility of employing a single angle in its mechanical design. However, this approach is not as effective for lithium as a result of its significantly lower mass.

To understand how mass impacts the design of a Zeeman slower, consider the relationship that governs the amplitude of the magnetic field in such a device, derived from Eq. (4.13):

$$\Delta B = \frac{\hbar k(v_c - v_f)}{\mu_B}. \tag{4.13}$$

This equation indicates that the amplitude of the magnetic field in a Zeeman slower directly proportional to the capture velocity.

For ^{7}Li, assuming a capture velocity of 900 m/s at a temperature of 300 $°C$ and employing Eq. (3.2), we find that the Zeeman slower will decelerate approximately 12% of the atoms that leave the oven. In contrast, for ^{87}Rb with the same capture velocity, the Zeeman slower can slow down about 99% of the exiting atoms.

This substantial difference is mainly due to the mass of ^{87}Rb, which is about 12 times higher than that of lithium. Consequently, when a Zeeman slower for rubidium is designed, opting for a lower capture velocity can still result in a significant proportion of atoms being slowed, which simplifies the mechanical design process considerably.

Subsequently, we explored an alternative design inspired by [8], which centered on the use of a long permanent magnet rotated at an angle relative to the x-axis. This design was originally developed for ytterbium atoms and also incorporated a spin-flip Zeeman slower, aligning with our objectives. However, the magnetic field amplitude generated by their Zeeman slower was limited to 600 Gauss, significantly lower than our required amplitude. After making efforts to optimize this approach, we found that the resulting magnetic field deviated considerably from the ideal configuration.

Our innovative approach involves utilizing a large number of cuboid small magnets, introducing an increased flexibility that allows us to attain the desired magnetic field configuration effectively. However, it should be noted that this approach also introduces a greater mechanical complexity to the structure, which will be discussed further in this thesis.

4.5 Simulated Magnetic Field Parameters

To commence the optimization process, it is essential to familiarize ourselves with the parameters required for simulating the magnetic field of the Zeeman slower. These parameters include:

- N: The total number of Halbach rings.
- B_r: The remanent magnetic field strength for each Halbach ring.
- α: The angle of rotation of each Halbach ring around the x-axis.
- Z_1: The axial coordinate Z for the first Halbach ring.
- R_1: The radius of the first Halbach ring.
- The size of the magnets within every Halbach ring, including their length (a), width (b), and height (c).

Note that after determining the values of R_1 and Z_1, along with the angles α for all magnets, we can easily calculate R_n and Z_n for the remaining magnets using the expressions provided in the previous chapter; see table 4.1.

We have design constraints that limit the options for our optimization parameters. First, we restrict the angle α to be within the range of $-\pi/2$ to $\pi/2$ for ease of manufacturing. Additionally, due to the limitations of available cuboid permanent magnets in the industry, we source our magnets from the company "HKCM Engineering," which provides a predefined list of magnet sizes. You can find the list at the following link: HKCM Engineering Cuboid Magnets. This list contains 904 options.

To ensure a more uniform magnetic field, we intentionally select cuboid magnets with identical width and length, denoted as ($a = b$). Moreover, we seek magnets with small heights (c), which significantly reduces the number of available options and simplifies the optimization process.

During optimization, we explore all the options available for the sizes of the magnets within the given constraints. The magnets within the same Halbach ring are identical but not necessarily identical to magnets in other Halbach rings. As part of the optimization process, we consider the magnet sizes and their remanent magnetic field strengths (B_r) obtained from the company and adjust the values of z_1 and R_1 for the first magnet, along with the angles α for all N Halbach rings. Our goal is to achieve a magnetic field configuration that closely matches the ideal magnetic field.

4.6 Ideal Magnetic Field Parameters

In this section, we discuss the parameters that need to be optimized—v_c, η, and δ—to calculate the ideal magnetic field. These parameters are specified and defined in Table 4.2 below.

Our goal is to minimize the divergence of the atomic beam following the Zeeman slower, thereby enabling effective capture by the magneto-optical trap (MOT). This involves reducing the transverse velocity, with the considerations for this detailed in the following subsection.

4.6.1 Considerations Regarding Transverse Velocity

- **Ballistic Expansion at the Final Stage (After the Slower):** The distance $d_{\text{prop}} \approx 10$ cm represents the propagation length from the Zeeman slower to the MOT region, and the radius of the MOT region $r_{\text{MOT}} \approx 1$ cm. For atoms exiting the Zeeman slower with a final velocity $v_f \approx 30$ m/s, the transverse velocity v_{tr} is determined by equating the time for longitudinal travel over d_{prop} and transverse travel over r_{MOT}, resulting in:

  $$v_{\text{tr}} = v_f \frac{r_{\text{MOT}}}{d_{\text{prop}}} \approx 3 \text{ m/s}.$$

  Selecting $v_f = 30$ m/s ensures a minimized transverse velocity.

- **Transverse Heating During Propagation in the Zeeman Slower:** The recoil velocity is $v_{\text{rec}} = \frac{\hbar k}{m} = 0.085$ m/s. Assuming capture velocity $v_{\text{c}} = 900$ m/s, the number of photons N_{ph} required to decelerate the atoms to v_f is given by $N_{\text{ph}} = \frac{v_{\text{c}} - v_f}{v_{\text{rec}}} \approx 10^4$. Consequently, the transverse velocity v_{tr} due to heating is:

  $$v_{\text{tr}} = \sqrt{N_{\text{ph}}} v_{\text{rec}} \approx 8.5 \text{ m/s}.$$

These considerations are crucial for fine-tuning the operational parameters of the Zeeman slower to ensure compatibility with the MOT's capturing efficiency.

4.6.2 Parameter Flexibility in Ideal Magnetic Field Calculations

In the design of the Zeeman slower, we are afforded a measure of flexibility in choosing certain parameters that define the ideal magnetic field. Notably, within the proposed range, variations in these parameters do not markedly affect the Zeeman slower's overall efficacy. Such flexibility is instrumental in fine-tuning the congruence between the simulated and ideal magnetic fields. The parameters under consideration include:

1. **Security Coefficient η:** This coefficient accounts for the imperfections in the Zeeman slower. We can adjust η between 0.45 and 0.6, but it must remain below 1. In prior experiments with a conventional wire-based Zeeman slower, we used $\eta = 0.7$. This value was less than optimal, considering the various imperfections encountered in constructing the Zeeman slower. A lower η value aligns better with theoretical predictions while compensating for these imperfections. However, a reduced η increases the length of the Zeeman slower, which requires careful consideration to avoid impractically long slowers, as they occupy too much space on our optical table and adversely affect the angle at which atoms are captured by the MOT.

2. **Capture Velocity v_c:** The chosen capture velocity of 900 m/s results in a relatively low transverse velocity, which can be further diminished with pre-slower collimation. Opting for a higher capture velocity increases not only the transverse velocity but also the required length of the Zeeman slower. Conversely, a velocity that is too low impedes the number of atoms that can be effectively slowed. We have determined that a capture velocity within the range of 800 m/s to 900 m/s results in a minor difference in the number of the slowed atoms, thus allowing flexibility in selecting this parameter.

3. **Detuning (δ):** The laser is tuned to a point 401.5 MHz away from the atomic transition frequency. We utilize Acousto-Optic Modulators (AOMs) set to 80 MHz. This sets the detuning value δ to $401.5 - 2 \times 80 = 241.5$ MHz. We can also fine-tune the AOM to adjust the detuning by ±10 MHz, providing us the option to select a detuning within the range of 231.5 MHz to 251.5 MHz for our ideal magnetic field calculations.

In conclusion, these parameters offer a level of adaptability that is crucial for optimizing the performance of the Zeeman slower amidst practical limitations and imperfections, thereby improving the alignment with the ideal magnetic field model. The final optimized parameters for the ideal magnetic field are outlined in Table 4.2.

4.7 Optimization Results

The central objective of our optimization process was to minimize the difference between the ideal magnetic field and the simulated magnetic field, which is produced using an array of permanent magnets within the Zeeman slower. This optimization process involved iterative adjustments to critical parameters during the calculation of the ideal magnetic field, encompassing variables such as η, $v_{capture}$, and δ. Simultaneously, we fine-tuned parameters governing the simulated magnetic field within the

Parameter	Symbol	Value
Mass	m	$1.1650341 \times 10^{-26}\,\mathrm{kg}$
Wavelength	λ	$670.975 \quad [\mathrm{nm}]$
Magnetic moment	$\mu_{\prime}$	$-1.3996\,[\mathrm{MHz/G}]$
Wavenumber	$k = \frac{2\pi}{\lambda}$	$9.3643 \times 10^{6}\,[\mathrm{rad/m}]$
Linewidth of the transition	Γ	$2\pi \times 5.87123\,\mathrm{MHz}$
Maximum deceleration	$a_{max} = \frac{\hbar k \Gamma}{2m}$	$1.5635 \times 10^{6}\,\mathrm{m\,s^{-2}}$
Capture velocity	v_c	$850\,\mathrm{m\,s^{-1}}$
“Security” coefficient to allow imperfections	η	0.48
Detuning	δ_0	$-244.93405\,\mathrm{MHz}$
Final velocity	v_f	$30\,\mathrm{m\,s^{-1}}$
Length of Zeeman slower	$L = \frac{v_c^2 - v_f^2}{2\eta a_{max}}$	$47.3\,\mathrm{cm}$
Length of Zeeman for $v_f = 0$	$L_{\mathrm{stop}} = \frac{v_c^2}{2\eta a_{max}}$	$47.36\,\mathrm{cm}$
Field offset	$B_0 = \frac{\hbar \delta_0}{\mu_{\prime}}$	$175\,\mathrm{G}$
Field amplitude	$B_L = \frac{\hbar k v_c}{\mu_{\prime}}$	$-905.1102\,\mathrm{G}$

Table 4.2: Zeeman slower design parameters

Zeeman slower constructed from permanent magnets, specifically, we varied the dimensions (R_1 and z_1) of the first Halbach ring and manipulated the rotation angles (α) of the Halbach rings. This procedure was carried out across multiple iterations, each time with different sizes of cuboid permanent magnets, to select the set of parameters that resulted in the minimal difference between the calculations of the ideal and simulated magnetic fields. In the final iteration, detailed parameters for the ideal magnetic field calculations are summarized in Table 4.2. Our optimized design comprised a total of 19 Halbach rings, each ring composed of eight individual magnets, resulting in a requirement for a total of 152 permanent magnets. The precise specifications of these magnets are documented in Table 4.3. Figure 4.9 provides a visual representation of the composite design formed by these permanent magnets, illustrating the intricate and challenging nature of constructing such a complex structure. The development of this Zeeman slower has provided invaluable insights, and in the subsequent chapter, we will delve into a comprehensive explanation of the mechanical structure of the

Zeeman slower.

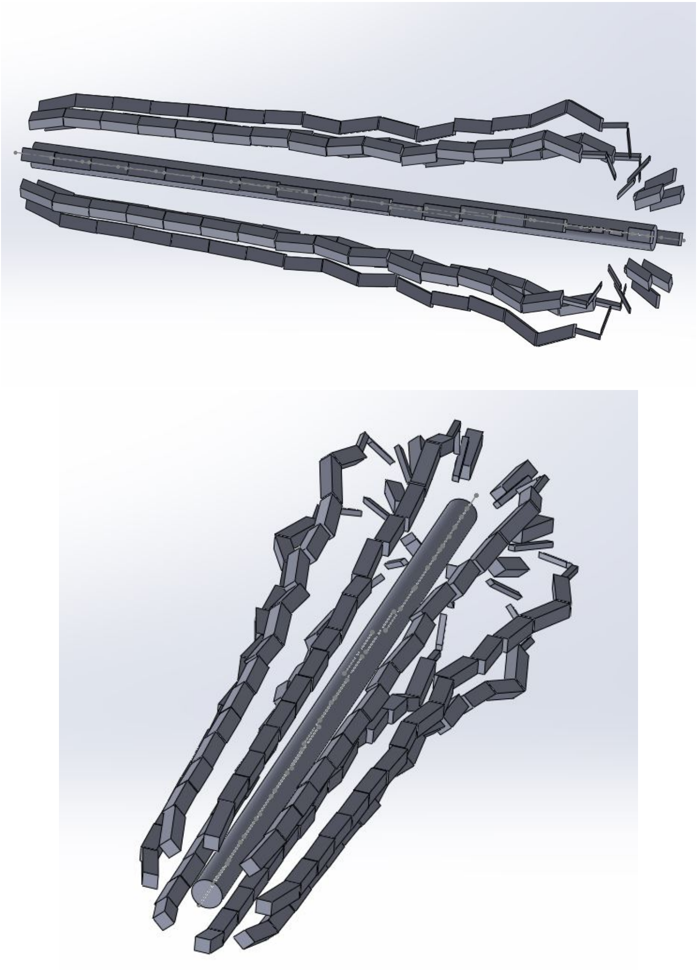

Figure 4.9: Two views of permanent magnets design.

4.8 Analysis of Magnetic Field Profiles in the PMZS: Simulated vs. Ideal Comparisons

This section introduces two graphical representations derived from the optimization process within the context of a Zeeman slower. The first graph, shown in Fig. 4.10, presents the profiles of both the simulated magnetic field ($B_{\text{simulated}}$) and the ideal magnetic field (B_{ideal}). These profiles are plotted as functions of the axial coordinate Z, which corresponds to the direction of atomic propagation within the Zeeman slower.

The second graph, illustrated in Fig. 4.11, is dedicated to highlighting the discrepancies between these magnetic field profiles along the axial coordinate. This graph offers a focused view on the magnetic field error up to the point where $Z = L$, marking the end of the Zeeman slower—a region of particular interest for evaluating field accuracy. An analysis of the second graph reveals an average deviation of 0.4142 G between the simulated and ideal magnetic fields along the axial length Z. This finding leads to a crucial consideration: determining the acceptable level of error between these two magnetic field representations, a topic that will be further explored in section 5.2.

Halbach ring	$\boldsymbol{\alpha_n}$ **(°)**	z_n **(mm)**	R_n **(mm)**	**Sign**	**a (mm)**	**b (mm)**	**c (mm)**	**Br**
1	16.68	-21.32	41.51	-1	10	10	30	1.28
2	3.66	9.59	47.05	-1	10	10	30	1.28
3	1.31	39.85	48.36	-1	10	10	30	1.28
4	2.72	70.00	49.42	-1	10	10	30	1.28
5	2.84	99.98	50.88	-1	10	10	30	1.28
6	-1.28	130.47	51.29	-1	10	10	30	1.28
7	7.76	161.44	53.04	-1	10	10	30	1.28
8	-4.87	192.80	53.84	-1	10	10	30	1.28
9	13.51	224.59	56.24	-1	10	10	30	1.28
10	-7.54	256.62	57.91	-1	10	10	30	1.28
11	19.04	288.91	61.16	-1	10	10	30	1.28
12	0.01	320.39	66.44	-1	10	10	30	1.28
13	15.90	351.75	70.82	-1	10	10	30	1.28
14	23.46	380.82	81.22	-1	10	10	30	1.28
15	-19.49	413.89	82.36	-1	10	10	20	1.17
16	21.91	442.31	81.19	1	10	10	20	1.17
17	-76.35	463.46	70.32	1	4	4	25	1.17
18	-67.02	474.97	49.66	1	10	10	20	1.17
19	28.01	494.60	37.71	1	10	10	20	1.17

Table 4.3: Geometric arrangement parameters for the PMZS

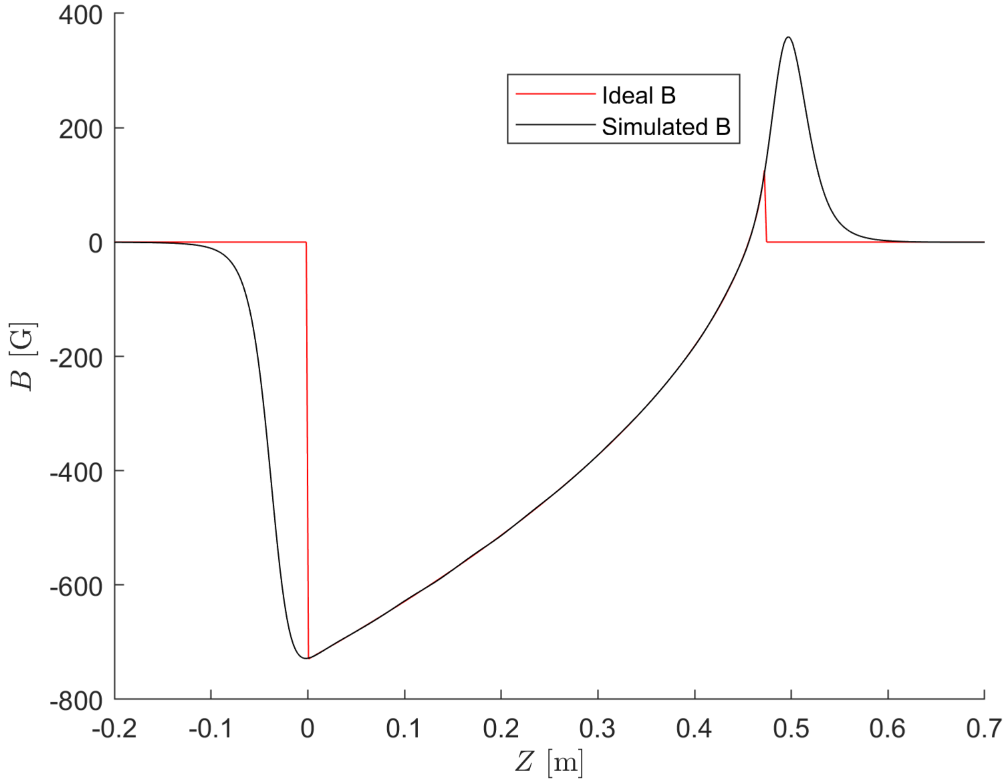

Figure 4.10: Simulated magnetic field vs ideal magnetic field.

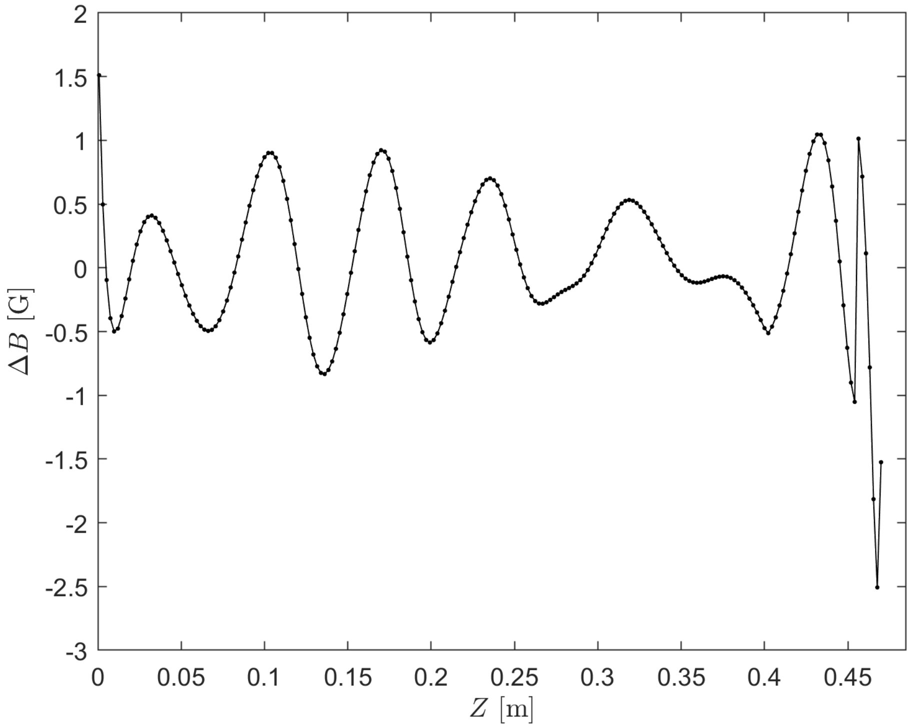

Figure 4.11: Deviation between simulated and ideal magnetic fields.

Chapter 5

Constructing the PMZS: Mechanical Design and Resulting Magnetic Field Measurements

5.1 Mechanical Design

We use permanent magnets in a Halbach configuration to produce the magnetic field required for the Zeeman slower. A three-dimensional model of the Zeeman slower based on permanent magnets is illustrated in Fig. 5.1. The model was created using the SolidWorks CAD environment. It comprises two side holders supporting eight magnet holders, divided into four of type I and four of type II, ensuring the Halbach symmetry. Here, types I and II respectively denote the non-rotated and 45°-rotated magnets. Each magnets holder accommodates 19 rectangular cuboids permanent magnets arranged according to the optimized position and orientation, as detailed in Table (4.3) above. The optimized configurations of the magnets result in a total length of the Zeeman slower of 555 [mm]. To address the intricate design complexity and minimize manufacturing costs while maintaining minimal tolerances, the holders components were 3D printed using PLA material. The design, manufacturing and assembly processes involved several challenging phases, which will be discussed in the following sections.

The primary challenge in Zeeman slower design is enabling attachment to the fixed vacuum tube while maintaining Halbach symmetry. This was achieved by dividing the Zeeman slower into upper and lower parts, as shown in Fig. 5.2. The upper part comprises five magnet holders, while the lower part incorporates three magnet holders. These two sections are pressed against each other using four M3 bolts to achieve the desired configuration.

The eight magnets holders were affixed to the side holders with a 0.5 [mm] clear-

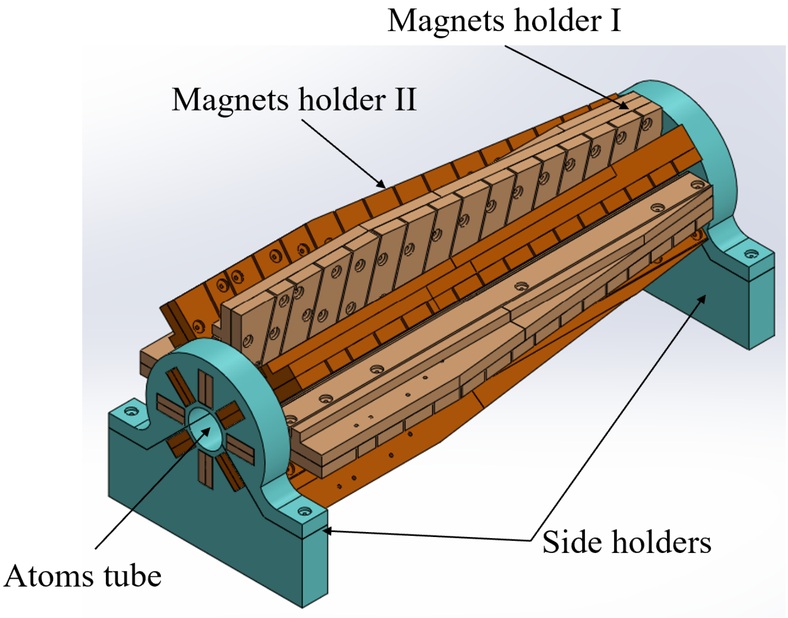

Figure 5.1: 3D model of the total assembly of the permanent magnets-based Zeeman slower.

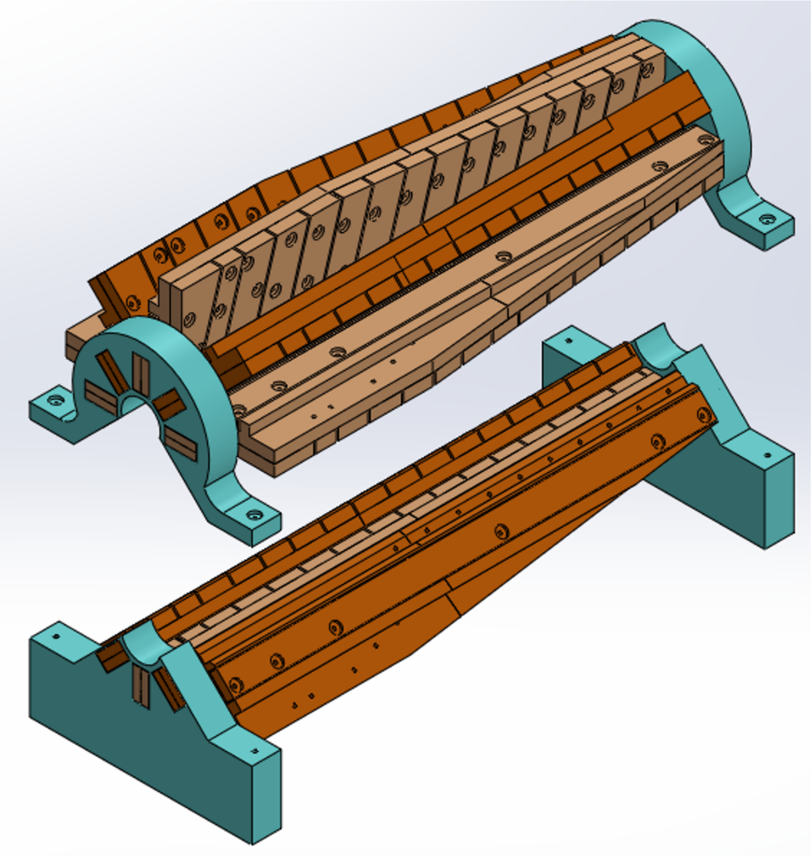

Figure 5.2: Upper and lower sub-assemblies of the permanent magnets-based Zeeman slower.

ance in each direction. The assembly of the side holder, along with an exploded view, is illustrated in panels (a) and (b) of Fig. 5.3. The design of the side holder posed a challenge in supporting the combined weight of the magnet holders and the 152 permanent magnets (8 * 19=152). This consideration is crucial, especially given that the side holder is divided into upper and lower parts. The solution involved strengthening the side holder by increasing its thickness to compensate for the limited material between the eight windows. The critical components of the Zeeman slower based on permanent magnets are the magnet holders, responsible for hosting magnets in their optimal locations and orientations. Three distinct rectangular cuboid permanent magnets were used: 10 mm × 10 mm × 30 mm, 10 mm × 10 mm × 20 mm, and 4 mm × 4 mm × 25 mm. These rectangular cuboid permanent magnets were adjusted differently for each magnet holder on the basis of its position in the Halbach array. This customization ensured the desired directionality of the resultant magnetic field.

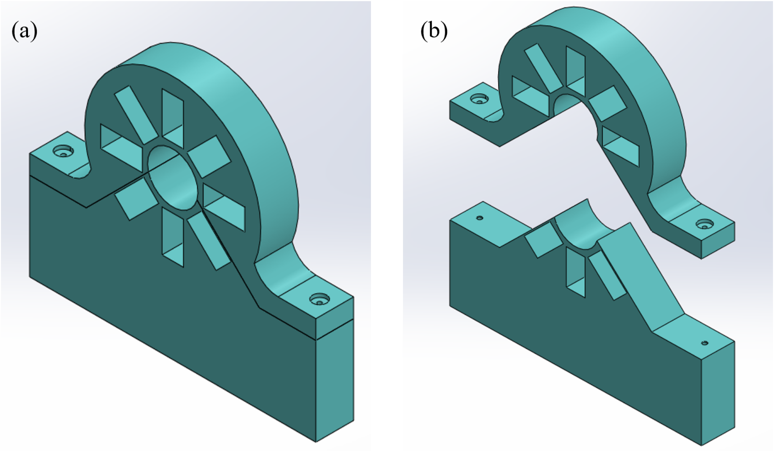

Figure 5.3: Side holder assembly: (a) Isometric view, and (b) exploded view.

The front and back views of magnet holder type I assembly are depicted in panels (a) and (b) of Fig. 5.4, respectively. The axial location for each permanent magnet is qualitatively labeled in the front view, as presented in panel (a) of the figure. Due to the length exceeding the available space of the 3D printer, manufacturing the magnet holders as a single unit was impossible. Consequently, each magnets holder was divided into two parts, right and left parts, as illustrated in panel (c) of Fig. 5.4. These left and right subassemblies were aligned using centering pins and holes and subsequently connected through a Teflon connection stick, as seen in panel (c) of Fig. 5.4.

Fully detailed front and back exploded views of magnets holder type I are presented in panels (a) and (b) of Fig. 5.5 respectively. In these views, the optimal location and orientation of the permanent magnets are clearly visible, with the positions of the magnets on the holder base plate engraved. The assembly process involved identifying the magnetization direction for the 19 permanent magnets in each holder, maintaining minimal manufacturing tolerances (0.1 mm) to ensure a secure assembly. To achieve the desired configuration, each magnet is secured against its cover using two M3 peek bolts.

The overall thickness of the magnet holders is constrained by the physical space available between the eight holders. Consequently, using a uniform thickness would result in bending failure due to the strong magnetic forces exerted between neighboring permanent magnets. This challenge was addressed by incorporating two reinforcement ribs on the base of the left and right parts of the magnets holder, as depicted in Fig. 5.5(b). These reinforcement ribs significantly improved the bending strength of the holders.

Similarly, Fig. 5.6 provides a comprehensive description of the assembly process for the magnet holder type II, where each magnet undergoes a 45-degree rotation around its axial axis. To complete the visual representation, an exploded view is presented in Fig. 5.7, offering similar insights as for magnets holder type I.

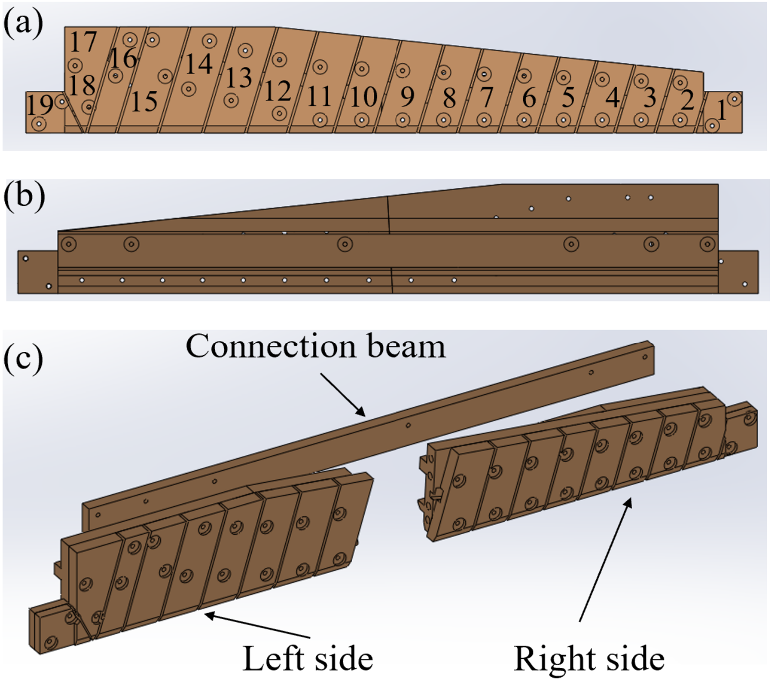

Figure 5.4: Assembly of magnets holder type I: (a) front view, (b) back view, and (c) exploded isometric view.

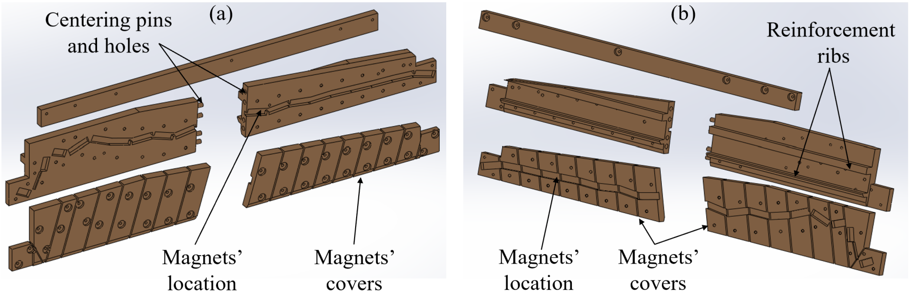

Figure 5.5: Exploded isometric view of magnets holder type I: (a) front view, and (b) back view.

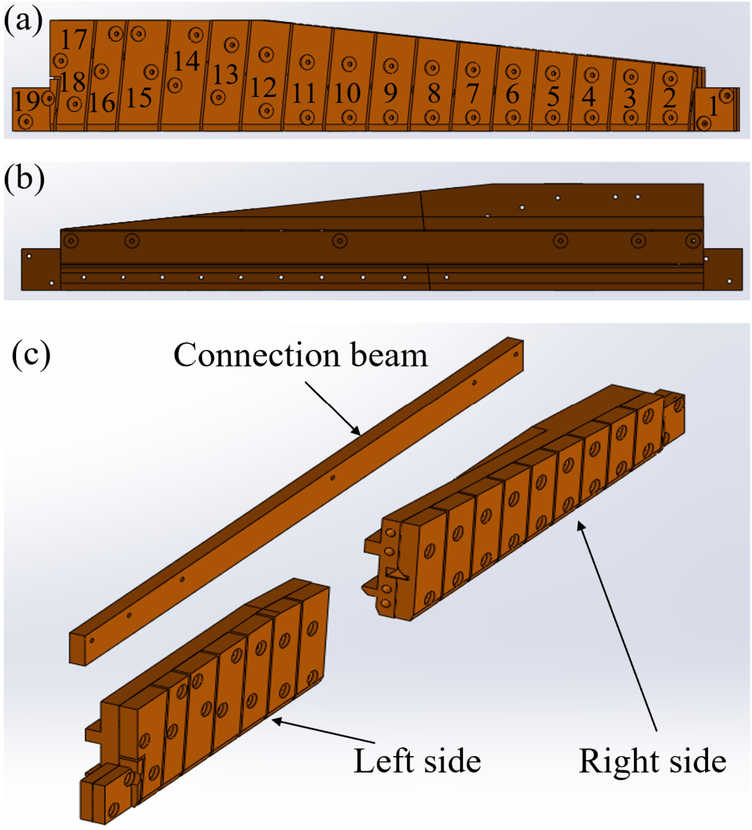

Figure 5.6: Assembly of magnets holder type II: (a) front view, (b) back view, and (c) exploded isometric view.

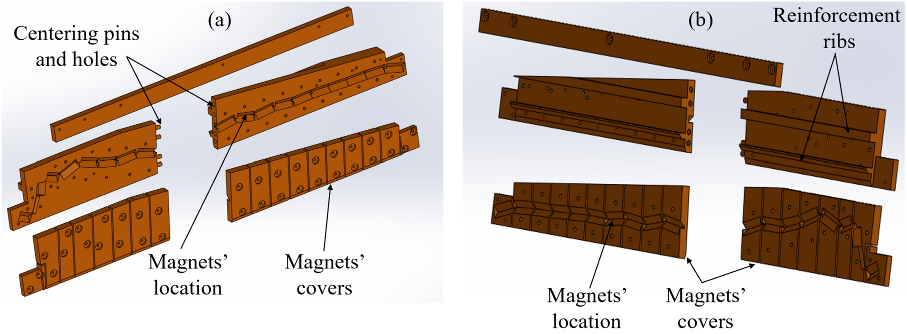

Figure 5.7: Exploded isometric view of magnets holder type II: (a) front view, and (b) back view.

Figures (5.8, 5.9) shows the actual assembly of the holders and Zeeman slower.

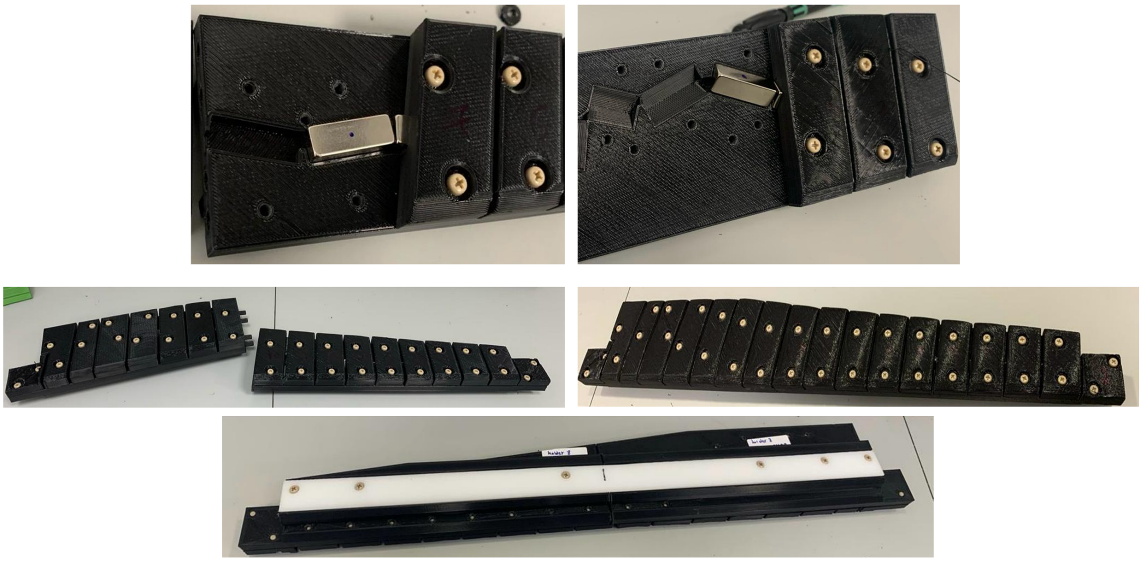

Figure 5.8: Assembly of magnets holder.

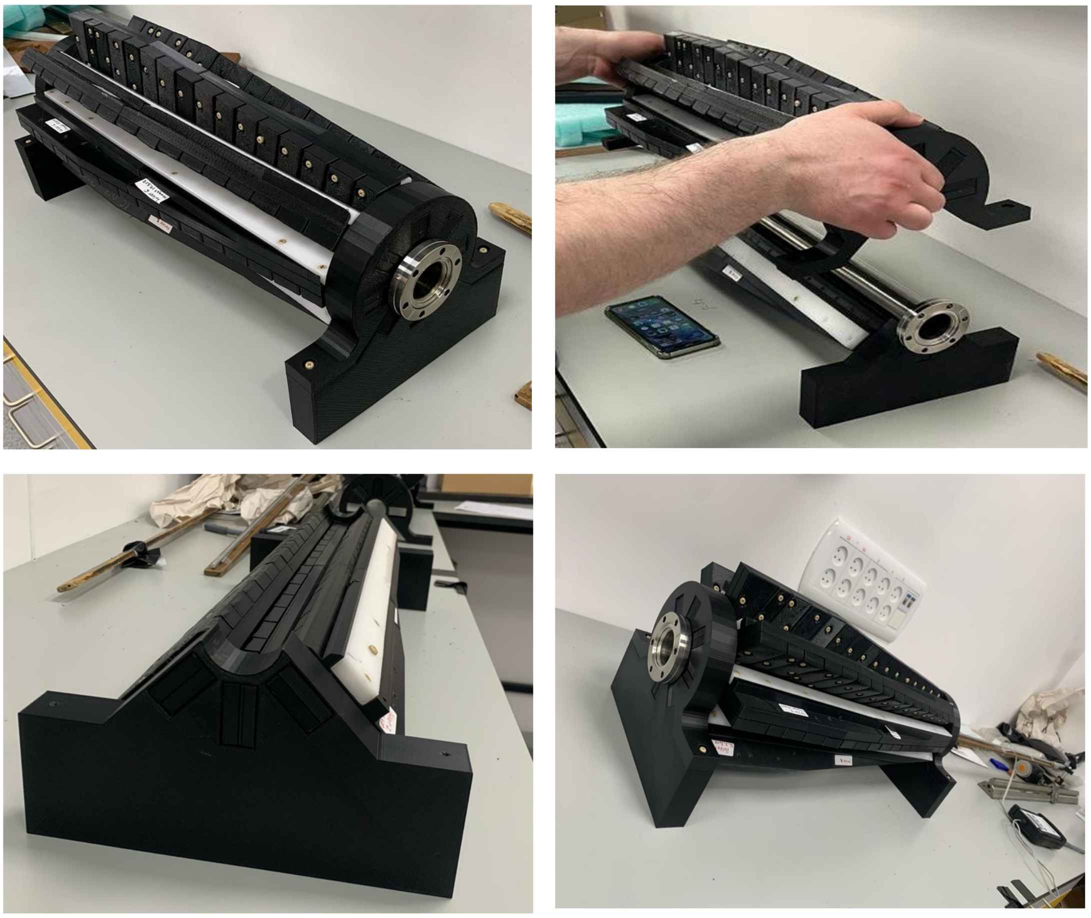

Figure 5.9: Total assembly of the permanent magnets-based Zeeman slower.

5.2 Tolerable Measured Magnetic Field Deviations

In Chapter 2, we discussed the force acting on atoms, which can be expressed as:

$$F = \hbar k \frac{\Gamma}{2} \frac{S(z)}{1 + S(z) + 4\left(\frac{\delta_{eff}}{\Gamma}\right)^2}, \tag{5.1}$$

here, $\delta_{eff} = \delta_0 + \frac{v}{c}\omega - \frac{\mu'(B(z))}{\hbar}$, and $S(z) = \frac{I}{I_{sat}}$, where I represents the intensity, and I_{sat} is the saturation intensity.

In an ideal scenario where the magnetic field profile perfectly compensates for the Doppler shift, δ_{eff} remains zero at any position z, resulting in the highest attainable force. We enforce this condition in Eq. (5.1)

$$F \leq \eta F_{\text{max}}, \tag{5.2}$$

where, $F_{\text{max}} = \hbar k \frac{\Gamma}{2} \frac{S(z)}{S(z)+1}$, and η serves as a 'security' coefficient, accounting for potential imperfections, where $\eta \leq 1$.

One such imperfection is the deviation of the magnetic field from the ideal profile, denoted as δB. To assess the tolerable extent of this deviation, we consider the total detuning:

$$\delta = \delta_{eff} \pm \delta_{dev} = \delta_0 + \frac{v}{c}\omega - \frac{\mu' B(z)}{\hbar} \pm \frac{\mu' \delta B(z)}{\hbar} = \pm \frac{\mu' \delta B(z)}{\hbar}. \tag{5.3}$$

To establish the criteria for acceptable magnetic field deviations, we substitute Eq. (5.3) into Eq. (5.2), leading to:

$$\eta \hbar k \frac{\Gamma}{2} \frac{S(z)}{S(z)+1} \leq \hbar k \frac{\Gamma}{2} \frac{S(z)}{1 + S(z) + 4\left(\frac{\pm \mu' \delta B(z)}{\hbar \Gamma}\right)^2}. \tag{5.4}$$

After rearranging Eq. (5.4), we find that the magnetic field deviation is expressed as:

$$\delta B(z) = \pm \frac{\hbar \Gamma}{2\mu'} \sqrt{\frac{(S(z)+1)(1-\eta)}{\eta}}. \tag{5.5}$$

Upon substituting our design parameters and constants of nature ($\mu' = 1.4$ MHz/Gauss, $\Gamma = 5.9$, and $S(0) = 25$), we calculate:

$$|\delta B_{\text{max}}(z)| = \frac{\hbar \Gamma}{2\mu'} \sqrt{26} \approx 10\,\text{Gauss} \tag{5.6}$$

It is important to note that the value of $S(0)$ corresponds to the beginning of the Zeeman slower. As we progress through the Zeeman slower, this parameter gradually decreases, indicating that the maximum deviation occurs at the starting point.

We find that the potential deviation of 10 Gauss is notably greater than the actual average deviation of 0.4 Gauss between the simulated magnetic field and the ideal field obtained through optimization. This strongly indicates the successful outcome of our optimization efforts.

5.3 Comparison of Measured and Simulated Magnetic Field Profiles in the PMZS

Here, we compare the actual and simulated magnetic field behaviors within the Zeeman slower. Figure 5.10 illustrates both the measured and the simulated magnetic field profiles as functions of the axial coordinate, Z. In addition, Fig. 5.11 highlights the difference between the simulated ($B_{\text{Simulated}}$) and the measured (B_{Measured}) magnetic fields.

A notable observation from these graphs is the discrepancy at the beginning of the Zeeman slower. Here, the error margin exceeds the maximum permissible error established in Subsection 5.2. However, beyond this initial region, the error within the remainder of the Zeeman slower is observed to be within acceptable limits, as per the previously calculated threshold.

In the next section, we will explore the factors causing these discrepancies. In the following chapter, we will examine in detail how these initial discrepancies impact the overall performance of the Zeeman slower using Monte Carlo simulations.

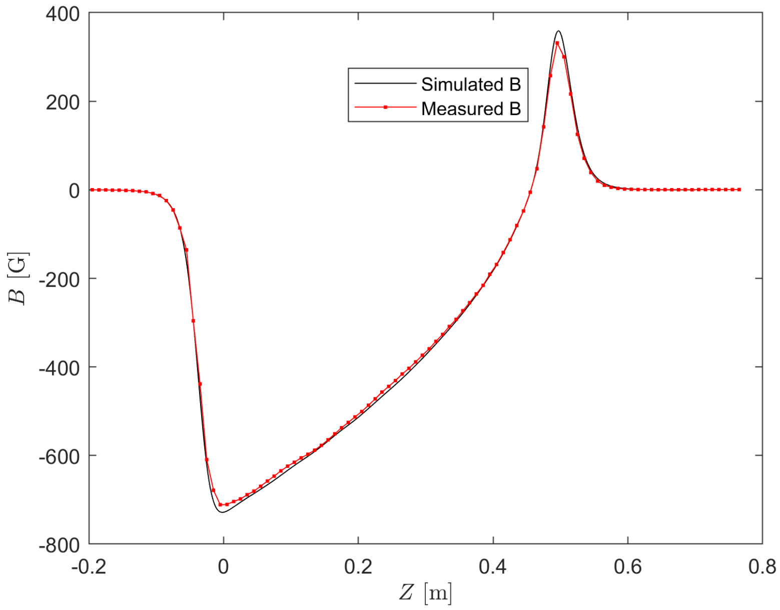

Figure 5.10: Simulated magnetic field vs Measured magnetic field.

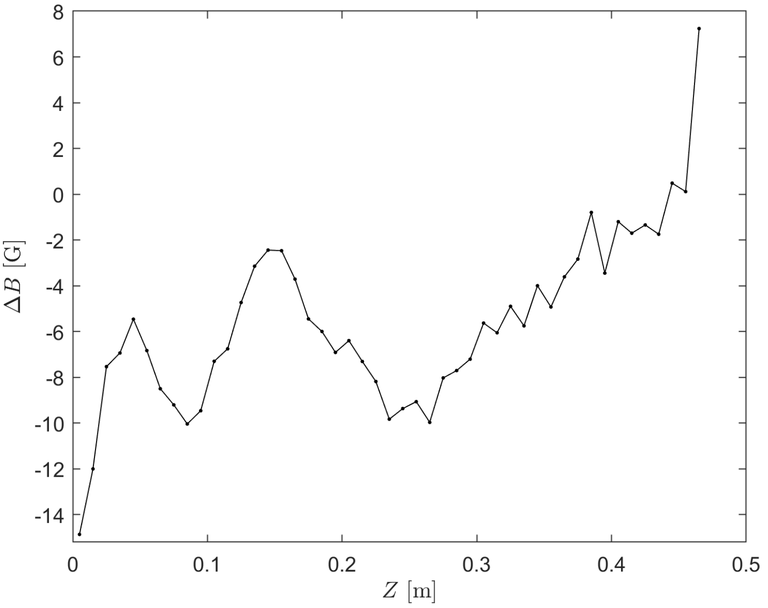

Figure 5.11: Deviation between simulated and measured magnetic fields: $\Delta B = B_{\text{Simulated}} - B_{\text{Measured}}$

5.3.1 Factors Influencing the Discrepancy Between Simulated and Measured Magnetic Fields in Zeeman Slower Construction

The construction of a Zeeman slower involves numerous factors that can significantly influence the precision of the resultant magnetic field. This section delineates these critical factors, highlighting their potential impacts on the accuracy of magnetic field measurements.

- **Impact of Halbach Ring Radius Variations:** A primary and previously unaccounted factor in our optimization model is the sensitivity of the magnetic field to changes in the radius of the Halbach ring. Given that manufacturing precision is within 1 mm, even marginal alterations in the radius of the initial Halbach ring (which consequentially affects the radii of subsequent rings) can critically modify the magnetic field. For instance, increasing the first Halbach ring's radius by 0.5 mm results in a reduction of the magnetic field strength by approximately 17 Gauss at $z = 0$.

- **Manufacturing Tolerances of Permanent Magnets:** The fabrication of cuboid permanent magnets, according to the manufacturer's stated tolerances, presents another influential factor. The dimensions of these magnets (width a, length b, height c) are subject to a manufacturing error tolerance of ± 2 mm, which could lead to significant variations in the magnetic field.

- **Magnet Placement and Physical Damage:** During the assembly of the Zeeman slower, the placement of cuboid magnets into their respective holders can be disrupted due to magnetic attraction to adjacent magnets. This occasionally results in physical collisions and subsequent scratching of the magnets, potentially impairing their magnetic performance.
- **Attractive Forces Between Adjacent Halbach Rings:** The significant attractive force between magnets located in adjacent Halbach rings is another factor that might affect the uniformity and strength of the magnetic field.
- **Limitations in 3D Printing Precision:** An additional overlooked factor in our optimization process is the precision limitations of 3D printing technology, particularly in achieving specific angular measurements. Although our optimization model could suggest angles with two decimal points, such precision is beyond the capability of standard 3D printing, impacting the accuracy of our magnetic field calculations.

In conclusion, considering these multifarious factors that can influence the precision of the magnetic field, the results obtained from the construction of the Zeeman slower are satisfactory. These insights not only underscore the complexity of accurately simulating magnetic fields but also highlight the importance of accounting for practical manufacturing limitations in theoretical models.

Chapter 6

Testing and characterization of the PMZS: Monte-Carlo Simulation

The purpose of a Zeeman slower is to decelerate a large fraction of atoms from a thermal beam with different, high initial velocities to the same low final velocity. The dissipative nature of the spontaneous force becomes evident, since the atoms are not decelerated by the same velocity but effectively 'bunched' into a particular final velocity. To assess the effectiveness of our Zeeman slower and to predict the final velocity distribution of atoms passing through a Zeeman slower, we want to apply the three-dimensional Monte Carlo simulation as suggested in [9].

6.0.1 The Differntial Equations

The acceleration given to an atom by many photons is given by:

$$a_z = \frac{\hbar k \Gamma}{2m} \frac{S(z)}{1 + S(z) + \left(\frac{4}{\Gamma^2}\right)\left(\delta_0 + k v_z - \frac{\mu' B_z}{\hbar}\right)^2}. \tag{6.1}$$

Notice that I kept the intensity-to-saturation intensity ratio, denoted as $S(z)$, constant at a value of $S_0 = 25$. Nevertheless, there are slight variations in S_z along the Zeeman slower. Importantly, these changes have minimal impact.

We start by rewriting the Eq. (6.1) in the following second order differential form:

$$\begin{aligned} \frac{d^2 z}{dt^2} &= \frac{\hbar k \Gamma}{2m} \frac{S_0}{1 + S_0 + \left(\frac{4}{\Gamma^2}\right)\left(\delta_0 + k\frac{dz}{dt} - \frac{\mu' B_z(x,y,z)}{\hbar}\right)^2}, \\ \frac{d^2 x}{dt^2} &= 0, \\ \frac{d^2 y}{dt^2} &= -9.8\,[\mathrm{m/s^2}]. \end{aligned} \tag{6.2}$$

Initial Conditions

The atoms leaving the oven are distributed according to a Maxwell-Boltzmann distribution.

To simulate the system, we begin by determining the number of atoms, denoted by N, that will participate in the simulation.

1. **Velocity Selection:** We implement a Maxwell-Boltzmann distribution for N atoms, considering only those with velocities up to $v = 880, \mathrm{m/s}$. Our focus is primarily on atoms with velocities at or below the capture velocity ($v_c = 850, \mathrm{m/s}$), which are the ones that can effectively be slowed down. However, by applying the Maxwell-Boltzmann distribution to velocities as high as 880 m/s, we aim to demonstrate the impact of the Zeeman slower on atoms whose initial velocities exceed the capture velocity.

2. **Position Initialization:** Set the initial conditions for the system, denoted by $x_0, y_0, z_0, v_{0,x}, v_{0,y}, v_{0,z}$, to solve Eq. (6.2).

   (a) *Radial Position Selection:* Randomly choose a radius, r, in the range $0 < r < r_{\text{oven}}$, where $r_{\text{oven}} = 2\,\text{mm}$ is the radius of the oven aperture.

   (b) *Angular Position Selection:* Randomly select angles θ and ϕ satisfying the conditions:

   $$0 < \phi < 2\pi,$$
   $$0 < \theta \leq \arctan\left(\frac{v_{r,max}}{v_{z,max}}\right)$$

   where $v_{z,max} = 850\,[m/sec]$ is the capture velocity and the max radial velocity is given by Eq. (3.10)

   (c) *Initial Position Calculation:* Compute the initial position coordinates:

   $$x_0 = r\cos(\phi),$$
   $$y_0 = r\sin(\phi).$$

3. **Initial Velocity Calculation:** After choosing random angles and radius r, ϕ, θ, calculate the initial velocities:

   $$v_{0,x} = v_{\text{oven}}\sin(\theta)\cos(\phi),$$
   $$v_{0,y} = v_{\text{oven}}\sin(\theta)\sin(\phi),$$
   $$v_{0,z} = v_{\text{oven}}\cos(\theta),$$

where v_{oven} is the initial velocity at the output aperture of the oven.

Now that we have figured out all of the initial conditions, we can solve Eq. (6.2)

6.1 Numerical Solution Along the Z Axis

To initiate the simulation of velocity profiles, we begin with an on-axis calculation. This simulation assumes that the atom travels exclusively along the z-axis so we assume the magnetic field is a function only of z. We focus on a range of velocities sampled from the Maxwell-Boltzmann distribution.

In this context, we simplify the calculation without considering the radial velocities (v_x) and (v_y). We also set $x = 0$ and $y = 0$, highlighting that the motion is confined to the z-direction.

Solution Using the Simulated Magnetic Field

The velocities as a function of z were determined through a solution of differential equations using the simulated magnetic field. It is important to note that the simulation results closely match those obtained with the ideal magnetic field, with the difference between them negligible, as demonstrated in Fig. 4.11.

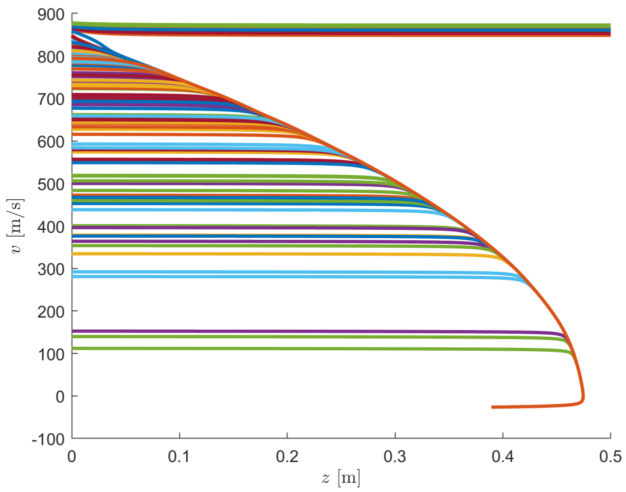

Figure 6.1: Velocity vs. z coordinate with simulated magnetic field, assuming on-axis motion.

Figure (6.1) shows the atom's velocity as a function of the position in the Zeeman slower for different initial velocities. As the Zeeman slower is designed for $v_0 = 850m/s$ which determines the length of the Zeeman slower, atoms with this initial velocity are resonant with the laser photons all along the Zeeman slower so the deceleration is constant until these atoms are stopped. Atoms with initial velocities larger than 850 m/s are far out of resonance with the laser, as a consequence of the Doppler effect. In these cases, the Zeeman effect is not able to compensate for the Doppler effect at any time, and there is practically no photon absorption. As a consequence, the velocity of these atoms does not vary in the Zeeman slower. The situation is completely different for atoms with initial velocities of less than 850 m/s, in this case, the interaction is non-resonant at the beginning of the Zeeman slower but at a particular point of the Zeeman slower the compensation of the Zeeman effect and the Doppler effect is perfect such that the interaction becomes resonant. From this point on, the interaction is always resonant until the atom stops. This is the explanation for why all the curves with initial velocities less than 850 m/s end up fitting each other.

As we observe, once the atoms reach the end of the Zeeman slower, they undergo acceleration in the negative direction, resulting in a negative velocity. This change in velocity can potentially cause the atoms to reverse their direction of motion. To prevent this undesirable outcome, it becomes necessary to make precise adjustments to both the power of the laser and the detuning parameters as we approach the end of the Zeeman slower. These adjustments are essential to ensure that we retain control over the atoms and avoid their loss.

Solution Using the Measured Magnetic Field.

In the following section, I employ the measured magnetic field data for the Zeeman slower. I create an interpolated function for the magnetic field using the measured results, which I then use to solve the differential equations. The objective here is to investigate the impact of the deviation between the simulated and measured magnetic fields, as depicted in Fig. 4.11, on the final velocity distribution at the end of the Zeeman slower.

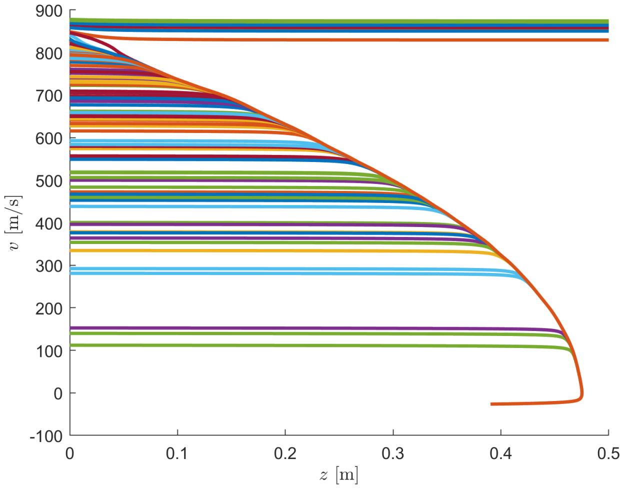

Figure 6.2: velocity vs. z coordinates with the interpolated magnetic field function, assuming on-axis motion.

Note that the velocity profile as a function of z is almost the same for both the measured and simulated magnetic fields, except that in the case of the measured magnetic field, the Zeeman slower initiates cooling for atoms at speeds of 845 m/s and below, whereas, for the simulated magnetic field, this process begins at 850 m/s.

6.2 General Numerical Solution (3D Motion Considered)

While previously neglecting the radial velocity, here I take it into account and see how the off-axis motion affects the slowing procedure.

The initial radial velocities are given in Fig. 6.3

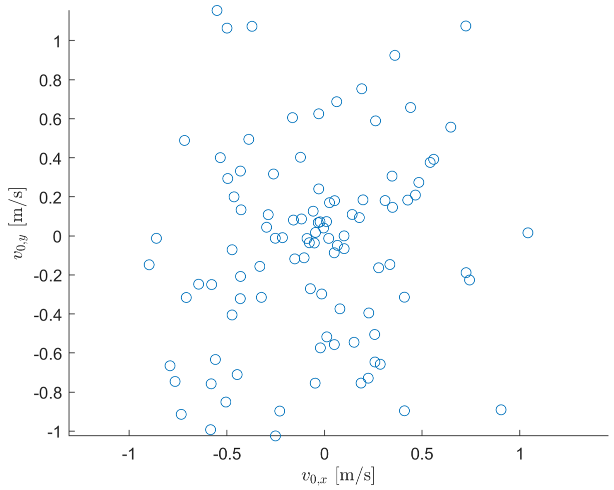

Figure 6.3: Random initial velocity v_x, v_y

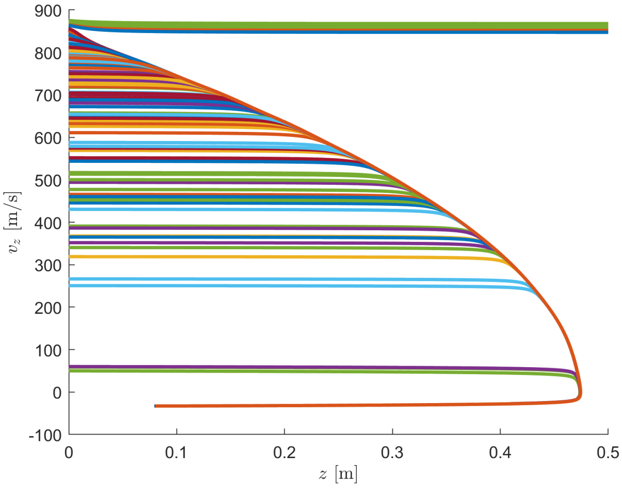

Figure 6.4: velocity vs. z coordinate with simulated magnetic field (3D motion considered)

Considering the negligible initial radial velocities, we obtain a velocity profile that closely resembles the one obtained when considering only on-axis motion.

Chapter 7

Zeeman Slower Performance: Velocity Measurements

The evaluation of the Zeeman slower performance is done by measuring the velocity distribution of the atoms at the MOT location. We perform this measurement using absorption spectroscopy and compare the results with and without the presence of the slowing laser beam.

7.1 Optical Density

For a weak laser beam passing an infinitesimal distance dl through the atoms, its intensity decreases according to Beer's law $I = I_0\, e^{-OD}$ where

$$OD(\delta, v) = n(v)\sigma(v, \delta)dl, \tag{7.1}$$

is the optical density per unit velocity, $n(v)$ is the atomic density per unit volume per unit velocity in the beam's direction, σ is the absorption cross section

$$\sigma(v, \delta) = \frac{\sigma_0}{1 + I/I_{sat} + 2(\delta/\Gamma)^2}, \tag{7.2}$$

where $\sigma_0 = \frac{3^*\lambda^2}{2\pi}$ is the resonance cross section, I_{sat} is the saturation intensity (for ^7Li equal to 2.56 mW/cm^2). This measurement is done at zero magnetic field, so the detuning is only affected by the laser frequency and the velocity component in the beam's direction $\delta = \omega_L - \omega_0 - \vec{k} \cdot \vec{v}$. The laser frequency is scanned at 50 Hz over some relevant section and its power is picked up after passing through the atoms by an amplified photodetector. We can make an approximation that the velocity distribution is sufficiently uniform over the beam path, and thus obtain the expression for its total power:

$$P = P_0\, e^{-L \int dv\, n(v)\sigma(v,\delta)} \tag{7.3}$$

where L is the total path length.

7.2 Measurement Apparatus

Figure 7.1 shows the configuration of the measurement apparatus. We define β as the angle between the probe laser and the general direction of propagation of the atoms $\hat{z}$, where $\beta > 0$ denotes the probe laser with positive z component of its wave vector. In theory, it would be optimal to have $\beta = 0$ to fully resolve the z component of the atoms' velocity. However, in this limit, the atomic density per velocity resolution range tends to zero and disappears below the measurement noise. In the other limit, as β approaches 90 degrees, the distribution compresses, and it becomes impossible to resolve small velocities that are relevant for our system evaluation. In order to have sufficient vapor pressure in the oven, and consequently a high flux of atoms, we heat the oven to 450°C The distribution of velocities in the $\hat{z}$ direction is based on a probability distribution function of the beam $f(v) \propto v_z^3\, exp\left(-\frac{mv_z^2}{2kT}\right)$ which, at this temperature, has a width of $\sigma_{v_z} = \sqrt{kT/m} \approx 925m/s$. For the case of $|\beta| > 0$, the measurement is sensitive to the velocities as follows: $v_\beta = cos(\beta)v_z + sin(\beta)v_\perp$, where $v_\perp$ is the velocity in the x-y plane. In the experiments we work with $80° > \beta > 67°$, and since the expected distribution of $v_\perp$ in the beam is much narrower than that of v_z (even in this range of β) it can be approximated as a delta function and, therefore, we neglect it's contribution to v_β. In addition, the natural linewidth Γ is also much narrower than the width of the velocity distribution when taken to the frequency domain $\tilde{\sigma}_v = cos(\beta)\sigma_{v_z}/\lambda$ and therefore the Lorentzian lineshape in the optical density can also be approximated by a delta function, such that the resulted convolution gives simply the atomic density function. By making these approximations and working with weak intensity such that $I \ll I_{sat}$ we obtain the following expression for the optical density per unit velocity (for a given laser frequency):

$$OD(v) = n(v_\beta)\sigma_0 L \tag{7.4}$$

We measure the power P of the beam after its passage through the octagon twice. Once with the mechanical shutter which blocks the atomic beam open, so the atoms are present in the octagon. And once with the shutter closed, so the atoms are blocked, making $OD = 0$. With these two measurements we can extract the optical density as following:

$$OD = log\left(P_{closed}/P_{open}\right), \tag{7.5}$$

Where ”open”/”closed” refer to the shutter configuration.

In order to calibrate our measurement we split the beam and pass one of them

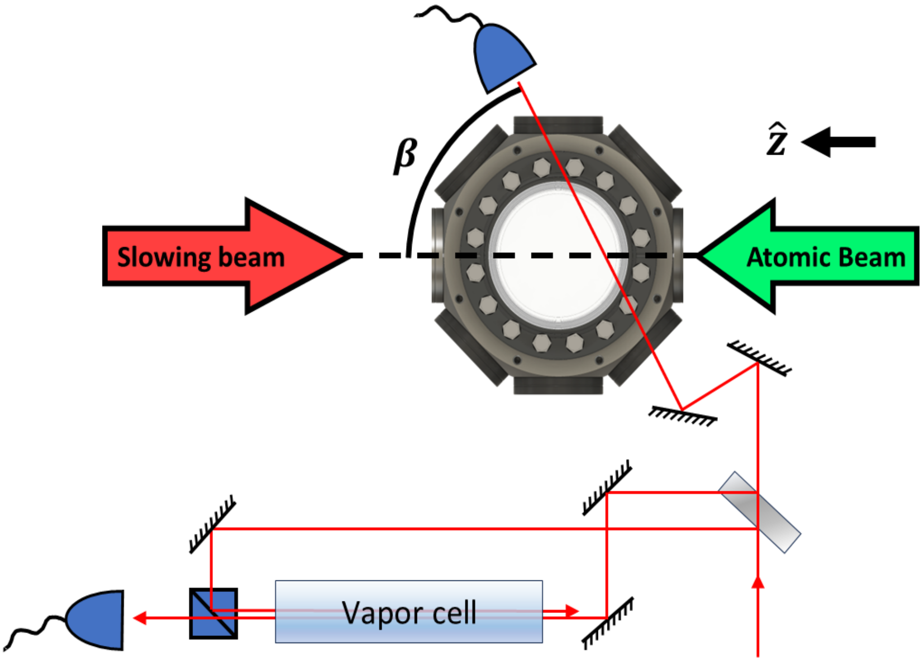

Figure 7.1: The measurement apparatus. Most of the laser power is directed for the probe beam through the octagon. Less than 1% of the light goes to the vapor cell for Doppler free spectroscopy for calibration.

through a vapor cell using Doppler-free saturation absorption spectroscopy, as shown schematically in Fig. 7.1. For each measurement, we capture the vapor cell signal in addition to the probe passing through the octagon. An example of such a measurement is shown in 7.2. The location of both D2 transitions ($|F = 1\rangle \rightarrow |F' = 0, 1, 2\rangle$ and $|F = 2\rangle \rightarrow |F' = 1, 2, 3\rangle$ which will be denoted from now on as $\nu_{1F'}$ and $\nu_{2F'}$) is recorded, and the horizontal axis of the measurement is calibrated to the known frequency difference of $\Delta\nu_{12} = 803.5$ MHz. In the case of $\beta > 0$ the atoms see the laser frequency red shifted setting the threshold to $\nu_{2F'}$ transition. All relevant signals are expected to appear at $\nu > \nu_{2F'}$. The opposite occurs for $\beta < 0$ when the threshold is set to $\nu_{1F'}$ and the signals appear at $\nu < \nu_{1F'}$. Notice that if β is sufficiently small, the contribution of atoms populating the $|F = 1\rangle$ and $|F = 2\rangle$ states can overlap and therefore interfere with our ability to observe low-velocity populations. For that reason, we must place the probe beam in the direction relevant for the state in which the atoms are in. Figure 7.3 shows the optical transitions caused by the slowing beam from the ground state $|F = 2, m_F = -2\rangle$ to the excited state for σ^+, σ^- and π polarizations of the laser along the propagation axis of atoms. The transitions are plotted in the form of velocity group that is in resonance with that specific transition for each laser (pump and repump). Each light polarization takes the atom into a different state according to the excited state m_J. The implication is that σ^+ and π transitions push the atoms into a dark state, while σ^- keeps the atoms in the closed cycle. It can be seen that around $z = 50$ cm, the magnetic field overshoots and creates a depumping transition for atoms with velocities up to ~ 200 m/s. This takes place after the slowing process ended, so it does not have any negative implications; however this means that we expect to find the slow atoms in the $|F = 1\rangle$ state in contrast to what is expected from a conventional Zeeman slower. This is caused primarily by the entrance of parasitic polarizations.

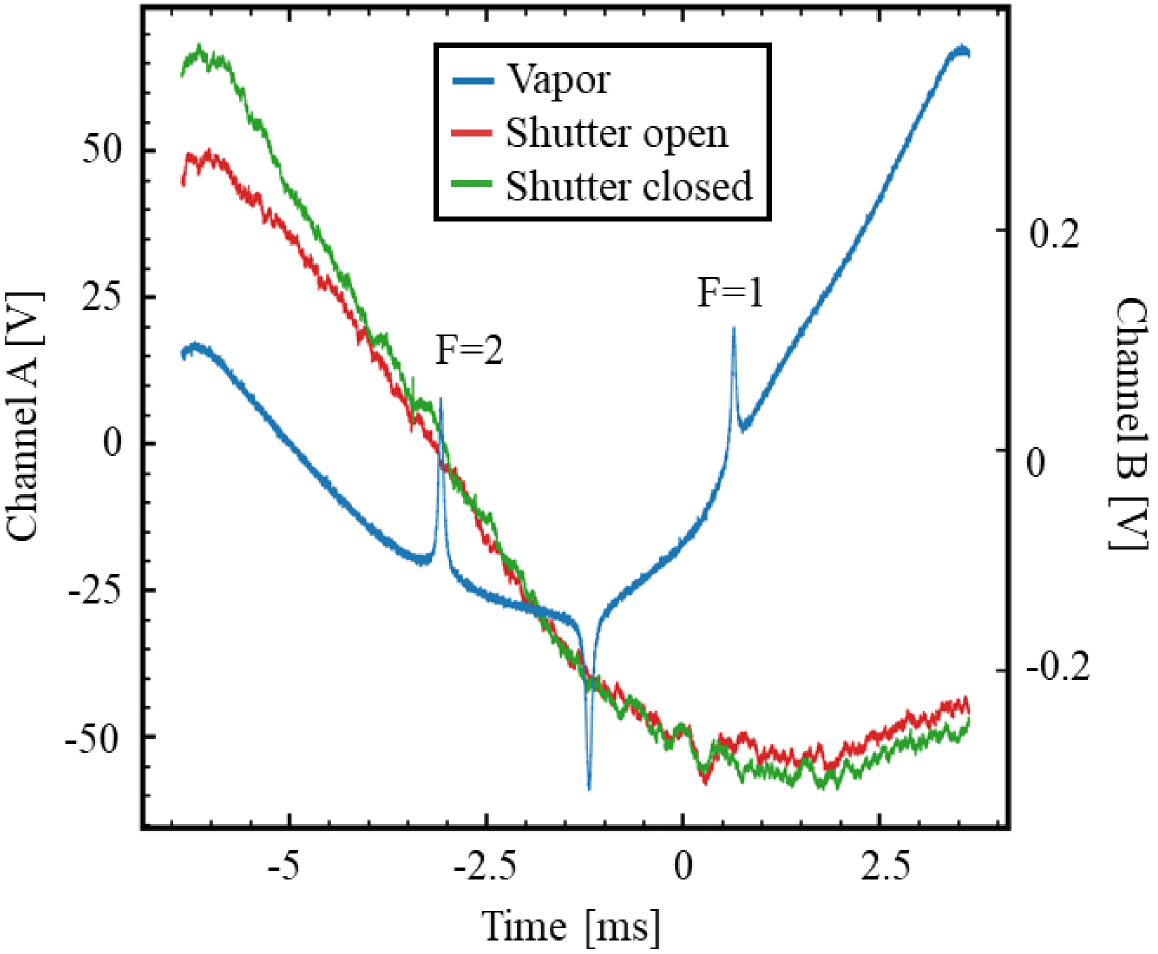

Figure 7.2: An example of a measurement. The blue line is the power of the vapor cell beam. The 2 sharp maxima are the frequency of F=1 and F=2 transition (see markings). Red and green lines are the probe beam power for closed and open shutters respectively. All data is shown as a voltage on the photodetector as a function of time, so all numbers here do not have any physical meaning prior to calibration.

7.3 Measurement Results

We present the results of a measurement for a probe beam that passes through the atoms at $\beta = -67.5°$. We choose negative β because we expect the atoms to be at the $|F = 1\rangle$ state, therefore, we want the signal to start at F=1 and go to lower frequencies (toward the $|F=2\rangle$ transition). The beam is gaussian with a waist $w = 2$ mm, and total power $P_{probe} = 5\mu W$. This means peak intensity $I_{peak} = 2 * P_{probe}/(\pi w^2) \approx 0.03 I_{sat}$. We pass the beam five times through the octagon in order to increase the path it takes through the atoms L, thus increasing the optical density according to Eq. 7.4. The slowing beam laser is prepared in a different optical table, and is transferred to the main table using an optical fiber. The light entering the fiber is composed of two frequencies, a pump laser detuned $\delta_p = -244$ MHz from the $\nu_{2F'}$ transition, and a repump laser detuned $\delta_r = -244$ MHz from the $\nu_{1F'}$ transition. These frequencies are compared to a locked master laser with a Fabry-Perot interferometer (ThorLabs SA30-73). The 2 lasers are combined on a PBS and then mixed in order to have them both with the same polarization. The power of each frequency is set by $\lambda/2$ wave plates. Figure 7.4 shows the optical density for different configurations of the pump/repump power. Without any laser, there are 2 ”Beam-Maxwell-Boltzmann” distributions, one for the $|F=2\rangle$ state and another for the $|F=1\rangle$ state. They go one on top of the other, so it is not so clear to see. When there is only a pump laser, the atoms slow down until the magnetic field zero crossing, and then they are all depumped into the dark state ($|F=1\rangle$), and so they accumulate at a velocity of $\sim 160 m/s$ as predicted for that specific detuning. When adding power to the repump, it is possible to see that they continue to slow down further and reach velocities as low as $100 m/s$. This proves that the atoms pass the zero crossing and manage to continue slowing beyond it.

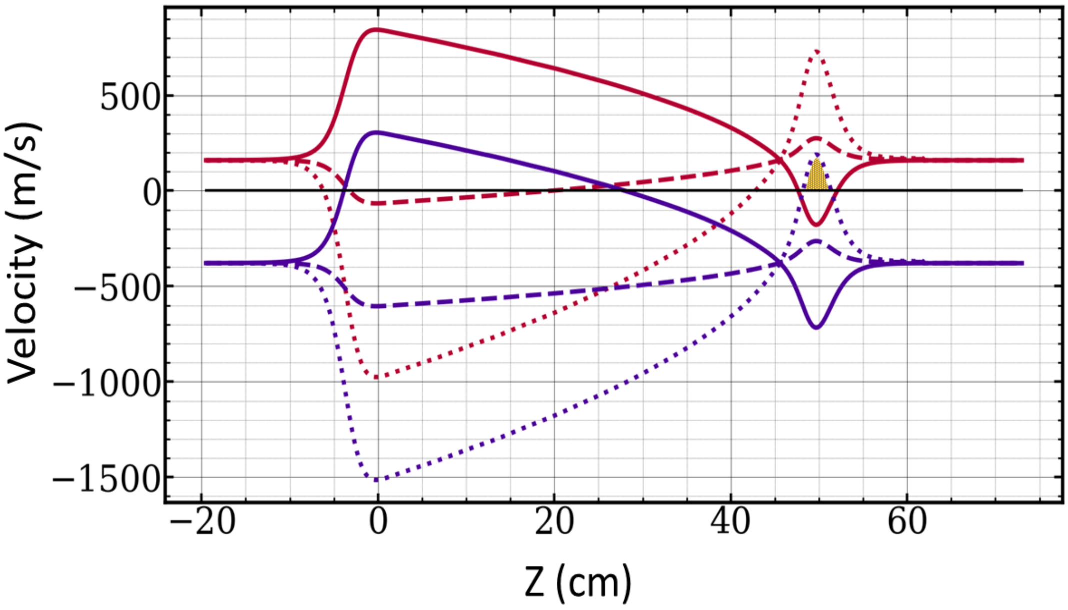

Figure 7.3: Transition of the slowing laser beam. The lines show the velocity in resonance with the laser for both pump and repump and every polarization. The positive velocity is considered to be going against the laser (in the positive z direction). Red lines are for the pump laser, and purple lines are for the repump. Solid lines are σ^-, dashed lines π, dotted lines σ^+. The yellow dotted area marks the place where depumping occurs for slow atoms after the end of the Zeeman slower because of the repump σ^+ transition.

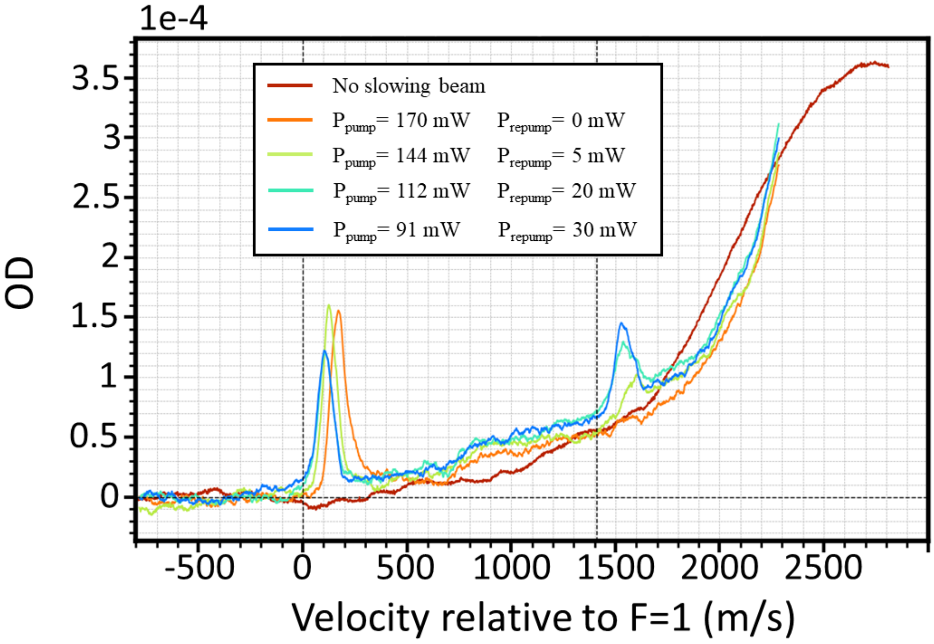

Figure 7.4: Optical density for $\beta = -67.5°$. The OD is ploted as a function of velocity starting from the F=1 transition. Note that for atoms in the F=2 state, the value on the horizontal axis does not reflect their velocity since there is a shift of $\Delta_{12}\lambda$.

Chapter 8

Magneto-optical trap (MOT)

8.1 Exact Field of a Circular Current Loop

As depicted in Fig. 8.1, the magnetic field components for a circular current loop with a current I and radius R, displaced by a distance D from the origin, are given by [48]:

$$B_z = \frac{\mu I}{2\pi} \frac{1}{\sqrt{(R+\rho)^2 + (z-D)^2}} \left[K(k^2) + \frac{R^2 - \rho^2 - (z-D)^2}{(R-\rho)^2 + (z-D)^2} E(k^2) \right], \tag{8.1}$$

$$B_\rho = \frac{\mu I}{2\pi} \frac{z-D}{\rho\sqrt{(R+\rho)^2 + (z-D)^2}} \left[-K(k^2) + \frac{R^2 + \rho^2 - (z-D)^2}{(R-\rho)^2 + (z-D)^2} E(k^2) \right], \tag{8.2}$$

where

$$k^2 = \frac{4R\rho}{(R+\rho)^2 + (z-D)^2}. \tag{8.3}$$

Here, $K(k^2)$ and $E(k^2)$ represent the complete elliptic integrals of the first and second kind, respectively.

8.2 Anti-Helmholtz Coil Configuration

An optical trap is formed by adding a quadrupole magnetic field that is zero at the center of the intersection and varies linearly with the distance from the center. The field can be produced by an anti-Helmholtz coil consisting of two coils with opposite currents.

The core equations for computing the magnetic field are initially applicable to a singular loop. For each loop, one must specify its dimensions, spatial location, and orientation. The magnetic field is then calculated at any given point in the space, represented by the coordinates (x, y, z). To determine the magnetic field generated

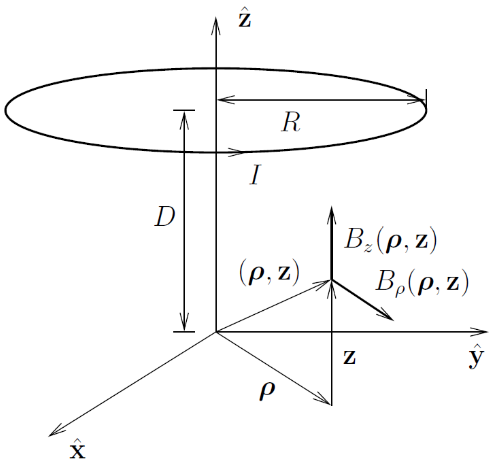

Figure 8.1: Cylindrical coordinates for the magnetic field of a single circular current loop centered at axial position z. (From [48]).

by a thick circular coil, the coil is discretized into a series of individual loops. In the context of a quadrupole trap, this involves dividing the coil into discrete $N_v \times N_r$ loops.

Each loop in this arrangement is characterized by a radius R_n and is located at r_n. Here, r_n denotes the center of the loop, which in our specific design is located at $(0, 0, z_n)$. The magnetic-field contribution from each loop is calculated and then cumulatively summed. This summation accounts for the magnetic field contributions from all individual loops, culminating in the comprehensive magnetic field profile of the entire quadrupole trap.

8.3 MOT Design

In the final iteration of our magneto-optical trap (MOT) design, we adopted a specific set of parameters that proved to be the most effective in achieving key operational objectives. The primary goal was to minimize the inductance of the system, a crucial factor in reducing switching times. Rapid switching is essential in this context, as it helps prevent atom loss during trap operations.

In addition, reducing the resistance of the coil was a significant consideration. Lower resistance mitigates the heating of the wires, thereby enhancing the efficiency of the cooling process. This aspect is vital to maintain the stability and longevity of the MOT.

Furthermore, in the interest of power efficiency and thermal management, we opted for a configuration that allows the use of lower currents. This approach not only conserves power but also minimizes the increase in temperature of the coil relative to

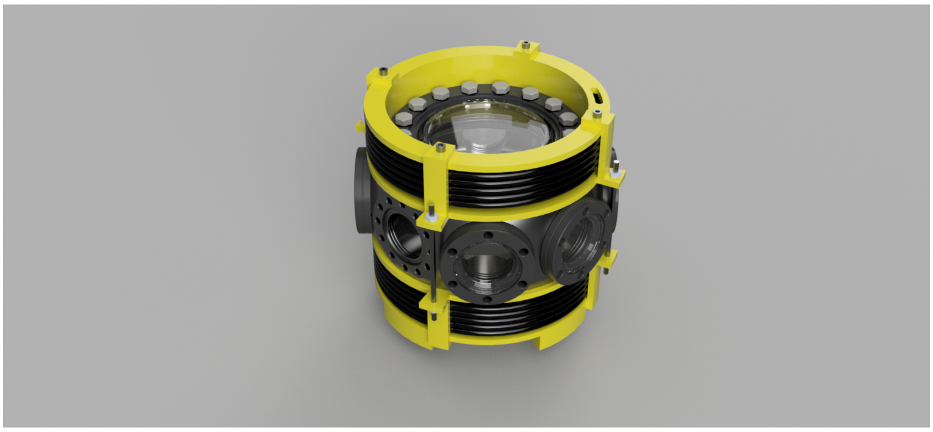

Figure 8.2: Magneto optical trap.

the surrounding air. This thermal control is paramount to ensure the effectiveness and safety of the MOT system. Importantly, the selection of these parameters was also constrained within the limits set by the trap's octagonal geometry. In our magneto-optical trap design, we utilized copper wire with inner and outer diameters of 0.24 cm and 0.478 cm, respectively, coated with a 0.04 cm insulating layer. The configuration consists of five vertical loops ($N_V = 5$) and two radial ($N_R = 2$) loops, operating at 180 A. Key design choices, including an inner radius (R_{in}) of 8.12 cm and the lowest layer distance (d_{lowest}) of 4.08 cm from the center of the vacuum chamber, were selected to optimize performance.

Using the specified design parameters, we calculate the resistance of the coil as $R = 0.0068\,\Omega$ (ohms), the power dissipation as approximately 221.1376 W (watts) and the inductance of the coil as $L = 0.0107\,\mathrm{H}$ (henries).

Our design is depicted in Fig. 8.2. Using the design parameters mentioned above, Figs. (8.3, 8.4) depicts the magnetic field (B_z) and its gradient as functions of the Z-axis.

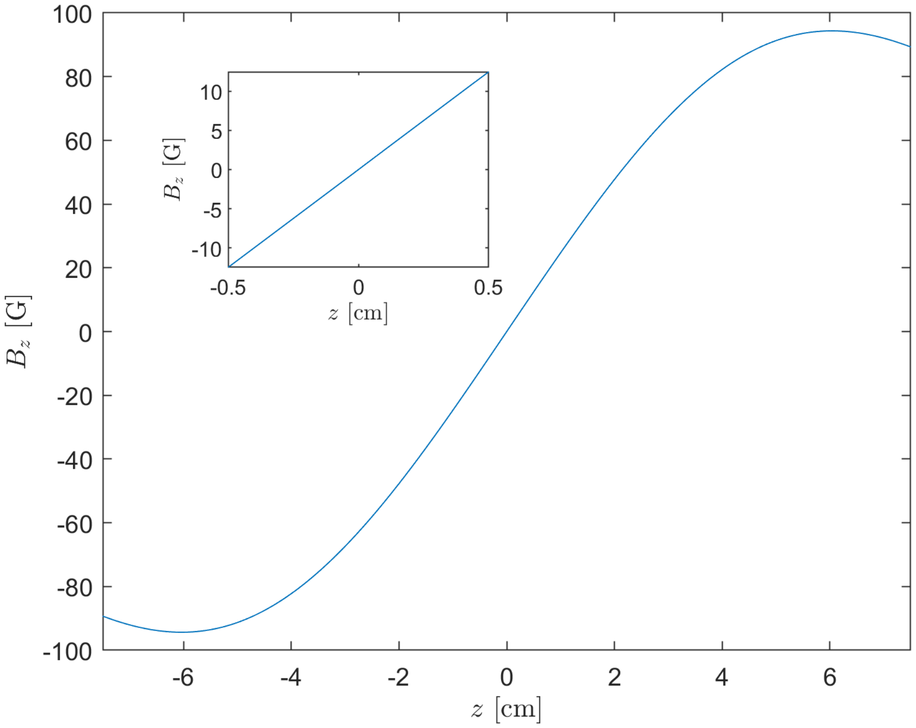

Figure 8.3: Variation of the magnetic field B_z across the Z-axis in the MOT.

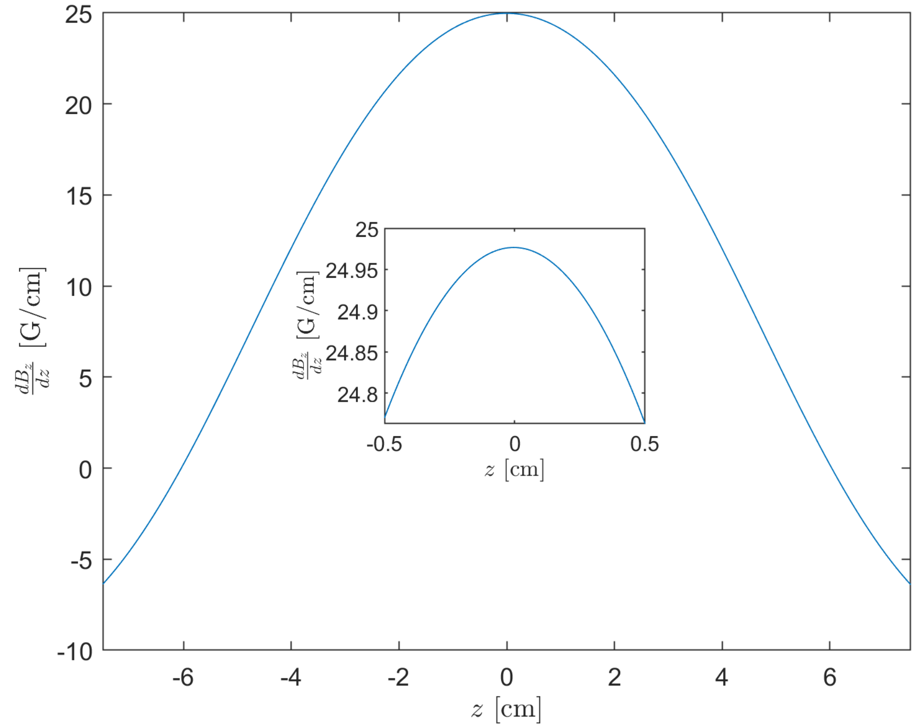

Figure 8.4: Gradient of the magnetic field along the Z-axis in the MOT.

Part II

Influence of Background Scattering on Efimov Scenario for Two Overlapping Feshbach Resonances

Chapter 9

Resonant Regimes in Few-Body Physics

9.1 Feshbach Resonances

Feshbach resonance is a powerful tool in quantum gas experiments, allowing tuning the strength and sign of interatomic interactions by adjusting the scattering length a through a simple change of an external magnetic field.

This resonance arises in a colliding two-atom system when the energy of the incoming open elastic channel is magnetically tuned into resonance with the bound molecular state of an energetically closed channel, as depicted in Fig. 9.1. The ability of tuning arises from the difference in the magnetic moments of the open and closed channels [49].

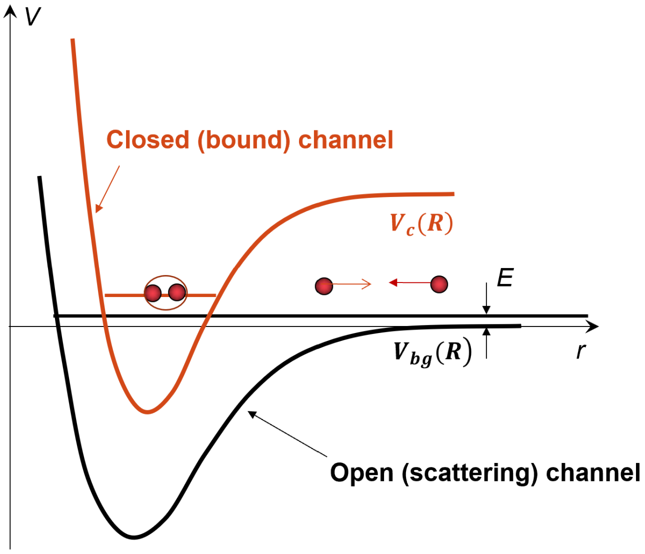

Figure 9.1: Basic two-channel model of a magnetically tunable Feshbach resonance. A resonance occurs when two free colliding atoms in an open channel potential with energy E resonantly couple to a bound state in the closed channel.

This resonant effect allows for large tunability of the scattering length from positive to negative infinity. In the case of an isolated resonance, the dependence of the scattering length a on the applied magnetic field strength B can be parameterized in the following relation:

$$a(B) = a_{\mathrm{bg}} \left(1 - \frac{\Delta}{B - B_0}\right), \tag{9.1}$$

where B_0 and Δ are the pole and the width of the resonance, respectively, and a_{bg} is the background scattering length of the open channel (see Fig. 9.2).

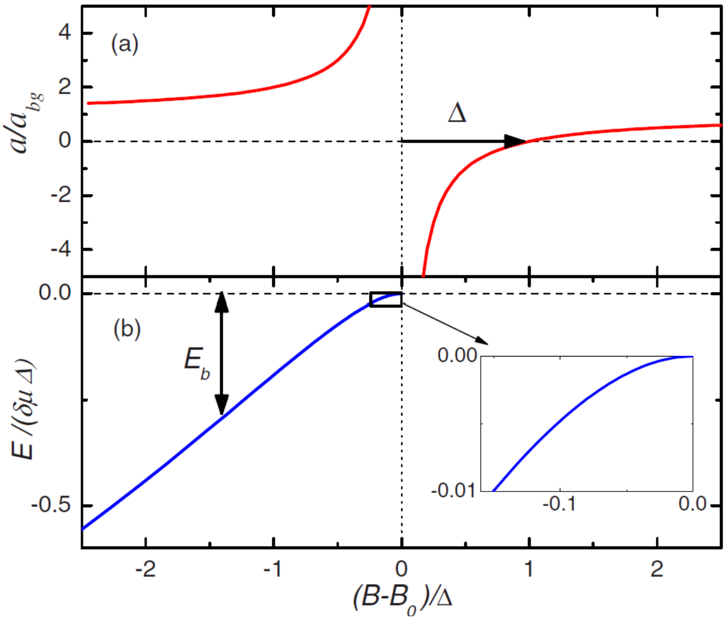

Figure 9.2: Feshbach resonance properties. (a) shows the scattering length's divergence and (b) the binding energy near a Feshbach resonance. The inset captures the universal regime with a notably large, positive scattering length and the quadratic behavior of the bound state near the resonance. (From [49]).

In the vicinity of the resonance position at B_0, where the two channels are strongly coupled, the scattering length is very large. For large positive values of a, a "dressed" molecular state exists with a binding energy given by:

$$E_b = -\frac{\hbar^2}{2\mu a^2}, \tag{9.2}$$

where μ is the reduced mass of the atom pair. In this limit E_b depends quadratically on the magnetic detuning $B - B_0$ and results in the bend shown in the inset of Fig. 9.2 (b) In this "universal" range, the physics is fully described by a as a single parameter. Away from resonance, the energy varies linearly with B with a slope given by $\delta\mu$, the difference in magnetic moments of the open and closed channels.

It is instrumental to distinguish between two types of Feshbach resonances. These are differentiated by the dimensionless resonance strength parameter s_{res}, which is defined as [49]:

$$s_{\mathrm{res}} = \frac{a_{\mathrm{bg}}\tilde{a}}{\hbar^2}(\delta\mu\Delta), \tag{9.3}$$

where $\tilde{a} = 0.956 R_{\mathrm{vdW}}$ is the mean scattering length of the van der Waals interaction [50], and $\delta\mu$ represents the difference in magnetic moment between the closed and open channels.

A broad resonance ($s_{\mathrm{res}} \gg 1$) emerges from a strong coupling to the bound state, with the scattering amplitude mainly influenced by a. In contrast, a narrow resonance ($s_{\mathrm{res}} \ll 1$) is the result of weak coupling, and the scattering amplitude is characterized by a large effective range in its vicinity.

When multiple bound states are present in one or more closed channels, it is possible to have overlapping Feshbach resonances. In this case, Eq. 9.1 can be generalized as following:

$$a = a_{\mathrm{bg}} \prod_i (1 - \Delta_i/|B - B_i|), \tag{9.4}$$

where Δ_i and B_i are the resonance position and width for each Feshbach resonance.

9.2 Efimov Resonances

In 1970, Vitaly Efimov showed that, for a system of identical bosons with divergent s-wave scattering length, an infinite series of three-body bound states exists [17].

In Figure 9.3, the Efimov scenario is illustrated by a series of trimer states that exhibit a geometric series. This set of states is plotted against the inverse scattering length, $1/a$, where the zero energy level aligns with the three-atom continuum. Below this energy threshold ($E < 0$), one can identify two different regions. For positive scattering lengths ($a > 0$), there exists a dimer-atom continuum. On the other hand, the negative scattering length realm ($a < 0$) is referred to as the Borromean region, distinguished by the formation of trimer states even though the constituent two-body subsystems remain unbound. The intersections with the three-atom continuum are denoted by the scattering lengths $a_-^{(n)}$, while the points where trimers descend into the dimer-atom continuum are marked by $a_*^{(n)}$, with $n \geq 0$ representing an integer sequence. The most tightly bound Efimov state is identified as the ground state, designated by $n = 0$.

The Efimov spectrum exhibits a universal geometrical scaling law in various properties, such as binding energy and trimer size. The length scales tend to scale as a single scaling constant $e^{\pi/s_0} = 22.7$, with $s_0 = 1.00624$, while the binding energy scales as $1/22.7^2$, as one probes Efimov resonances associated with higher energy levels.

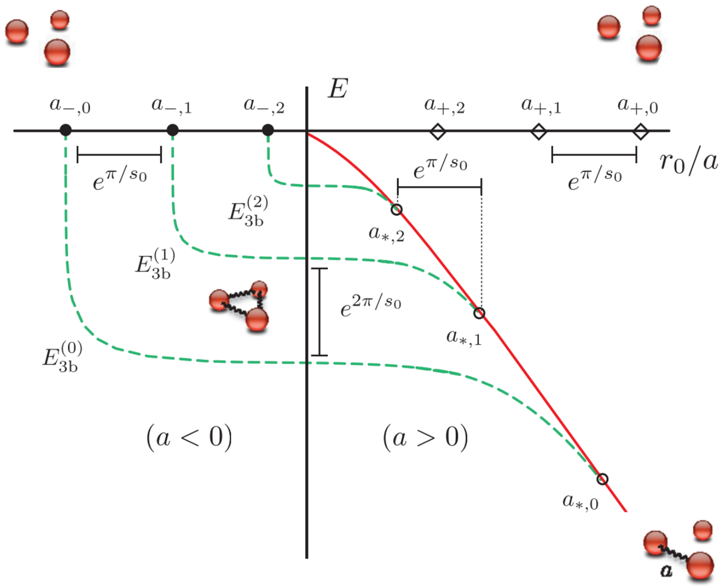

Figure 9.3: Illustration of the Efimov energy spectrum (green dashed lines) and the corresponding three-body parameters, a_+, a_-, and a^*. For $a < 0$, Efimov states are bound below the three-body continuum ($E = 0$), while for $a > 0$, they are bound below the atom-molecule threshold (solid red line). The Efimov trimer states exhibit a universal scaling separated by factors of $\exp(\frac{\pi}{s_0})$, and their binding energies scale with the factor $\exp(\frac{2\pi}{s_0})$. (From [51]).

9.3 Two-Channel Model

The physics of the Feshbach and Efimov resonances in the two- and three-body sectors, respectively, can be described within the framework of the minimalistic two-channel model [21]. In this model, we neglect the van der Waals (vdW) interaction and consider a simplified scenario involving a spherical potential with a cutoff radius k_c^{-1} to avoid divergence. All system parameters are normalized according to this cutoff, making them dimensionless, denoted by a tilde, except for the magnetic moment μ, which is renormalized to units of 1/G.

This section will summarize the two-channel model as reviewed in [39], which will be instrumental in understanding the following chapters.

9.3.1 Hamiltonian

The Hamiltonian of the system consists of two parts, $\hat{H} = \hat{H}_0 + \hat{H}_{\text{int}}$, where

$$\hat{H}_0 = \int \frac{d^3k}{(2\pi)^3} \left[\frac{\hbar^2 k^2}{2m} \hat{a}^\dagger_{\vec{k}} \hat{a}_{\vec{k}} + \left(E_b + \frac{\hbar^2 k^2}{4m} \right) \hat{b}^\dagger_{\vec{k}} \hat{b}_{\vec{k}} \right] \tag{9.5}$$

describes an open and a closed channel, and

$$\hat{H}_{\text{int}} = \Lambda \int \frac{d^3k}{(2\pi)^3} \int \frac{d^3q}{(2\pi)^3} \left[\hat{b}^\dagger_{\vec{k}} \hat{a}_{\vec{q}+\frac{\vec{k}}{2}} \hat{a}_{-\vec{q}+\frac{\vec{k}}{2}} + \hat{a}^\dagger_{-\vec{q}+\frac{\vec{k}}{2}} \hat{a}^\dagger_{\vec{q}+\frac{\vec{k}}{2}} \hat{b}_{\vec{k}} \right] \tag{9.6}$$

represents the interaction between these channels, with the coupling constant Λ. In this framework, $\hat{a}_{\vec{k}}$ ($\hat{b}_{\vec{k}}$) annihilates an atom (a molecule) with momentum $\hbar\vec{k}$ and mass m ($2m$) in the open (closed) channel, and $\hat{a}^\dagger_{\vec{k}}$ ($\hat{b}^\dagger_{\vec{k}}$) is its Hermitian conjugate. E_b is the bare molecular binding energy: $E_b = \mu(B_0 - B)$, where μ is the molecule's magnetic moment with respect to the open channel and B_0 is the bare resonance position.

9.3.2 Two-Body Sector

To describe the two-body sector we solve the Schrödinger equation $(\hat{H} - E)|\psi_{2B}\rangle = 0$ with the most general two-body ansatz in the center-of-mass superposition of two free atoms and one bare molecule:

$$|\psi_{2B}\rangle = \beta\hat{b}^\dagger_{k=0}|0\rangle + \int \frac{d^3k}{(2\pi)^3}\alpha_{\vec{k}}\hat{a}^\dagger_{\vec{k}}\hat{a}^\dagger_{-\vec{k}}|0\rangle. \tag{9.7}$$

After solving $(\hat{H} - E)|\psi_{2B}\rangle$ for $E > 0$, one extracts the renormalized scattering length $\tilde{a} = k_c a$

$$\tilde{a} = -\frac{1}{2\pi}\frac{\tilde{\Lambda}^2}{\tilde{\mu}(B_0 - B) - \frac{\tilde{\Lambda}^2}{\pi^2}} \tag{9.8}$$

Comparing Eq. (9.8) to the familiar form:

$$\tilde{a} = \frac{\tilde{\Delta}}{B - B_{\text{res}}}. \tag{9.9}$$

One obtains the observable parameters, $\tilde{\Delta}$ and B_{res}, in terms of the bare parameters Λ and B_0, given by:

$$B_{\text{res}} = B_0 - \frac{\tilde{\Lambda}^2}{\tilde{\mu}\pi^2}, \quad \tilde{\Delta} = \frac{\tilde{\Lambda}^2}{2\pi\tilde{\mu}}, \tag{9.10}$$

Neglecting the van der Waals (vdW) interactions ($r_{\text{vdW}} \to 0$), this model is particularly effective for narrow resonances, given that we satisfy the condition $R^* \gg r_{\text{vdW}}$. R^* is defined as:

$$R^* = \frac{\hbar^2}{m\mu\Delta}, \tag{9.11}$$

and we can express R^* in terms of the bare parameter Λ as:

$$\tilde{R}^* = \frac{2\pi}{\tilde{\Lambda}^2}. \tag{9.12}$$

The solution of $(\hat{H} - E)|\psi_{2B}\rangle$ for $E < 0$ results in the bound state solution, where the dimer binding energy is $E_D = -\hbar^2\lambda_D^2/m$. For the binding wave number λ_D, one finds:

$$\lambda_D = \frac{\sqrt{1 + 4\frac{R^*}{a}} - 1}{2R^*} \tag{9.13}$$

9.3.3 Three-Body Sector

To find the binding energy of the Efimov trimers we search for a negative energy solution $E = -\hbar^2\lambda_T^2/m$, where $\lambda_T > \max(0, \lambda_D)$, of the Schrödinger equation $(\hat{H} - E)|\psi_{3B}\rangle$ with

$$|\psi_{3B}\rangle = \int \frac{d^3k}{(2\pi)^3}\beta_{\vec{k}}\hat{b}^\dagger_{\vec{k}}\hat{a}^\dagger_{-\vec{k}}|0\rangle + \int \frac{d^3k}{(2\pi)^3}\int \frac{d^3q}{(2\pi)^3}\alpha_{\vec{k},\vec{q}}\hat{a}^\dagger_{\vec{q}+\frac{\vec{k}}{2}}\hat{a}^\dagger_{-\vec{q}+\frac{\vec{k}}{2}}\hat{a}^\dagger_{-\vec{k}}|0\rangle. \tag{9.14}$$

We work in the center-of-mass frame and have chosen $\vec{k}$ and $\vec{q}$ to be a set of Jacobi momenta. After renormalizing with respect to k_c, the expressions for $\tilde{a}$ and $\tilde{R}^*$, in Eqs. (9.9) and (9.12) respectively, are substituted and one obtains

$$\left[\sqrt{\frac{3k^2}{4} + \lambda_T^2} - \frac{1}{a} + \tilde{R}^*\left(\frac{3k^2}{4} + \lambda_T^2\right)\right]\psi(k) - \frac{2}{\pi}\int_0^\infty dq \ln\left(\frac{k^2 + kq + q^2 + \lambda_T^2}{k^2 - kq + q^2 + \lambda_T^2}\right)\psi(q) = 0, \tag{9.15}$$

where $\psi(k) = k\beta_k$ and all factors of k_c have cancelled. To solve Eq. (9.15) it is convenient to switch variables via

$$k = \frac{2}{\sqrt{3}}\lambda_T \sinh(\xi), \quad q = \frac{2}{\sqrt{3}}\lambda_T \sinh(\xi') \tag{9.16}$$

and rescale $\psi(k) \to \psi(k)/\cosh(\xi)$. If we limit ourselves to odd solutions for $\psi(k)$ the lower integration limit may be extended to $-\infty$ provided we divide the entire integral by 2. The first term is included in the integral by introducing $\int d\xi'\delta(\xi - \xi')$. One finds:

$$\int_{-\infty}^{\infty} d\xi' \mathcal{M}_{\lambda_T}(\xi, \xi')\psi(\xi') = 0 \tag{9.17}$$

with $\psi(\xi)$ an odd function of ξ and

$$\mathcal{M}_{\lambda_T}(\xi, \xi') = \delta(\xi - \xi')\left[1 - \frac{1}{a\lambda_T\cosh(\xi')} + R^*\lambda_T\cosh(\xi')\right] - \frac{4}{\sqrt{3}\pi}\ln\left(\frac{e^{2(\xi-\xi')} + e^{\xi-\xi'} + 1}{e^{2(\xi-\xi')} - e^{\xi-\xi'} + 1}\right). \tag{9.18}$$

A non-trivial solution is obtained when:

$$\det \mathcal{M}_{\lambda_T}(\xi, \xi') = 0, \tag{9.19}$$

which constitutes a closed equation for λ_T and can be solved numerically by discretizing ξ and ξ'. One searches for the value $\lambda_T = \lambda_T^{(\mathrm{sol})}$ for which $\det \mathcal{M}_{\lambda_T}(\xi, \xi')$ changes sign as λ_T is varied through $\lambda_T^{(\mathrm{sol})}$. Note that many solutions $\lambda_T^{(\mathrm{sol})}$ exist for a given a and R^*.

To verify the solution, the obtained value $\lambda_T^{(\mathrm{sol})}$ is inserted back into $\mathcal{M}_{\lambda_T=\lambda_T^{(\mathrm{sol})}}(\xi, \xi')$ and its eigenvalues and eigenfunctions $\psi(\xi)$ are calculated. One of the eigenvalues must be equal to zero (within machine precision), and its associated eigenfunction must be odd (odd number of nodes). The value of $\lambda_T^{(\mathrm{sol})}$ for which $\psi(\xi)$ has one node is the ground state. If $\psi(\xi)$ has three nodes, then it is the first excited state and so on.

Chapter 10

Three-Channel Model

Here we briefly summarize the main results of the three-channel model (3CM) developed in [39].

10.1 Phenomenology of Three-Channel Model

The three-channel model generalizes the standard two-channel approach by incorporating a second closed channel, enabling the treatment of overlapping Feshbach resonances. This added channel gives rise to two molecular bound states coupled to the atomic continuum.

In the three-body sector, as schematically illustrated in Fig. 10.1, three classes of continua emerge: the usual atom continuum plus two distinct atom-dimer continua associated with each closed channel. Efimov trimers exist around each resonance below the respective atom-dimer threshold. However, only trimers linked to the higher resonance are true bound states, while lower resonance trimers reside in the continuum of the upper dimer's atom-dimer states.

10.2 Hamiltonian

The Hamiltonian of the system consists of an open channel, the two closed channels, and the interaction term: $\hat{H} = \hat{H}_0 + \hat{H}_{int}$, where $\hat{H}_{int} = \hat{H}_1 + \hat{H}_2 + \hat{H}_{12}$. The first term $\hat{H}_0$ is the bare Hamiltonian of the three channels:

$$\hat{H}_0 = \int \frac{d^3k}{(2\pi)^3} \left[\frac{\hbar^2 k^2}{2m} \hat{a}^\dagger_{\vec{k}} \hat{a}_{\vec{k}} + \left(E_{b,1} + \frac{\hbar^2 k^2}{4m} \right) \hat{b}^\dagger_{\vec{k}} \hat{b}_{\vec{k}} + \left(E_{b,2} + \frac{\hbar^2 k^2}{4m} \right) \hat{c}^\dagger_{\vec{k}} \hat{c}_{\vec{k}} \right], \qquad (10.1)$$

where $\hat{a}_{\vec{k}}$ annihilates free particles of mass m, $\hat{b}_{\vec{k}}(\hat{c}_{\vec{k}})$ annihilates molecules in the first (second) channel, and $E_{b,1}(E_{b,2})$ is the bare energy of the first (second) molecular channel: $E_{b,i} = \mu_i (B_i - B)$. Without loss of generality, we assume $B_1 < B_2$. Both

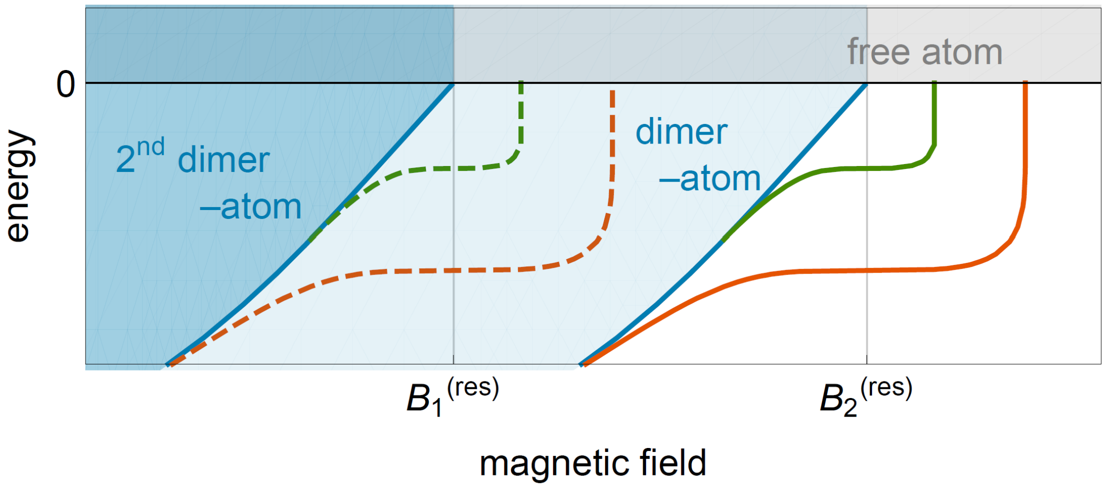

Figure 10.1: Depiction of the three-body sector involving overlapping Feshbach resonances at positions $B_1^{(\mathrm{res})}$ and $B_2^{(\mathrm{res})}$. The diagram illustrates the energy levels, showing the ground and excited Efimov trimers (in orange and green) and the two dimer states (in blue). The gray area represents the free-atom continuum, while the shaded blue regions indicate the dimer-atom continua above each dimer threshold. Notably, the Efimov trimers associated with the resonance at $B_1^{(\mathrm{res})}$ are embedded within the dimer-atom continuum of the higher resonance at $B_2^{(\mathrm{res})}$. (From [39]).

molecular channels are coupled to the open channel by means of:

$$\hat{H}_1 = \Lambda_1 \int \frac{d^3k}{(2\pi)^3} \int \frac{d^3q}{(2\pi)^3} \left[\hat{b}^\dagger_{\vec{k}} \hat{a}_{\vec{q}+\frac{\vec{k}}{2}} \hat{a}_{-\vec{q}+\frac{\vec{k}}{2}} + \hat{a}^\dagger_{-\vec{q}+\frac{\vec{k}}{2}} \hat{a}^\dagger_{\vec{q}+\frac{\vec{k}}{2}} \hat{b}_{\vec{k}} \right], \tag{10.2}$$

$$\hat{H}_2 = \Lambda_2 \int \frac{d^3k}{(2\pi)^3} \int \frac{d^3q}{(2\pi)^3} \left[\hat{c}^\dagger_{\vec{k}} \hat{a}_{\vec{q}+\frac{\vec{k}}{2}} \hat{a}_{-\vec{q}+\frac{\vec{k}}{2}} + \hat{a}^\dagger_{-\vec{q}+\frac{\vec{k}}{2}} \hat{a}^\dagger_{\vec{q}+\frac{\vec{k}}{2}} \hat{c}_{\vec{k}} \right]. \tag{10.3}$$

In addition, the two molecular channels are coupled to each other via:

$$\hat{H}_{12} = \Lambda_{12} \int \frac{d^3k}{(2\pi)^3} \left[\hat{c}^\dagger_{\vec{k}} \hat{b}_{\vec{k}} + \hat{b}^\dagger_{\vec{k}} \hat{c}_{\vec{k}} \right]. \tag{10.4}$$

10.3 Two-Body Sector

To describe the two-body sector we solve the Schrödinger equation $(\hat{H} - E)|\psi_{2B}\rangle = 0$ with the most general two-body ansatz in the center-of-mass frame:

$$|\psi_{2B}\rangle = \gamma \hat{c}^\dagger_{\vec{k}=0}|0\rangle + \beta \hat{b}^\dagger_{\vec{k}=0}|0\rangle + \int \frac{d^3k}{(2\pi)^3} \alpha_{\vec{k}} \hat{a}^\dagger_{\vec{k}} \hat{a}^\dagger_{-\vec{k}}|0\rangle. \tag{10.5}$$

Once plugged into the Schrödinger equation the following system of coupled equations is obtained:

$$\left(\frac{\hbar^2 k^2}{m} - E\right)\alpha_{\vec{k}} + \Lambda_1\beta + \Lambda_2\gamma = 0, \tag{10.6}$$

$$\left(E_{b,1} - E\right)\beta + 2\Lambda_1 \int \frac{d^3q}{(2\pi)^3}\alpha_{\vec{q}} + \Lambda_{12}\gamma = 0, \tag{10.7}$$

$$\left(E_{b,2} - E\right)\gamma + 2\Lambda_2 \int \frac{d^3q}{(2\pi)^3}\alpha_{\vec{q}} + \Lambda_{12}\beta = 0. \tag{10.8}$$

10.3.1 Scattering Length

The open channel coefficient $\alpha_{\vec{k}}$ can be extracted from Eq. (10.6) when positive energy is considered $E = \hbar^2 k_0^2/m > 0$. By comparing the expression for $\alpha_{\vec{k}}$ with the scattering Green's function, the scattering amplitude f_{k_0} can be obtained in terms of the molecular amplitudes β and γ:

$$f_{k_0} = -\frac{m}{4\pi\hbar^2}\left(\Lambda_1\beta + \Lambda_2\gamma\right). \tag{10.9}$$

Furthermore, the coupled Eqs. (10.6, 10.7, 10.8) can be numerically solved to obtain β and γ as functions of the bare parameters such as coupling strengths Λ_1, Λ_2 and bare molecular energies $E_{b,1}$, $E_{b,2}$. Thus, by combining these numerical solutions for β and γ with Eq. (10.9) the full scattering amplitude f_{k_0} can be determined solely in terms of the microscopic bare parameters of the model (see Eq. (6) in [39]).

10.3.2 Binding Energy

For the binding energy solution, the coupled Eqs. (10.6)-(10.8) are solved assuming $E = -\hbar^2\lambda_D^2/m < 0$ ($\lambda_D > 0$) (See Eq. (8) [39]) .

10.3.3 Relating the Bare Parameters to the Observable Parameters

Observable parameters such as resonance positions $B_i^{(res)}$ and widths Δ_i can be explicitly related to the bare parameters of the model, including coupling strengths Λ_i and bare molecular energies $E_{b,i}$. The analytical expression for the scattering length $a(B)$ can be derived in terms of the bare parameters at the zero energy limit ($f_{k_0=0} = -a$). Then it can be compared to a familiar parametrization form of the coupled-channels calculations of multiple Feshbach resonances [52]:

$$a(B) = \frac{\Delta_1}{B_1^{(res)} - B} + \frac{\Delta_2}{B_2^{(res)} - B}. \tag{10.10}$$

establishing the relation between the observable parameters of Eq. (10.10) and the underlying bare quantities of the model (see appendix in [39]). Since there are five bare parameters $(\Lambda_1, \Lambda_2, \Lambda_{12}, B_1, B_2)$ but only four observables $(\Delta_1, \Delta_2, B_1^{(res)}, B_2^{(res)})$, one bare parameter, such as the intermolecular coupling Λ_{12} remains unconstrained. As shown in [39]) it can be determined at will within a certain limit (for example set to zero) or constrained by another known quantity (such as bare resonance spacing). This choice, of course, influences the values of the other parameters.

10.4 Three-Body Sector: Efimov Trimers

Having determined the bare parameters in the two-body sector, we now calculate the Efimov energy levels in the three-body sector without additional adjustments.

The trimer binding energy $E_T = -\hbar^2 \lambda_T^2 / m$ is determined by solving the Schrödinger equation $(\hat{H} - E_T)|\psi_{3B}\rangle = 0$, provided the condition $\lambda_T > \max\{0, \lambda_D\}$ is satisfied. The latter signifies that only trimers associated with the higher magnetic field resonance are properly determined by the solution. The trimers of the lower resonances are embedded into the atom-dimer continuum of the higher resonance. Substitution of $|\psi_{3B}\rangle$:

$$|\psi_{3B}\rangle = \int \frac{d^3k}{(2\pi)^3} \gamma_{\vec{k}} \hat{c}^\dagger_{\vec{k}} \hat{a}^\dagger_{-\vec{k}} |0\rangle + \int \frac{d^3k}{(2\pi)^3} \beta_{\vec{k}} \hat{b}^\dagger_{\vec{k}} \hat{a}^\dagger_{-\vec{k}} |0\rangle + \int \frac{d^3k}{(2\pi)^3} \int \frac{d^3q}{(2\pi)^3} \alpha_{\vec{k},\vec{q}} \hat{a}^\dagger_{\vec{q}+\frac{\vec{k}}{2}} \hat{a}^\dagger_{-\vec{q}+\frac{\vec{k}}{2}} \hat{a}^\dagger_{-\vec{k}} |0\rangle \tag{10.11}$$

into the Schrödinger equation leads to three coupled equations:

$$\left(\frac{\hbar^2 q^2}{m} + \frac{3}{4} \frac{\hbar^2 k^2}{m} - E_T \right) \alpha_{\vec{k},\vec{q}} + \Lambda_1 \beta_{\vec{k}} + \Lambda_2 \gamma_{\vec{k}} = 0, \tag{10.12}$$

$$\left(\frac{3}{4} \frac{\hbar^2 k^2}{m} + E_{b,1} - E_T \right) \beta_{\vec{k}} + \Lambda_{12} \gamma_{\vec{k}} + 2\Lambda_1 \int \frac{d^3q}{(2\pi)^3} \left[\alpha_{\vec{k},\vec{q}} + 2\alpha_{\vec{q}-\frac{\vec{k}}{2}, -\frac{\vec{q}}{2}-\frac{3\vec{k}}{4}} \right] = 0, \tag{10.13}$$

$$\left(\frac{3}{4} \frac{\hbar^2 k^2}{m} + E_{b,2} - E_T \right) \gamma_{\vec{k}} + \Lambda_{12} \beta_{\vec{k}} + 2\Lambda_2 \int \frac{d^3q}{(2\pi)^3} \left[\alpha_{\vec{k},\vec{q}} + 2\alpha_{\vec{q}-\frac{\vec{k}}{2}, -\frac{\vec{q}}{2}-\frac{3\vec{k}}{4}} \right] = 0, \tag{10.14}$$

which are reduced to two by eliminating the free particle amplitude $\alpha_{\vec{k},\vec{q}}$. To solve the coupled equations, a high momentum cutoff k_c is introduced to regularize potential divergences. The quantities are renormalized to be dimensionless, denoted by a tilde, except for the magnetic moment μ, which is renormalized to units of 1/G.

Defining $\psi(k) = (\beta_k, \gamma_k)^T$, the procedure is similar to that of the two-channel model [22]. The amplitudes are rescaled as $\tilde{\beta}_k \to \frac{\tilde{\beta}_k}{\tilde{k}}, \tilde{\gamma}_k \to \frac{\tilde{\gamma}_k}{\tilde{k}}$. The variables are then changed to (ξ, ξ') using the variables switch in Eq. (11.24) and rescaled again using $\tilde{\beta}_\xi \to \frac{\tilde{\beta}_\xi}{\cosh \xi}$, $\tilde{\gamma}_\xi \to \frac{\tilde{\gamma}_\xi}{\cosh \xi}$. After these steps, the Schrödinger equation takes the form:

$$\int_{-\infty}^{\infty} d\xi' \begin{pmatrix} \mathcal{M}_{11}\left(\xi, \xi'\right) & \mathcal{M}_{12}\left(\xi, \xi'\right) \\ \mathcal{M}_{21}\left(\xi, \xi'\right) & \mathcal{M}_{22}\left(\xi, \xi'\right) \end{pmatrix} \begin{pmatrix} \tilde{\beta}_\xi \\ \tilde{\gamma}_\xi \end{pmatrix} = 0. \tag{10.15}$$

The matrix elements $(\mathcal{M}_{\lambda_T})_{ij}$ are given by:

$$(\mathcal{M}_{\lambda_T})_{ij} = [\delta_{ij}(f_i(\xi') - h(\xi')) + h(\xi') - \tilde{\Lambda}_i\tilde{\Lambda}_j g(\xi')]\delta(\xi - \xi') - \tilde{\Lambda}_i\tilde{\Lambda}_j L(\xi, \xi'), \tag{10.16}$$

where we have defined:

$$f_i\left(\xi\right) = \tilde{\lambda}_T \cosh \xi + \frac{\tilde{\mu}_i}{\tilde{\lambda}_T \cosh \xi}\left(B_i - B\right), \tag{10.17}$$

$$g\left(\xi\right) = \frac{1}{\pi^2}\left(\frac{1}{\tilde{\lambda}_T \cosh \xi} - \frac{\pi}{2}\right), \tag{10.18}$$

$$h\left(\xi\right) = \frac{\tilde{\Lambda}_{12}}{\tilde{\lambda}_T \cosh \xi}, \tag{10.19}$$

$$L\left(\xi, \xi'\right) = \frac{2}{\sqrt{3}\pi^2} \ln\left(\frac{e^{2(\xi-\xi')} + e^{\xi-\xi'} + 1}{e^{2(\xi-\xi')} - e^{\xi-\xi'} + 1}\right). \tag{10.20}$$

Requiring the determinant to vanish, $\det \mathcal{M}_{\lambda_T}(\xi, \xi') = 0$, provides an implicit equation for the binding energies of the Efimov trimer. The mathematical solutions to this equation must be validated by analyzing the associated eigenfunctions. Only odd eigenfunctions with the correct nodal structure represent the physical solution. This procedure identifies the spectrum of the bound state [39].

Chapter 11

Two-Channel Model with background Scattering

In this chapter, we examine the two-channel model extended to include a non-zero background scattering (2CMbg). Our analysis is inspired by the approach described in [30].

11.1 Hamiltonian

The Hamiltonian of the 2CMbg can be written as the sum of two terms: $\hat{H}^{2\mathrm{bg}} = \hat{H}_0^{2\mathrm{bg}} + \hat{H}_{int}^{2\mathrm{bg}}$. The first term is the bare Hamiltonian of free interacting atoms and closed channel molecules:

$$\hat{H}_0^{2\mathrm{bg}} = \int \frac{d^3k}{(2\pi)^3} \left[\frac{\hbar^2 k^2}{2m} \hat{a}^\dagger_{\vec{k}} \hat{a}_{\vec{k}} + \left(E_\mathrm{b} + \frac{\hbar^2 k^2}{4m} \right) \hat{b}^\dagger_{\vec{k}} \hat{b}_{\vec{k}} \right] + \\ \Lambda_{bg} \int \frac{d^3k}{(2\pi)^3} \int \frac{d^3q}{(2\pi)^3} \int \frac{d^3p}{(2\pi)^3} \chi^*_{\vec{q}}\, \chi_{\vec{p}}\, \hat{a}^\dagger_{\vec{p}+\frac{\vec{k}}{2}} \hat{a}^\dagger_{-\vec{p}+\frac{\vec{k}}{2}} \hat{a}_{\vec{q}+\frac{\vec{k}}{2}} \hat{a}_{-\vec{q}+\frac{\vec{k}}{2}}. \quad (11.1)$$

The background scattering between the atoms in the open channel is modeled by a separable potential: It is characterized by the coupling constant Λ_{bg} and a Gaussian function $\chi_{\vec{q}}$ with a cutoff length b [30]:

$$\chi_{\vec{q}} = \exp\left(-\frac{q^2 b^2}{2} \right). \quad (11.2)$$

The cutoff length b represents the potential range, and it is on the order of the van der Waals length (r_{vdW}). E_b is the bare molecular energy, which, as in the three-channel model (3CM), we assume to be a linear function in the external magnetic field: $E_b = \mu\,(B_0 - B)$. The second term, $\hat{H}_{int}^{2\mathrm{bg}}$, couples the two channels:

$$\hat{H}^{2\mathrm{bg}}_{int} = \Lambda \int \frac{d^3k}{(2\pi)^3} \int \frac{d^3q}{(2\pi)^3} \left(\chi^*_{\vec{q}}\, \hat{b}^\dagger_{\vec{k}} \hat{a}_{\vec{q}+\frac{\vec{k}}{2}} \hat{a}_{-\vec{q}+\frac{\vec{k}}{2}} + \chi_{\vec{q}}\, \hat{a}^\dagger_{-\vec{q}+\frac{\vec{k}}{2}} \hat{a}^\dagger_{\vec{q}+\frac{\vec{k}}{2}} \hat{b}_{\vec{k}} \right). \tag{11.3}$$

11.2 Two-Body Sector

In the two-body sector we substitute the following ansatz in the Schrödinger equation $(\hat{H}^{2\mathrm{bg}} - E)|\psi_{2B}\rangle = 0$.

$$|\psi_{2B}\rangle = \int \frac{d^3k}{(2\pi)^3} \alpha_{\vec{k}} \hat{a}^\dagger_{\vec{k}} \hat{a}_{\vec{k}} |0\rangle + \beta \hat{b}^\dagger_{\vec{k}=0} |0\rangle. \tag{11.4}$$

Solving the equation leads to a system of two coupled integral equations for amplitudes $\alpha_{\vec{k}}$ and β:

$$\left(\frac{\hbar^2 k^2}{m} - E \right) \alpha_{\vec{k}} + \Lambda \chi_{\vec{k}}\, \beta + 2\Lambda_{bg} \chi_{\vec{k}} \int \frac{d^3q}{(2\pi)^3} \chi^*_{\vec{q}} \alpha_{\vec{q}} = 0, \tag{11.5}$$

$$(E_b - E)\, \beta + 2\Lambda \int \frac{d^3q}{(2\pi)^3} \chi^*_{\vec{q}} \alpha_{\vec{q}} = 0, \tag{11.6}$$

where E_b is the bare molecular level.

11.2.1 Scattering Amplitude

To compute the scattering amplitude, we express $\alpha_{\vec{k}}$ from Eqs. (11.5) and (11.6) and compare it with the scattering Green's function for $E = \frac{\hbar^2 k_0^2}{m} > 0$:

$$\alpha_{\vec{k}} = (2\pi)^3\, \delta\left(\vec{k} - \vec{k}_0 \right) + \frac{\Lambda_{bg} \chi_k}{\Lambda} \frac{E - E_b + \frac{\Lambda^2}{\Lambda_{bg}}}{E - \frac{\hbar^2 k^2}{m} + i\eta} \beta. \tag{11.7}$$

Comparing Eq. (11.7) to the scattering theory allows determination of the scattering amplitude $f(E)$:

$$f(E) = -\frac{m}{4\pi\hbar^2} \frac{\Lambda_{bg} \chi_k}{\Lambda} (E - E_b + \frac{\Lambda^2}{\Lambda_{bg}}) \beta. \tag{11.8}$$

From Eq. (11.8), the amplitude β is expressed as a function of $f(E)$. Thus, we can substitute β along with $\alpha_{\vec{k}}$ from Eq. (11.7) into Eq. (11.6). This substitution leads to the following integral equation for $f(E)$:

$$\frac{m\, |\chi_{k_0}|^2}{4\pi\hbar^2 f(E)} = \int \frac{d^3k}{(2\pi)^3} \frac{|\chi_k|^2}{(E - \frac{\hbar^2 k^2}{m} + i\eta)} + \frac{\Lambda^2}{2\Lambda_{bg}^2 (E - E_b + \frac{\Lambda^2}{\Lambda_{bg}})} - \frac{1}{2\Lambda_{bg}}. \tag{11.9}$$

11.2.2 Relating the Bare Parameters to Observable Parameters

Here we link the observable parameters (a_{bg}, ΔB, $B^{(res)}$, E_D) to the model parameters (Λ_{bg}, Λ, b, B_0, μ).

In the limit of the vanishing coupling strength between channels ($\Lambda = 0$), the scattering amplitude reduces to the background scattering length: $f\left(E \to 0\right) = -a_{\text{bg}}$. Subsequently, using Eq. (11.9), one can derive a_{bg}, which is expressed as follows:

$$a_{bg} = \frac{b\sqrt{\pi}\Lambda_{bg}}{\Lambda_{bg} + \frac{2\pi^{3/2}\hbar^2}{m}b}, \tag{11.10}$$

Solving the integral equation for $f(E)$ as given in Eq. (11.9) for negative energies $E = \frac{\hbar^2 k_0^2}{m} < 0$ and expanding to positive energies through standard analytical continuation ($k_0 = iq$ with $q > 0$), and using Eq. (11.10), we obtain the following expression for the scattering amplitude:

$$\frac{1}{f(E)} = q\,\mathrm{erfc}(bq) - \frac{\exp\left(-b^2q^2\right)}{a_{bg}}\left(1 - \frac{\frac{2\pi\hbar^2\Lambda^2 a_{bg}}{m\Lambda_{bg}^2}}{E - E_b + \frac{\Lambda^2}{\Lambda_{bg}}}\right). \tag{11.11}$$

In the limit of zero energy the scattering amplitude which is given in Eq 11.11 converges to the scattering length $f\left(E\right) = -a$ which can be written as:

$$a = a_{bg}\left(1 - \frac{\frac{2\pi\hbar^2\Lambda^2 a_{bg}}{m\Lambda_{bg}^2}}{E_b - \frac{\Lambda^2}{\Lambda_{bg}} + \frac{2\pi\hbar^2\Lambda^2 a_{bg}}{m\Lambda_{bg}^2}}\right), \tag{11.12}$$

The scattering length expression (Eq. (11.12) is compared to the well-known parameterization equation (Eq. (1.1)), the desired relations between the observables and model parameters can be obtained:

$$\Delta B = -\frac{2\pi\hbar^2\Lambda^2 a_{bg}}{\mu m\Lambda_{bg}^2}, \tag{11.13}$$

$$B^{(res)} = B_0 - \frac{\Delta B}{1 - b\frac{\sqrt{\pi}}{a_{bg}}}. \tag{11.14}$$

11.2.3 Binding Energy

The binding energy (denoted $E_D = \frac{\hbar^2 q_D^2}{m} > 0$) is given by the poles of the scattering amplitude of Eq. (11.11) with negative energy ($E = -E_{dim} < 0$) leading to the following expression for q_D:

$$\frac{a_{bg}\exp(b^2q_D^2)q_D\mathrm{erfc}(bq_D)}{a_{bg}\exp(b^2q_D^2)q_D\mathrm{erfc}(bq_D)-1}+\frac{\hbar^2q_D^2}{m\mu\Delta B}=\frac{B-B^{(res)}}{\Delta B}. \tag{11.15}$$

E_D is obtained from the numerical solution of this equation.

Denoting the $R^\star$ parameter as a new length scale related to the resonance strength [16]:

$$R^\star=\frac{\hbar^2}{m|a_{\mathrm{bg}}\mu\Delta B|}, \tag{11.16}$$

Eq. (11.15) can be renormalized as following:

$$\frac{q_D^*\exp\left((q_D^*b^*)^2\right)\mathrm{erfc}\left(q_D^*b^*\right)}{q_D^*a_{bg}^*\exp\left((q_D^*b^*)^2\right)\mathrm{erfc}\left(q_D^*b^*\right)-1}+(-1)^jq_D^{*2}=\frac{1}{a_{bg}^*-a^*} \tag{11.17}$$

where $q_D^*=q_DR^*$, $b^*=b/R^*$, $a_{bg}^*=a_{bg}/R^*$, $a^*=a/R^*$ and $j=0$ if $\frac{\hbar^2}{ma_{bg}\mu\Delta B}<0$, or $j=1$ if $\frac{\hbar^2}{ma_{bg}\mu\Delta B}>0$. Note that these dimensionless quantities signify different types of Feshbach resonances. Specifically, $|a_{bg}^*|\geq 1$ corresponds to a broad resonance while $|a_{bg}^*|\ll 1$ signifies a narrow resonance. $|a_{bg}|\gg b$ denotes a shape resonance [30].

11.3 Three-Body Sector: Efimov Trimers

Having fixed the bare parameters in the two-body sector, we proceed to the three-body sector with no more adjustable parameters. To find the binding energy of the Efimov trimers, we look for a negative energy solution $E=-\frac{\hbar^2\lambda_T^2}{m}$ where $\lambda_T>\max\{0,\lambda_D\}$, of $(\hat{H}^{\mathrm{2bg}}-E)|\psi_{3B}\rangle=0$ with:

$$|\psi_{3B}\rangle=\int\frac{d^3k}{(2\pi)^3}\beta_{\vec{k}}\hat{b}_{\vec{k}}^\dagger\hat{a}_{-\vec{k}}^\dagger|0\rangle+\int\frac{d^3k}{(2\pi)^3}\int\frac{d^3q}{(2\pi)^3}\alpha_{\vec{k},\vec{q}}\hat{a}_{\vec{q}+\frac{\vec{k}}{2}}^\dagger\hat{a}_{-\vec{q}+\frac{\vec{k}}{2}}^\dagger\hat{a}_{-\vec{k}}^\dagger|0\rangle. \tag{11.18}$$

We work in the center of mass frame and have chosen $\vec{k}$ and $\vec{q}$ to be a set of Jacobi momenta. The Schrödinger equation leads to the coupled equations:

$$(E_b-E_{rel})\beta_{\vec{k}}+2\Lambda\frac{1}{(2\pi)^3}\int d^3q\chi_{\vec{q}}^*\left(\alpha_{\vec{k},\vec{q}}+2\alpha_{\vec{q}-\frac{\vec{k}}{2},-\frac{\vec{q}}{2}-\frac{3}{4}\vec{k}}\right)=0, \tag{11.19}$$

$$\mathit{\Lambda}\chi_{\vec{q}}\beta_{\vec{k}}+\alpha_{\vec{k},\vec{q}}\left(\frac{\hbar^2q^2}{m}-E_{rel}\right)+2\Lambda_{bg}\frac{1}{(2\pi)^3}\chi_{\vec{q}}\int d^3q\chi_{\vec{q}}^*\left(\alpha_{\vec{k},\vec{q}}+2\alpha_{\vec{q}-\frac{\vec{k}}{2},-\frac{\vec{q}}{2}-\frac{3}{4}\vec{k}}\right)=0, \tag{11.20}$$

where $E_{rel}=E-\frac{3}{4}\frac{\hbar^2k^2}{m}$ is the collisional (or relative) energy of an atomic pair of total momentum $\vec{k}$. To simplify Eqs. (11.19, 11.20), we introduce a dressed atom-molecule wave function $\beta_{\vec{k}}^{\mathrm{eff}}$ [30]:

$$\beta_{\vec{k}}^{\text{eff}} = \frac{\Lambda_{bg}\beta_{\vec{k}}}{\Lambda^2}[E_{rel} - E_b + \frac{\Lambda^2}{\Lambda_{bg}}]. \tag{11.21}$$

Substituting Eq. (11.21) into Eqs. (11.19, 11.20) leads to:

$$\left(\frac{\hbar^2 q^2}{m} - E_{rel}\right)\alpha_{\vec{k},\vec{q}} + \Lambda\chi_{\vec{q}}\beta_{\vec{k}}^{\text{eff}} = 0. \tag{11.22}$$

One eliminates $\alpha_{\vec{k},\vec{q}}$ from Eq. (11.22) and insert it in Eq. (11.19) to obtain a closed integral equation verified by the effective atom-molecule wave function:

$$\frac{\exp\left(-mE_{rel}b^2/\hbar^2\right)}{4\pi f\left(E_{rel}\right)}\beta_{\vec{k}}^{\text{eff}} = \frac{2}{(2\pi)^3}\int d^3q \frac{\beta_{\vec{q}}^{\text{eff}}\exp\left(-\left(\vec{q}+\frac{\vec{k}}{2}\right)^2\frac{b^2}{2}\right)\exp\left(-\left(\vec{k}+\frac{\vec{q}}{2}\right)^2\frac{b^2}{2}\right)}{\lambda_T^2 + q^2 + \vec{q}\cdot\vec{k} + k^2}. \tag{11.23}$$

To solve Eq. (11.23) we define $\psi(k) = k\beta_k^{\text{eff}}$ and change variables using:

$$\text{k}=\frac{2}{\sqrt{3}}\lambda_T\text{sinh}(\xi)\ ,\ \text{q}=\frac{2}{\sqrt{3}}\lambda_T\text{sinh}(\xi'). \tag{11.24}$$

Then we rescale $\psi(\xi) \rightarrow \frac{\psi(\xi)}{\cosh(\xi)}$ and look only to odd solutions $\psi(\xi)$. The lower integration limit may be extended to $-\infty$ provided we divide the entire integral by two:

$$\begin{gathered}
-\frac{2}{\pi\sqrt{3}}\int_{-\infty}^{\infty} d\xi'\psi(\xi')\exp\left(b^2\lambda_T^2\left(1+\frac{1}{2}\sinh^2(\xi)+\frac{1}{2}\sinh^2(\xi')\right)\right)\cdot \\
\left(E_1\left(b^2\lambda_T^2\left(t(-1)\right)\right) - E_1\left(b^2\lambda_T^2\left(t(1)\right)\right)\right) + \frac{\exp(b^2\lambda_T^2\cosh^2\xi)}{\lambda_T\cosh(\xi)}\psi(\xi)\cdot \\
\left(\lambda_T\cosh(\xi)\text{erfc}(b\lambda_T\cosh(\xi)) - \frac{\exp(-b^2\lambda_T^2\cosh^2\xi)}{a_{bg}}\left(1+\frac{\frac{2\pi\hbar^2\Lambda^2 a_{bg}}{m\mathit{\Lambda}_{bg}^2}}{\lambda_T^2\cosh^2\xi + E_b - \frac{\mathit{\Lambda}^2}{\mathit{\Lambda}_{bg}}}\right)\right) = 0,
\end{gathered} \tag{11.25}$$

where $E_1(z) = \int_1^\infty ds\frac{e^{-sz}}{s}$ is the exponential integral and

$$t(j) = 1 + \frac{4}{3}\sinh^2(\xi) + \frac{4}{3}\sinh^2(\xi') + j\frac{4}{3}\sinh(\xi)\sinh(\xi'). \tag{11.26}$$

In the limit of $b \rightarrow 0$, the kernel in the integral coincides with the integral of the STM equation [53]. By inserting $\int d\xi'\delta\left(\xi - \xi'\right)$ into the second term, this expression can be incorporated into the integral and one obtains:

$$\int_{-\infty}^{\infty} d\xi'\mathcal{M}_{\lambda_T}(\xi,\xi')\psi(\xi') = 0, \tag{11.27}$$

with $\psi(\xi)$ being an odd function. The matrix $\mathcal{M}_{\lambda_T}(\xi, \xi')$ can be expressed as:

$$M\left(\xi, \xi'\right) = \delta\left(\xi - \xi'\right) K\left(\xi'\right) - \delta\left(\xi - \xi'\right) H\left(\xi'\right) - 2\pi L\left(\xi, \xi'\right), \tag{11.28}$$

where

$$H(\xi) = \frac{1}{\lambda_T^* a_{bg}^* \cosh(\xi)} \left(1 - \frac{1}{\left(\lambda_T^* \cosh(\xi)\right)^2 (-1)^j a_{bg}^* + 1 + \frac{1}{\frac{a^*}{a_{bg}^*} - 1}}\right), \tag{11.29}$$

$$K\left(\xi'\right) = \exp\left(\left(b^* \lambda_T^* \cosh(\xi)\right)^2\right) \operatorname{erfc}\left(b^* \lambda_T^* \cosh(\xi)\right), \tag{11.30}$$

$$\begin{aligned} L\left(\xi, \xi'\right) = \frac{1}{\sqrt{3}\pi^2} \exp\left(\left(b^* \lambda_T^*\right)^2 \left(1 + \frac{1}{2}\sinh^2(\xi) + \frac{1}{2}\sinh^2(\xi')\right)\right) \cdot \\ \left(E_1\left(\left(b^* \lambda_T^*\right)^2 t(-1)\right) - E_1\left(\left(b^* \lambda_T^*\right)^2 t(1)\right)\right), \end{aligned} \tag{11.31}$$

where $\lambda_T^* = \lambda_T R^*$, $b^* = b/R^*$, $a_{bg}^* = a_{bg}/R^*$, $a^* = a/R^*$ and $j = 0$ if $\frac{\hbar^2}{m a_{bg} \mu \Delta B} < 0$, or $j = 1$ if $\frac{\hbar^2}{m a_{bg} \mu \Delta B} > 0$, and $t(i)$ is defined in Eq. (11.26). We then renormalized Eq. (11.25) with respect to R^*.

The requirement of a vanishing determinant, $\det M_{\lambda_T}(\xi, \xi') = 0$, provides an implicit equation for λ_T. This transcendental equation can be solved numerically by discretizing ξ and ξ' on a grid. One searches for solutions $\lambda_T = \lambda_T^{(sol)}$ where the determinant changes sign as λ_T passes through $\lambda_T^{(sol)}$. Note that for given $\frac{R^*}{a_{bg}}$ and $\frac{b}{R^*}$, there are typically many solutions $\lambda_T^{(sol)}$. To verify a particular solution is physical, the obtained $\lambda_T^{(sol)}$ is substituted back into $M_{\lambda_T}(\xi, \xi')$, and its eigenvalues and eigenfunctions $\psi(\xi)$ are computed. The solution corresponds to a bound state only if one eigenvalue is zero (within numerical precision) and the associated eigenfunction $\psi(\xi)$ is an odd function of ξ (has an odd number of nodes).

Chapter 12

Two-Channel Model with background Scattering Versus Three-Channel Model

In this chapter, we define two model systems featuring two overlapping Feshbach resonances, which we examine using the 2CMbg and 3CM. These models were discussed in previous chapters.

Note that in [39] the same model systems are approximated using the two-channel model without background scattering (2CM) and with 3CM. Significant deviations in both the two- and three-body sectors are reported.

12.1 Definition of Model Systems

We use the 3CM to define two model systems of overlapping s-wave Feshbach resonances. To facilitate comparison between the performance of 2CM and 2CMbg in model systems, the latter are chosen to be the same as in [39] where they are com-

Type	NB	BN
$\Delta_1/a_0(\mathrm{G})$	150	1000
$\Delta_2/a_0(\mathrm{G})$	1000	150
$B_1 - B_2^{(res)}(\mathrm{G})$	-39.39	-54.07
$B_2 - B_2^{(res)}(\mathrm{G})$	-17.22	-2.535
$\Lambda_1/(E_0 a_0^{\frac{3}{2}})$	0.454	0.513
$\Lambda_2/(E_0 a_0^{\frac{3}{2}})$	0.272	0.131
Λ_{12}/E_0	2.5×10^{-4}	2.5×10^{-4}

Table 12.1: Parameters of the two model systems: NB and BN [39].

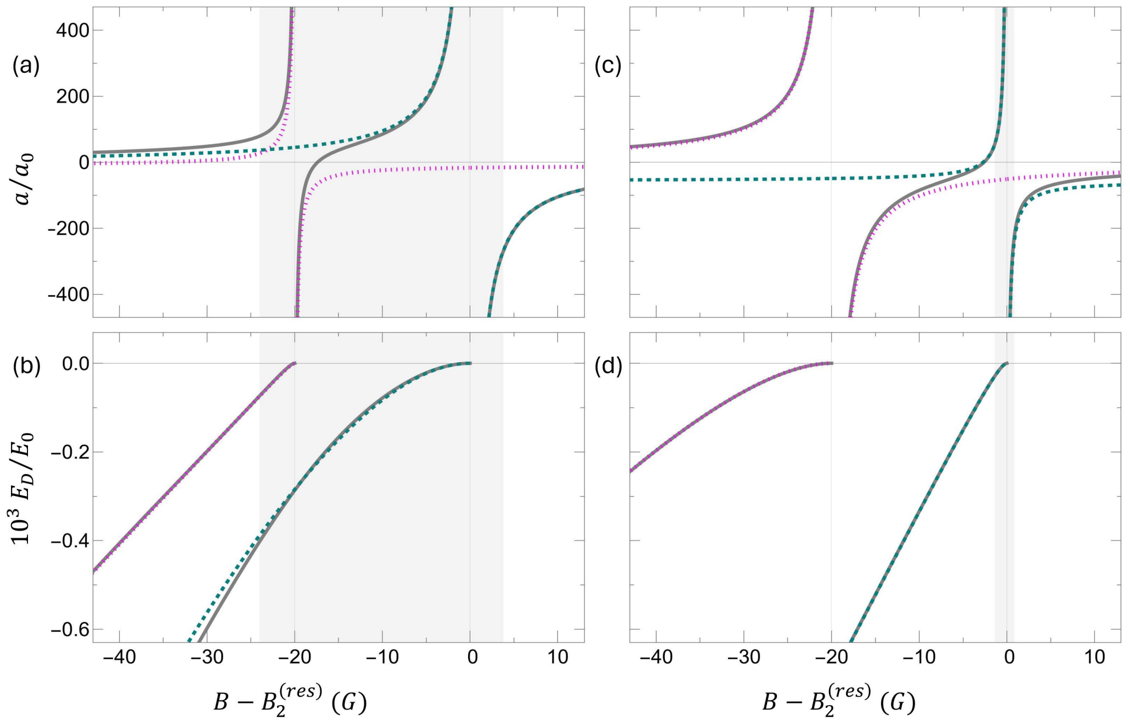

Figure 12.1: Two-body sectors of the NB (a,b) and BN (c,d) models. The scattering length (a,c) and dimer binding energy (b,d) of the three-channel model (solid lines) are compared with the two-channel model including a_{bg} (dashed lines). The gray vertical lines indicate the resonance positions $B_1^{(res)}$ and $B_2^{(res)}$. The shaded region shows the range of the Efimov ground state trimer $B_*^{(0)} < B < B_-^{(0)}$ associated with $B_2^{(res)}$.

pared to only 2CM. The model alkali-like atom is considered to have purely singlet molecular bound states and to be subject to a high enough magnetic field to ensure linear Zeeman shift of atomic energy levels to a good approximation. The value of the magnetic moments of both closed channels with respect to the open channel is thus $\mu_1 = \mu_2 = -2\mu_B$, where $\mu_B = 1.4$ MHz/G is the Bohr magneton. The first (second) system is characterized by $\Delta_1 \ll \Delta_2$ ($\Delta_2 \ll \Delta_1$) where Δ_1 and Δ_2 are the resonance widths (see Eq. (10.10)). For both systems, denoted as narrow-broad (NB) and broad-narrow (BN), respectively, the two Feshbach resonances are separated by a distance of $B_2^{(res)} - B_1^{(res)} = 20$G. As indicated in Table 12.1, for the NB (BN) system, the resonance at $B_1^{(res)}$ is narrow (broad) with $\Delta_1/a_0 = 150$G ($\Delta_1/a_0 = 1000$G) while the resonance at $B_2^{(res)}$ is broad (narrow) with $\Delta_2/a_0 = 1000$G ($\Delta_2/a_0 = 150$G). Efimov energy levels are explored only across the resonance at higher magnetic field for both scenarios. This is because they are true bound states, while the states across the other resonance are embedded into the atom-dimer continuum as shown in Fig. 10.1. By comparing the Efimov physics in the NB and BN scenarios, the influence of overlapping resonances can be revealed for both configurations.

12.2 Approximation of the Model Systems by the 2CMbg

Here we investigate how well the model systems can be approximated by the 2CMbg. As the latter describes only an isolated Feshbach resonance, each resonance in the 3CM is considered independently, and the resonance positions $B_1^{(res)}$ and $B_2^{(res)}$ are fixed to those defined by the 3CM.

In 2CMbg there are four bare parameters: b, Λ_{bg}, Λ and B_0. The scattering length (see Eq. (1.1)) is described by three observables: $a_{bg}, \Delta B, B_i^{(res)}$ and another observable is provided by the binding energy. Analytical expressions between the bare parameters and the scattering length observables can be achieved (see Eqs. (11.13) and (11.14)) by direct comparison between Eq. (11.12) and Eq. (1.1). There are different available strategies that can be followed to fix the bare parameters of the model. Here we choose to fit E_D of the 3CM with Eq. (11.15) and to extract the values of $a_{bg}, \Delta B, \mu$ and b and the remaining bare parameters are deduced from Eqs. (11.10, 11.13, 11.14). The resulting parameters are summarized in Table 12.2. Note that in this approach, we define all unknowns, including the magnetic moment μ and the potential range b, as fitting parameters. By allowing a maximum number of parameters to be adjusted, we might obtain an underdetermined system. However, we find that the fitting procedure converges and, as a self-consistency check, we calculate the parameter R^* that is related to the resonance strength (see Eq. (11.16)). For narrow resonances, we expect that $R^* \gg b$ and $R^* \gg |a_{bg}|$, and as shown in the last line of Table 12.2 both conditions are satisfied for all resonances, although at a different level of accuracy. The fitting procedure thus supports the fact that the underlining resonances are narrow.

Once all parameters are determined, we calculate the binding energies in the three-body sector and the results obtained from the 2CMbg are compared with those of the model systems.

Finally, we comment on other strategies to fix the bare parameters of the 2CMbg. One possibility is to fit the scattering length with Eq. (11.12) and to extract the remaining bare parameter (b) through the corresponding analytic expression. Another approach can follow the idea that the two- and three-body sectors are renormalizable with respect to the cutoff parameter (b) [39] leading to the elimination of the latter. However, to obtain consistent results in this case, $B_i^{(res)}$ must be released as a fitting parameter. Yet another strategy is to make a global fit of both the scattering length and the binding energy together and to extract all parameters of the model. Although different approaches lead to some variations of the results in the three-body sector, the main conclusions of this study remain invariant to the specifics of this choice. We emphasize that the main motivation here is to identify universal properties of the results which will be highlighted when presented.

Type	NB-Res1	NB-Res2	BN-Res1	BN-Res2
$\Delta B\,(\mathrm{G})$	-15.57	-204.7	-6135	-2.713
$a_{bg}\,(a_0)$	-9.393	-4.886	-0.165	-56.84
$b\,(a_0)$	136.8	0.504	2.871×10^{-4}	1.371
$\mu\,(\mathrm{MHz/G})$	-1.517	-4.514	-2.47	-2.8
$R^*(a_0)$	325.6	16	28.71	167.2

Table 12.2: 2CMbg parameters obtained from the fit to the 3CM binding energies for two model systems. The R^* parameter in the last line is defined according to Eq. (11.16).

12.3 Two-Body Sector

Fig. 12.1 (a,b) compares the scattering length and the binding energies of the 2CMbg with the NB model system. As the three-body sector is calculated across the resonance at a higher magnetic field only ($B_2^{(res)}$) we discuss it first. The fitting of the binding energy is shown in Fig. 12.1 (b) as a green dashed line and indicates a relatively poor reproduction of the model system. Note that the obtained absolute value of $|\mu| = 4.514$ MHz/G (see Table 12.2, "NB-Res2") is significantly higher than that of the model system ($|\mu| = 2.8$ MHz/G). Note also that the opposite situation occurs for the second resonance (see Table 12.2, "NB-Res1"). This behavior reflects the presence of strong mutual repulsion between the binding energy levels in the NB model system induced by coupling through a continuum [39]. Although deviations of the 2CMbg binding energy from the model system vary as a function of the magnetic field fitting range, the main failure can be observed when the scattering length dependencies on the magnetic field are compared (see Fig. 12.1 (a)). It is clear that the 2CMbg has no chance to reproduce a sharp turn toward the scattering length zero crossing failing to fulfill the main motivation behind this model (see green dashed line versus gray solid line in Fig. 12.1 (a)). We emphasize that this conclusion is independent of the applied strategy to fix bare parameters and that we expect the three-body sector of the 2CMbg to miss the NB model system behavior.

In contrast to the previous case, the binding energy of the lower magnetic field resonance ($B = B_1^{(res)}$) is reproduced quite well by the 2CMbg (see the magenta dotted line in Fig. 12.1 (b)). However, the scattering length behavior still fails to reproduce the position of the zero crossing and shows significant deviations from the model system (see the magenta dotted line versus the gray solid line in Fig. 12.1 (a)). The reason of this distortion can be attributed to the above-mentioned strong energy level repulsion. Note, though, that this result is not universal. If a different strategy is chosen and the scattering length is fitted instead of the binding energy, the zero crossing will be captured by the 2CMbg. This is, however, irrelevant for the results in the three-body sector which are calculated for the higher magnetic field resonance only.

Fig. 12.1 (c,d) compares the scattering length and the binding energies of 2CMbg to the BN model system. Here, the success of the 2CMbg is obvious in both the binding energies (Fig. 12.1 (d)) and the scattering length (Fig. 12.1 (c)) behavior. The binding energy for both resonances follows the model system almost perfectly. More importantly, the scattering length for the higher field resonance reproduces the zero crossing quite precisely. We thus expect that the 2CMbg will be as successful in the three-body sector as it is in the two-body sector. Note that the obtained absolute value of $|\mu|$ (see Table 12.2, "BN-Res1" and "BN-Res2") is very close to that of the model system. In the case of the BN system, the repulsion of energy levels is considerably weaker as the bare states are farther apart from each other [39].

12.4 Three-Body Sector

Fig. 12.2(a)-(c) compares the ground and first excited Efimov states calculated within the framework of the 2CMbg (dashed lines) and the 3CM of the NB configuration (solid lines). Efimov spectrum is calculated across the Feshbach resonance centered at $B_2^{(res)}$ only. Fig. 12.2(a) (Fig. 12.2(b)) shows two binding energies as a function of the inverse scattering length (dimer binding energy E_D). Fig. 12.2(c) represents the difference between trimer and dimer binding energies as a function of E_D. The failure of the 2CMbg to reproduce the 3CM binding energy of the ground state trimer can be identified either in the positive scattering length region (Fig. 12.2(a)) or deep dimer binding energies (Fig. 12.2(b),(c)). The 2CMbg trimer simply merges with the dimer state (see dashed line), while the 3CM trimer extends across the $B_1^{(res)}$, which is indicated by solid lines in Fig. 12.2(a) that exit the figure towards $+\infty$ and reenter it back from $-\infty$. The black arrow in the figure indicates where the background Efimov trimer crosses $B_1^{(res)}$ $(1/(a - a_{bg}) = 0)$. It then continues to the lower scattering length region and only then merges with the dimer state (see the shaded area in Fig. 12.1(a),(b) which indicates the region of extension of the ground state Efimov trimer). The large discrepancy between the merging points can be clearly identified in Fig. 12.2(a) and (c). Note that the same behavior is observed in comparison of 3CM with 2CM ($a_{bg} = 0$) in [39]. Here we see that the inclusion of the background scattering length into the two-channel model does not solve this problem, indicating failure of the 2CMbg to reproduce the results of the 3CM. Finally, note that the first excited state is well captured by the 2CMbg.

Fig. 12.2(d)-(f) compares the ground and first excited Efimov states calculated within the framework of the 2CMbg (dashed lines) and the 3CM for the BN configuration (solid lines). It is clear that the results of both models are nearly identical in this case, and the results of 3CM can be reproduced well by the 2CMbg.

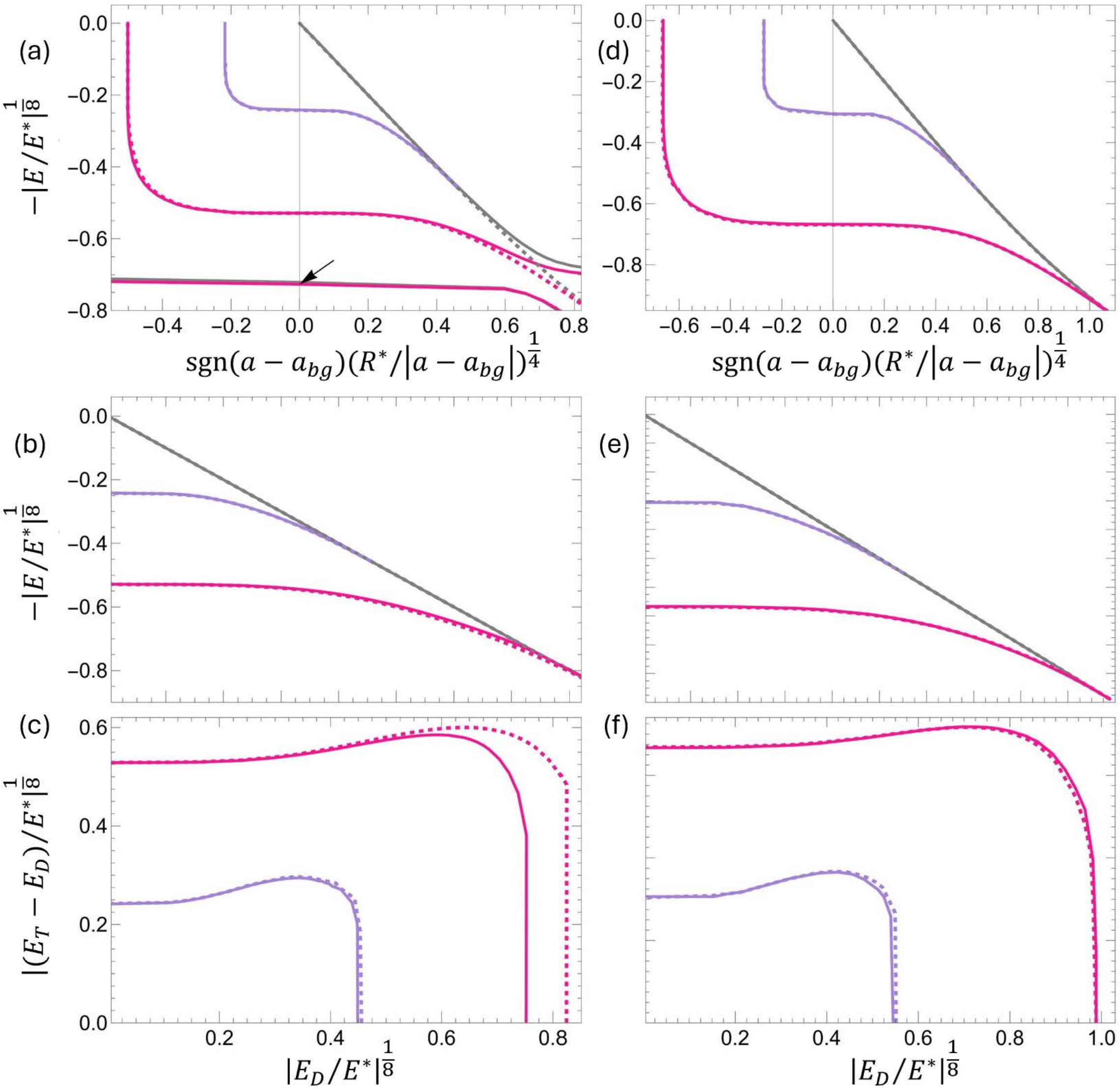

Figure 12.2: Three-body binding energies for the (a)-(c) NB and (d)-(f) BN models. Solid (dashed) lines indicate the results of 3CM (2CMbg) for the dimer (gray), Efimov ground (magenta) and the first excited (violet) states. (a) and (d) delineate the entire spectrum as a function of the inverse scattering length. In particular in (a), the ground-state trimer extends into the regime of zero scattering length and the lower resonance at B_1^{res} (indicated by an arrow). (b),(e) show the $a > 0$ regions as a function of the dimer energy. (c) and (f) represent the trimer-dimer energy difference in the same region. All energies are normalized to a characteristic energy scale $E^* = \hbar^2/(mR^*)^2$ [54].

Chapter 13

Three-Channel Model with background Scattering

A real-world example of the NB model system is ^{7}Li bb-channel [52, 55]. However, the above analysis shows that the NB system is poorly approximated by the 2CMbg, and the 3CM is a better approach. However, comparing the 3CM to the bb-channel reveals significant disagreement with the coupled-channel calculations [39] and the experimental results. Thus, the extension of the 3CM framework to non-zero background interactions has a potential to improve the performance of the model while keeping it minimalistic and avoiding heavy numerical calculations associated with the full treatment of van der Waals interactions. Our goal is to apply this model to the ^{7}Li bb-channel, which will be the subject of Chapter 14. Here, we elaborate on the extension of the three-channel model to include the background scattering (3CMbg).

13.1 Hamiltonian

The Hamiltonian for the three-channel model with background scattering is $\hat{H}^{3\mathrm{bg}} = \hat{H}_0^{3\mathrm{bg}} + \hat{H}_{int}^{3\mathrm{bg}}$, where $\hat{H}_{int}^{3\mathrm{bg}} = \hat{H}_1^{3\mathrm{bg}} + \hat{H}_2^{3\mathrm{bg}}$, and the three terms are:

$$\begin{aligned}\hat{H}_0^{3\mathrm{bg}} = \int \frac{d^3k}{(2\pi)^3} \left[\frac{\hbar^2 k^2}{2m} \hat{a}^\dagger_{\vec{k}} \hat{a}_{\vec{k}} + \left(E_{b,1} + \frac{\hbar^2 k^2}{4m}\right) \hat{b}^\dagger_{\vec{k}} \hat{b}_{\vec{k}} + \left(E_{b,2} + \frac{\hbar^2 k^2}{4m}\right) \hat{c}^\dagger_{\vec{k}} \hat{c}_{\vec{k}}\right] + \\ \Lambda_{\mathrm{bg}} \int \frac{d^3p}{(2\pi)^3} \int \frac{d^3k}{(2\pi)^3} \int \frac{d^3q}{(2\pi)^3} \chi^*_{\vec{q}} \chi_{\vec{p}}\, \hat{a}^\dagger_{\vec{p}+\frac{\vec{k}}{2}} \hat{a}^\dagger_{-\vec{p}+\frac{\vec{k}}{2}} \hat{a}_{\vec{q}+\frac{\vec{k}}{2}} \hat{a}_{-\vec{q}+\frac{\vec{k}}{2}},\end{aligned} \tag{13.1}$$

$$\hat{H}_1^{3\mathrm{bg}} = \Lambda_1 \int \frac{d^3k}{(2\pi)^3} \int \frac{d^3q}{(2\pi)^3} \left[\chi^*_{\vec{q}} \hat{b}^\dagger_{\vec{k}} \hat{a}_{\vec{q}+\frac{\vec{k}}{2}} \hat{a}_{-\vec{q}+\frac{\vec{k}}{2}} + \chi_{\vec{q}}\, \hat{a}^\dagger_{-\vec{q}+\frac{\vec{k}}{2}} \hat{a}^\dagger_{\vec{q}+\frac{\vec{k}}{2}} \hat{b}_{\vec{k}}\right], \tag{13.2}$$

$$\hat{H}_2^{3\text{bg}} = \Lambda_2 \int \frac{d^3k}{(2\pi)^3} \int \frac{d^3q}{(2\pi)^3} \left[\chi_{\vec{q}}^* \hat{c}_{\vec{k}}^\dagger \hat{a}_{\vec{q}+\frac{\vec{k}}{2}} \hat{a}_{-\vec{q}+\frac{\vec{k}}{2}} + \chi_{\vec{q}} \hat{a}^\dagger_{-\vec{q}+\frac{\vec{k}}{2}} \hat{a}^\dagger_{\vec{q}+\frac{\vec{k}}{2}} \hat{c}_{\vec{k}} \right], \tag{13.3}$$

where $\chi_{\vec{q}}$ retains the same definition as in the 2CMbg (see Eq. (11.2)). The second term in Eq. (13.1) models the background scattering as a contact interaction between atoms in the open channel. Furthermore, we set the intermolecular coupling at zero ($\Lambda_{12} = 0$), since it is a redundant parameter and can essentially be set at will (see [39]).

13.2 Two-Body Sector

Solving the Schrödinger equation $(\hat{H}_2^{3\text{bg}} - E)|\psi_{2B}\rangle = 0$ with the two-body ansatz $|\psi_{2B}\rangle$ defined in Eq. (10.5), leads to the following three coupled equations:

$$\left(\frac{\hbar^2 k^2}{m} - E \right) \alpha_{\vec{k}} + 2\Lambda_{bg} \chi_{\vec{k}} \int \frac{d^3q}{(2\pi)^3} \chi_{\vec{q}}^* \alpha_{\vec{q}} + \Lambda_1 \chi_{\vec{k}} \beta + \Lambda_2 \chi_{\vec{k}} \gamma = 0, \tag{13.4}$$

$$(E_{b,1} - E)\, \beta + 2\Lambda_1 \int \frac{d^3q}{(2\pi)^3} \chi_{\vec{q}}^* \alpha_{\vec{q}} = 0, \tag{13.5}$$

$$(E_{b,2} - E)\, \gamma + 2\Lambda_2 \int \frac{d^3q}{(2\pi)^3} \chi_{\vec{q}}^* \alpha_{\vec{q}} = 0. \tag{13.6}$$

To determine the scattering amplitude, we follow the same procedure described in 3CM and 2CMbg models. For $E = \frac{\hbar^2 k_0^2}{m} > 0$, in analogy to Eq. (11.9), the scattering amplitude $f(E)$ satisfies the following equation:

$$\frac{m \left|\chi_{\vec{k}_0}\right|^2}{4\pi\hbar^2 f(E)} = \int \frac{d^3k}{(2\pi)^3} \frac{\left|\chi_{\vec{k}}\right|^2}{(E - \frac{\hbar^2 k^2}{m} + i\eta)} - \frac{1}{2\Lambda_{bg}} \frac{(E_{b,1} - E)}{(E_{b,1} - E) - \frac{\Lambda_1^2}{\Lambda_{bg}} - \frac{\Lambda_2^2}{\Lambda_{bg}} \frac{\left(E_{b,1} - E\right)}{\left(E_{b,2} - E\right)}}. \tag{13.7}$$

It is easy to verify that setting $\Lambda_2 = 0$ in Eq. (13.7) recovers Eq. (11.9), which expresses the scattering amplitude in the 2CMbg. In the absence of open-to-closed channel couplings, i.e., for $\Lambda_i = 0$ (where $i = \{1, 2\}$) and at $E = 0$ ($k_0 = 0$), the scattering amplitude reduces to the background scattering length: $f(E = 0) = -a_{bg}$. As a result, a_{bg} for 3CMbg is the same as for 2CMbg (see Eq. (11.10)). The scattering length is then calculated along the same lines as in 2CMbg and yields the following:

$$a = a_{bg}\left(1 + \frac{\left(\frac{a_{bg}}{\sqrt{\pi}b\Lambda_{bg}} - \frac{1}{\Lambda_{bg}}\right)\frac{\Lambda_1^2}{\mu_1}\left(B_2 - B\right) + \left(\frac{a_{bg}}{\sqrt{\pi}b\Lambda_{bg}} - \frac{1}{\Lambda_{bg}}\right)\frac{\Lambda_2^2}{\mu_2}\left(B_1 - B\right)}{\left(B_1 - B\right)\left(B_2 - B\right) - \frac{a_{bg}}{\sqrt{\pi}b\Lambda_{bg}}\frac{\Lambda_2^2}{\mu_2}\left(B_1 - B\right) - \frac{a_{bg}}{\sqrt{\pi}b\Lambda_{bg}}\frac{\Lambda_1^2}{\mu_1}\left(B_2 - B\right)}\right). \tag{13.8}$$

The scattering length can be parametrized as following [52]:

$$a = a_{bg}\left(1 - \frac{\Delta B_1}{B - B_1^{(res)}} - \frac{\Delta B_2}{B - B_2^{(res)}}\right), \tag{13.9}$$

where a_{bg}, ΔB_i and $B_i^{(res)}$ are five observable parameters which can be directly related to bare parameters of the model by a direct comparison with Eq. (13.8) (see next section).

To complete the two-body sector, Eqs. (13.4)-(13.6) are solved for the binding energy ($E = -\hbar^2\lambda_D^2/m < 0$), which is found to satisfy the following equation:

$$\left(1 - \frac{\Lambda_1^2}{\Lambda_{bg}\left(E_{b,1} + \hbar^2\lambda_D^2/m\right)} - \frac{\Lambda_2^2}{\Lambda_{bg}\left(E_{b,2} + \hbar^2\lambda_D^2/m\right)}\right) \cdot \left(-\pi\lambda\exp(b^2\lambda_D^2)\mathrm{erfc}(\lambda_D b) + \frac{\sqrt{\pi}}{b}\right) = -\frac{2\pi^2\hbar^2}{m\Lambda_{bg}}. \tag{13.10}$$

13.2.1 Relating the Bare Parameters to the Observable Parameters in 3CMbg

We aim to link the five bare parameters $\{\Lambda_1, \Lambda_2, b, B_2, B_1\}$ to the four observable parameters $\{B_1^{res}, B_2^{res}, \Delta B_1, \Delta B_2\}$.

This is accomplished by comparing Eq. (13.8) to Eq. (13.9), which yields:

$$B_{1,2}^{res} = \frac{-C_4 C_1}{2C_3} + \frac{1}{2}(B_1 + B_2) \pm \frac{R}{2\sqrt{\pi}} \tag{13.11}$$

$$\Delta B_1 = -\frac{\sqrt{\pi}(C_4 - 1)}{2C_3^2 R}\left(C_4 C_1^2 - C_3 C_2(B_2 - B_1) - \frac{C_3 C_1 R}{\sqrt{\pi}}\right) \tag{13.12}$$

$$\Delta B_2 = \frac{\sqrt{\pi}(C_4 - 1)}{2C_3^2 R}\left(C_4 C_1^2 - C_3 C_2(B_2 - B_1) + \frac{C_3 C_1 R}{\sqrt{\pi}}\right) \tag{13.13}$$

where we have defined:

$$R = \sqrt{\frac{C_1^2 C_4^2 \pi}{C_3^2} + \frac{2\pi C_4(B_1 - B_2)C_2}{C_3} + (B_1 - B_2)^2\pi)} \tag{13.14}$$

and $C_1 = \Lambda_2^2\mu_1 + \Lambda_1^2\mu_2$, $C_2 = \Lambda_2^2\mu_1 - \Lambda_1^2\mu_2$, $C_3 = \Lambda_{bg}\mu_1\mu_2$, $C_4 = \frac{a_{bg}}{b\sqrt{\pi}}$. From Eq. (11.10), it is clear that Λ_{bg} is not an independent parameter. It is rather defined by a_{bg} and b through the relation:

$$\Lambda_{bg} = \frac{2\hbar^2\pi^{\frac{3}{2}}}{m}\left(\frac{b a_{bg}}{b\sqrt{\pi} - a_{bg}}\right) \tag{13.15}$$

The model has five bare but only four observable parameters. Thus, one free parameter exists which we chose to be b. By fixing the value of b, we can establish a mapping between the bare and observable parameters using the relations outlined above. This provides a straightforward way to connect our theoretical model with the experimental observables.

13.3 Three-Body Sector: Efimov Trimers

The trimer binding energy $E_T = -\hbar^2\lambda_T^2/m$ is found by solving the Schrödinger equation $(\hat{H} - E_T)|\psi_{3B}\rangle = 0$ with the three-body ansatz defined in Eq. (10.11), leads to the following coupled equations:

$$\left(\frac{\hbar^2 q^2}{m} + \frac{3}{4}\frac{\hbar^2 k^2}{m} - E\right)\alpha_{\vec{k},\vec{q}} + \Lambda_1 \chi_{\vec{q}}\,\beta_{\vec{k}} + \Lambda_2 \chi_{\vec{q}}\,\gamma_{\vec{k}} + 2\Lambda_{bg}\chi_{\vec{q}}\int \frac{d^3q}{(2\pi)^3}\chi^*_{\vec{q}}\left[\alpha_{\vec{k},\vec{q}} + 2\alpha_{\vec{q}-\frac{\vec{k}}{2},-\frac{\vec{q}}{2}-\frac{3\vec{k}}{4}}\right] = 0, \tag{13.16}$$

$$\left(\frac{3}{4}\frac{\hbar^2 k^2}{m} + E_{b,1} - E\right)\beta_{\vec{k}} + 2\Lambda_1 \int \frac{d^3q}{(2\pi)^3}\chi^*_{\vec{q}}\left[\alpha_{\vec{k},\vec{q}} + 2\alpha_{\vec{q}-\frac{\vec{k}}{2},-\frac{\vec{q}}{2}-\frac{3\vec{k}}{4}}\right] = 0, \tag{13.17}$$

$$\left(\frac{3}{4}\frac{\hbar^2 k^2}{m} + E_{b,2} - E\right)\gamma_{\vec{k}} + 2\Lambda_2 \int \frac{d^3q}{(2\pi)^3}\chi^*_{\vec{q}}\left[\alpha_{\vec{k},\vec{q}} + 2\alpha_{\vec{q}-\frac{\vec{k}}{2},-\frac{\vec{q}}{2}-\frac{3\vec{k}}{4}}\right] = 0. \tag{13.18}$$

Solving this set of equations to find the trimer binding energy, we get:

$$\begin{aligned}
&\left(\frac{1}{\frac{\Lambda_1^2}{\frac{3}{4}\frac{\hbar^2k^2}{m}+E_{b,1}+\hbar^2\lambda^2/m} + \frac{\Lambda_2^2}{\frac{3}{4}\frac{\hbar^2k^2}{m}+E_{b,2}+\hbar^2\lambda^2/m} - \Lambda_{bg}}\right)\beta_k^{\text{eff}} = \\
&\frac{m}{\hbar^2}\frac{\beta_k^{\text{eff}}}{2\pi^2 b}\left(-\pi b\left(\lambda^2 + \frac{3}{4}k^2\right)^{\frac{1}{2}}\exp\left(b^2\left(\lambda^2+\frac{3}{4}k^2\right)\right)\operatorname{erfc}\left(b\left(\lambda^2+\frac{3}{4}k^2\right)^{\frac{1}{2}}\right) + \sqrt{\pi}\right) + \\
&\frac{m}{\pi^2\hbar^2}\int dq\,\beta_q^{\text{eff}} q^2 \exp\left(-\frac{5}{8}q^2 b^2\right)\exp\left(-\frac{5}{8}k^2 b^2\right)\frac{\exp\left(b^2\left(\lambda^2+k^2+q^2\right)\right)}{kq}\left[E_1\left(v(-1)\right) - E_1\left(v(1)\right)\right],
\end{aligned} \tag{13.19}$$

where $E_1(z) = \int_1^\infty ds \frac{e^{-sz}}{s}$ is the exponential integral and

$$v(j) = b^2 \left(\lambda^2 + k^2 + q^2 + jkq\right). \tag{13.20}$$

The steps are similar for both the two-channel and the three-channel models. First, we define $\psi(k) = k\beta_k^{\text{eff}}$, switch variables using Eq. (11.24) and rescale $\psi(\xi) \to \frac{\psi(\xi)}{\cosh(\xi)}$. Limiting ourselves to odd solutions in $\psi(\xi)$, we can extend the integration range to $-\infty$ and get the integral equation in the form: $\int_{-\infty}^{\infty} d\xi' \mathcal{M}_{\lambda_T}(\xi, \xi')\psi(\xi') = 0$ where the matrix elements are given by:

$$M(\xi, \xi') = \delta(\xi - \xi') F(\xi') - \delta(\xi - \xi') f(\xi') - L(\xi, \xi'), \tag{13.21}$$

where :

$$F(\xi) = \frac{\hbar^2}{m\lambda_T \cosh\xi} \left[\left(\frac{\Lambda_1^2}{\frac{\hbar^2}{m}\lambda_T^2 \cosh^2\xi + \mu_1 (B_1 - B)} \right) + \left(\frac{\Lambda_2^2}{\frac{\hbar^2}{m}\lambda_T^2 \cosh^2\xi + \mu_2 (B_2 - B)} \right) - \Lambda_{bg} \right]^{-1}, \tag{13.22}$$

$$f(\xi) = \frac{1}{2\pi^2 b} \left[-\pi b \exp\left((b\lambda_T \cosh\xi)^2 \right) \operatorname{erfc}\left(b\lambda_T \cosh(\xi)\right) + \frac{\sqrt{\pi}}{\lambda_T \cosh(\xi)} \right], \tag{13.23}$$

$$L(\xi, \xi') = \frac{1}{\sqrt{3}\pi^2} \exp\left((b\lambda_T)^2 \left(1 + \frac{1}{2}\sinh^2(\xi) + \frac{1}{2}\sinh^2(\xi') \right) \right) \cdot \left(E_1\left((b\lambda_T)^2 (t(-1)) \right) - E_1\left((b\lambda_T)^2 (t(1)) \right) \right), \tag{13.24}$$

where $t(j)$ is defined in Eq. (11.26). The requirement of a vanishing determinant, $\det M_{\lambda_T}(\xi, \xi') = 0$, provides an implicit equation for λ_T which can be solved numerically. Among many possible solutions, λ_T should satisfy the condition $\lambda_T > \max\{0, \lambda_D\}$.

Chapter 14

Efimov Scenario in Bosonic Lithium

In this section, we apply the 3CMbg on ^{7}Li *bb*-channel which provides an example of two overlapping narrow Feshbach resonances extensively studied in recent experiments [56–61]. An example of an isolated narrow Feshbach resonance is provided by the ^{7}Li *aa*-channel, which has also been experimentally studied in [62–64]. We apply the 2CMbg to the latter and compare it with the performance of the 3CMbg on the *bb*-channel. For both models, we fix the magnetic moment to $\mu = -2.66$ MHz/G for the *aa*-channel and $\mu_1 = \mu_2 = \mu$ for the *bb*-channel to match the coupled-channel calculations. The characteristic range of the interactions of ^{7}Li atoms (the van der Waals length $r_{\mathrm{vdW}} = (mC_6/\hbar^2)^{1/4}/2 = 32a_0$, where C_6 is the dispersion coefficient and a_0 is the Bohr radius) and the background scattering length a_{bg} are small.

14.1 ^{7}Li *bb*-Channel

The *bb*-channel ($|F = 1, m_f = 0\rangle$) features two Feshbach resonances characterized by the dimensionless strength parameters $s_{\mathrm{res},1} = 0.0411$ ($R_1^* = 722a_0$) and $s_{\mathrm{res},2} = 0.493$ ($R_2^* = 60a_0$) [52] $s_{\mathrm{res},1} \ll s_{\mathrm{res},2} < 1$ ($R_1^* \gg R_2^* > r_{\mathrm{vdW}}$) indicates that both resonances are narrow and can be classified as NB systems.

14.1.1 Two-Body Sector

To determine the bare parameters of our model, we fit the coupled-channel calculations scattering length with Eq. (13.9) as shown in Fig. 14.1(a), and summarize the fitting parameters in Table 14.1. Then, the analytic expressions shown in section 13.2.1 are used to extract the bare parameters of the model. However, there are only four equations for five bare parameters, and we are free to choose one of them to complete the settings by fitting the binding energy. The most reasonable choice is to fit b as

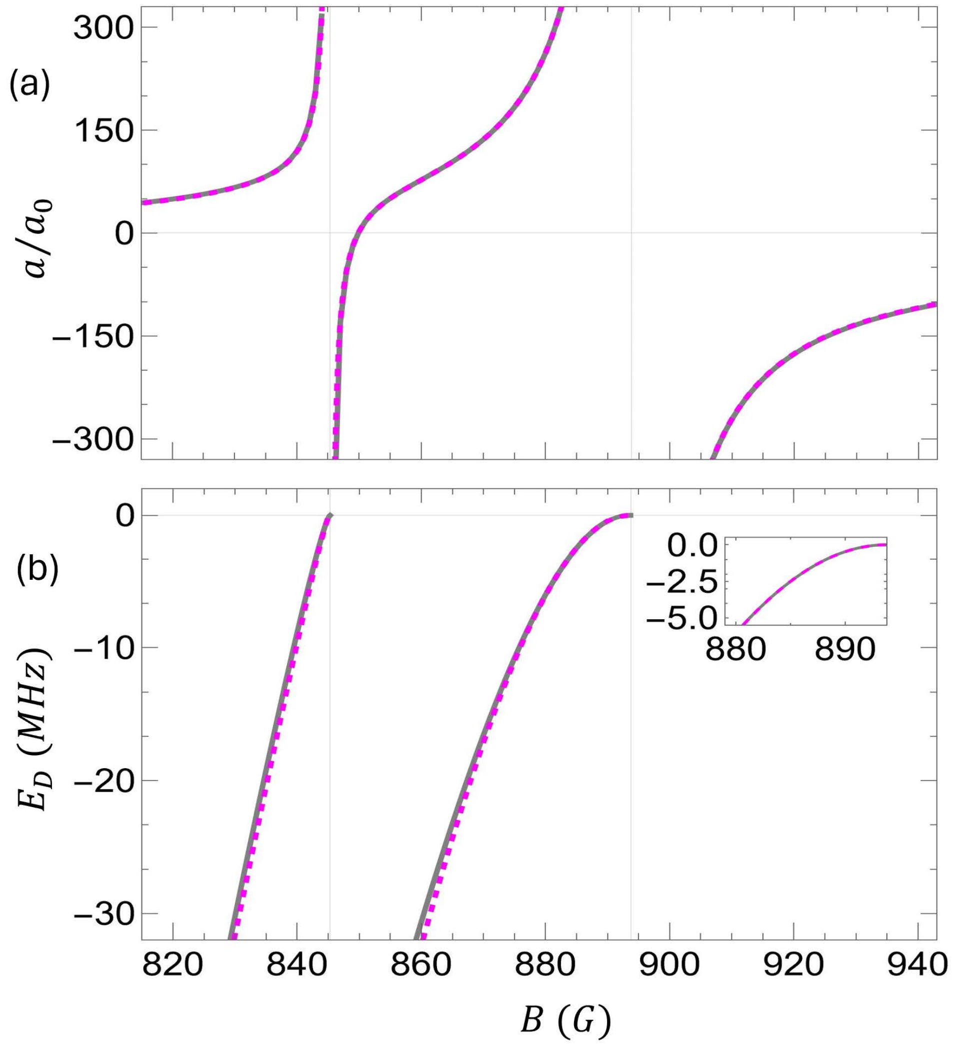

Figure 14.1: Two-body sector of ^{7}Li *bb*-channel: (a) the scattering length, and (b) the dimer binding energy, as obtained from the 3CMBg model (dashed magenta) are compared with the exact coupled-channel calculations (solid gray).

it signifies the range of the model interaction potential. It is expected though that the Gaussian approximation of the real van der Waals potential will be applicable to a limited range only. To verify the range of applicability, we chose to fit the position of the Feshbach resonance $B_2^{(\mathrm{res})}$ as an additional parameter. Fig. 14.1(b) shows the result of the binding energy fitting with the fitting range limited to -5 MHz which is the maximal range we used here. Very good agreement with the coupled-channel calculations is confirmed for binding energies down to ~ -10 MHz. We obtain the position of the "broad" resonance at $B_2^{(\mathrm{res})} = 893.83$ G which deviates from the position defined by the scattering length by a tiny amount of $\sim 5 \times 10^{-5}$ G (see Table 14.1). The corresponding potential range is $b = 23.76\, a_0$ (see Table 14.2). Then, using the analytical expressions outlined in section 13.2.1, the bare parameters are determined and shown in Table 14.2.

Type	$B_1^{(res)}$ (G)	$B_2^{(res)}$ (G)	ΔB_1 (G)	ΔB_2 (G)	a_{bg}/a_0
bb-channel	845.31	893.78	−18.021	−216.12	−18.531
aa-channel	–	737.69	–	−172.02	−20.14

Table 14.1: Fitting parameters of the ^{7}Li coupled-channel calculations.

Type	B_1 (G)	B_2 (G)	$\Lambda_1/(E_0 a_0^{3/2})$	$\Lambda_2/(E_0 a_0^{3/2})$	$\Lambda_{bg}/(E_0 a_0^3)$	b/a_0
bb-channel	813.8	853.7	0.244	0.089	-80.88	23.76
aa-channel	–	702.4	–	0.266	-100.6	44.09

Table 14.2: Bare parameters of the 3CMBg for ^{7}Li *bb*- and *aa*-channels.

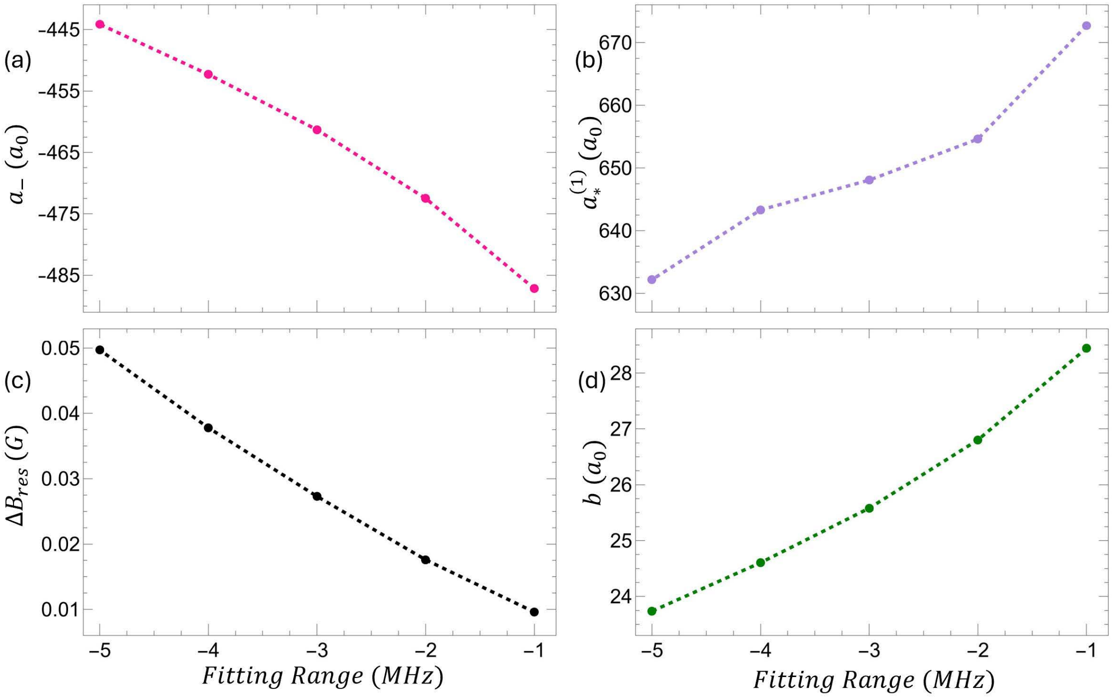

Figure 14.2: ^{7}Li *bb*-channel: variations of (a) a_- and (b) $a_*^{(1)}$ as a function of the binding energy fitting range derived from the 3CMbg model; (c) $\Delta B_2^{(res)} = (B_2^{(res)}|_{E_D=0} - B_2^{(res)}|_{a=\infty})$ and (d) change in the interaction range b as a function of the fitting range.

14.1.2 Three-Body Sector

Once the parameters are fixed in the two-body sector, the Efimov trimer energies can be calculated according to Section 13.3. Our primary interest lies in the determination of the scattering length a_-, which corresponds to the intersection of the ground state Efimov trimer with the three-body continuum, and $a_*^{(1)}$, marking the merging of the first excited Efimov trimer state with the atom-dimer continuum. These Efimov resonances can be directly compared with the experimental results.

As discussed, the value of the parameter b depends on the fitting range, which affects other parameters and ultimately the position of the Efimov resonances. Fig. 14.2 (a) and (b) show the positions of a_- and $a_*^{(1)}$ as a function of the fitting ranges down to -5 MHz. The general trend for both resonances to move to smaller absolute values is in agreement with [54] which indicates that the final background scattering length leads to the same qualitative behavior. However, the experimental value $a_- = -280\, a_0$ [57] is impossible to achieve with this theory. Comparison of the experimental value of $a_*^{(1)} = 170\, a_0$ [58, 61] leads to the same conclusion (see Fig. 14.2(b)). The quality of the approximation is visible in Fig. 14.2 (c) where $\Delta B_2^{(res)} = (B_2^{(res)}|_{E_D=0} - B_2^{(res)}|_{a=\infty})$ is plotted. The fitting of the binding energy is limited to -5 MHz because $\Delta B_2^{(res)}$ exceeds the fitting error of the resonance position extracted from the scattering length (see Fig. 14.1(c)), which is equal to 40 mG [55]. To correctly predict the position of Efimov resonances, the use of the van der Waals potential is unavoidable, leading to heavy multi-channel numerical calculations [38]. In conclusion, the Feshbach resonance in the bb-channel is not narrow enough to allow for simplified treatment within the 3CMBg framework to provide us with quantitative predictions.

14.2 ^{7}Li *aa*-Channel

^{7}Li aa-channel ($|F = 1, m_f = 1\rangle$), having an isolated Feshbach resonance, can be treated within the 2CMbg framework. The resonance is characterized by the $s_{\text{res}} = 0.56$ ($R^* = 54.6\, a_0$) which indicates that it is rather similar to the "broad" resonance in the bb-channel.

The bare parameters of the model are obtained in the same way as before. The fitting of the coupled-channel calculations is shown in Fig. 14.3 (a) and (b) and the parameters are summarized in Table 14.1 while the derived bare parameters of the model are found in Table 14.2. The agreement of the 2CMbg with the coupled-channel calculations is excellent as can be seen especially well in the fitting of the binding energy which is done down to -5 MHz but shown in Fig. 14.3 (b) all the way down to -200 MHz ($\sim 40\%$ of the van der Waals energy).

Despite this excellent agreement in the two-body sector, the three-body energy levels miss the experimental results even more significantly than for the case of the bb-channel. Fig. 14.4 illustrates the position of the Efimov resonance (a_-) obtained as a function of the fitting range. As before, we find that the values are far from the experimental results reported in [58], where a_- was estimated to be $a_- \approx -200\, a_0$. Interestingly, the prediction for the bb-channel agrees somewhat better with the experiment compared to the aa-channel. We thus speculate that this might be attributed to the influence of the second, truly narrow resonance for which the 3CMBg is expected

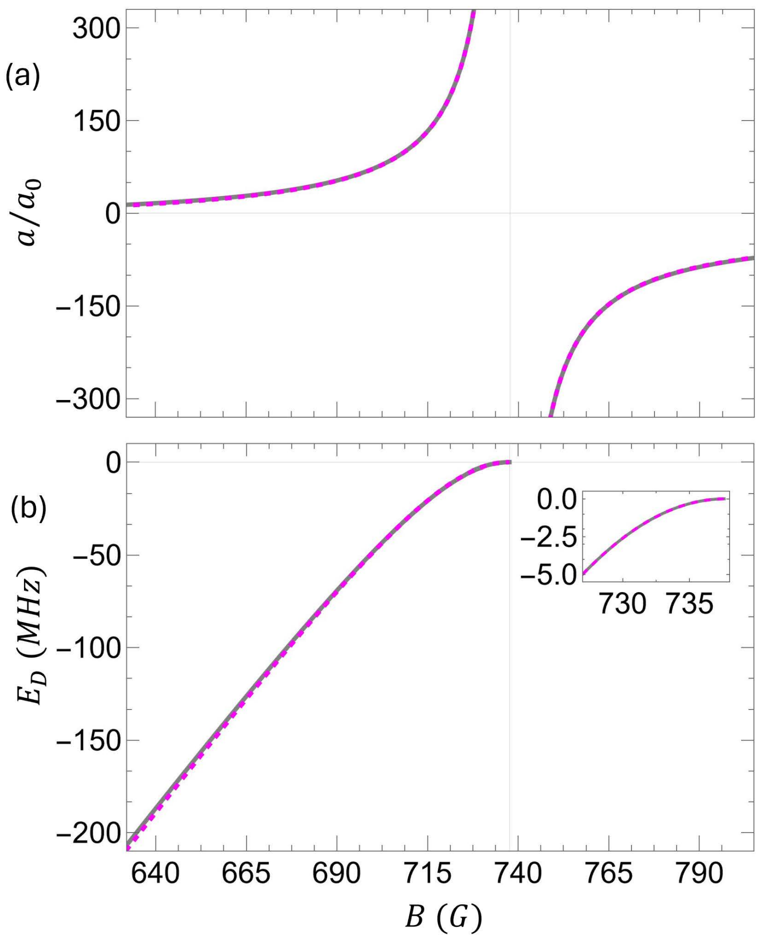

Figure 14.3: Two-body sector of ^{7}Li aa-channel: (a) the scattering length, and (b) the dimer binding energy, as obtained from the 3CMbg model (dashed magenta) are compared with the exact coupled-channel calculations (solid gray).

to work better.

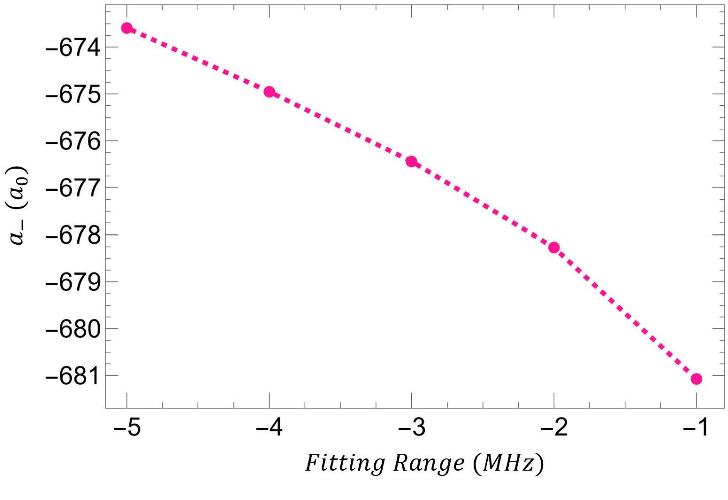

Figure 14.4: ^{7}Li aa-channel: variation of a_- as a function of the binding energy fitting range derived from the 2CMbg model.

Chapter 15

Summary & Conclusions

In this thesis, two distinct projects are investigated: the development of a Zeeman slower using permanent magnets, and the impact of background scattering on the Efimov scenario for overlapping narrow Feshbach resonances.

- **First Project:**

  In conclusion, we have described the theory, design, optimization, construction, and assembly of a spin-flip transverse Zeeman slower using permanent magnets based on Halbach configuration arrangement. Compared to the conventional wire-wound Zeeman slower, our design presents a superior and attractive alternative with several advantages:

  - It requires no electric power consumption or water cooling, thereby eliminating the risks of electric shorts.
  - It is easy to assemble and disassemble without breaking the vacuum, which is especially useful for high-temperature bake-outs.
  - It produces a very smooth and homogeneous transverse magnetic field with low stray magnetic fields.
  - It avoids perturbations associated with the heating of the Zeeman slower coils.
  - It is flexible, adjustable, and inexpensive due to its reliance on 3D printing technology.

  Our innovative use of small magnets and detailed mechanical design, including solutions to various challenges, can be particularly valuable for researchers working with cold atoms. This design can be optimized for any alkali metal, such as Na, K, Rb, Cs, and alkaline earth metals such as Sr and Yb. Additionally, the proposed design can help create a setup based on permanent magnets that produces a highly homogeneous magnetic field, which is crucial for the science chamber, a topic currently being researched by our group.

In our experiments, we observed that the atoms reached low velocities at the end of the slower, with some velocities recorded at 50 [m/s] low enough to be trapped in the MOT. However, we still need to connect the MOT to measure the flux, and this aspect remains under investigation.

The spin-flip configuration was chosen for its ability to provide a low magnetic field near the MOT, although it posed open questions regarding the performance of the Zeeman slower. Specifically, at the zero-crossing point, atoms can be optically pumped to dark states, and the unavoidable presence of both circular polarizations in the laser light (due to transverse magnetic field configuration) may prevent their repumping back to the right energy state. Skepticism has been expressed in the literature as to the feasibility of such a configuration [15]. However, we provide experimental proof that the Zeeman slower works well and provides a good flux of slow atoms for their consequent loading into MOT.

- **Second Project:** In conclusion, we examine how the three-channel model (3CM) developed to describe two overlapping Feshbach resonances compares with the two-channel model extended to include background scattering (2CMbg) for different model systems. Specifically, we find that while 2CMbg is a viable substitute for 3CM for the broad-narrow (BN) model system, it fails to correctly reproduce the 3CM for the NB one.

  To further investigate the contribution of the background scattering length, we extend the 3CM framework to include the background interactions (3CMbg) and apply it to the ^{7}Li *bb*-channel. Furthermore, we apply the 2CMbg model to the ^{7}Li *aa* channel and compare it to the performance of the 3CMbg for the *bb* channel. Despite the simplicity of our models, we find good agreement with the coupled-channel calculations of the binding energies in the two-body sector. Although the inclusion of the background scattering length improves the performance of models in the three-body sector, significant discrepancies remain between the predicted and experimentally found positions of the Efimov resonances. These discrepancies can be attributed to the intermediate character of the relevant ^{7}Li Feshbach resonances ($s_{\text{res}} \sim 1$). Finally, we note a curious observation that the 3CMbg for the *bb*-channel performs better than the 2CMbg for the *aa*-channel which might be attributed to the influence of the second resonance in the overlapping pair of resonances in the *bb*-channel.

Bibliography

[1] I. Bloch. “Ultracold quantum gases in optical lattices”. In: *Nature Physics* 1.1 (2005), pp. 23–30.

[2] I. Bloch. “Quantum coherence and entanglement with ultracold atoms in optical lattices”. In: *Nature* 453 (2008), pp. 1016–1022.

[3] I. Bloch, J. Dalibard, and S. Nascimbene. “Quantum simulations with ultracold quantum gases”. In: *Nature Physics* 8 (2012), pp. 267 –276.

[4] D. S. Jin and J. Ye. “Introduction to Ultracold Molecules: New Frontiers in Quantum and Chemical Physics”. In: *Chemical Reviews* 112.9 (2012), pp. 4801–4802.

[5] B. J. Bloom, T. L. Nicholson, J. R. Williams, S. L. Campbell, M. Bishof, X. Zhang, W. Zhang, S. L. Bromley, and J. Ye. “An optical lattice clock with accuracy and stability at the 10−18 level”. In: *Nature* 506.7486 (2014), pp. 71–75.

[6] F. Hamodi and L. Khaykovich. “Extracting atoms one by one from a small matter-wave soliton”. In: *Journal of Physics B: Atomic, Molecular and Optical Physics* 53.5 (2020), p. 055301.

[7] P. Cheiney, O. Carraz, D. Bartoszek-Bober, S. Faure, F. Vermersch, C. Fabre, G. L. Gattobigio, T. Lahaye, D. guéry odelin, and R. Mathevet. “A Zeeman slower design with permanent magnets in a Halbach configuration”. In: *The Review of scientific instruments* 82 (2011), p. 063115.

[8] E. Wodey, R. J. Rengelink, C. Meiners, E. M. Rasel, and D. Schlippert. “A robust, high-flux source of laser-cooled ytterbium atoms”. In: *Journal of Physics B: Atomic, Molecular and Optical Physics* 54.3 (2021), p. 035301.

[9] S. P. Krzyzewski, T. G. Akin, P. Dahal, and E. R. I. Abraham. “A clip-on Zeeman slower using toroidal permanent magnets”. In: *Review of Scientific Instruments* 85.10 (2014), p. 103104.

[10] I. R. Hill, Y. B. Ovchinnikov, E. M. Bridge, E. A. Curtis, and P. Gill. “Zeeman slowers for strontium based on permanent magnets”. In: *Journal of Physics B: Atomic, Molecular and Optical Physics* 47.7 (2014), p. 075006.

[11] Y. Ovchinnikov. “A permanent Zeeman slower for Sr atomic clock”. In: *European Physical Journal: Special Topics* 163 (2008), pp. 95–100.

[12] X. Zhang and X. Xu. “Optimized design of a permanent Zeeman slower for an ytterbium optical lattice clock”. In: *Laser Physics* 26.7 (2016), p. 075501.

[13] Q. Wang, Y.-G. Lin, F.-L. Gao, Y. Li, B.-K. Lin, F. Meng, E.-J. Zang, T.-C. Li, and Z.-J. Fang. “A Longitudinal Zeeman Slower Based on Ring-Shaped Permanent Magnets for a Strontium Optical Lattice Clock*”. In: *Chinese Physics Letters* 32.10 (2015), p. 100701.

[14] G. Reinaudi, C. B. Osborn, K. Bega, and T. Zelevinsky. “Dynamically configurable and optimizable Zeeman slower using permanent magnets and servomotors”. In: *J. Opt. Soc. Am. B* 29.4 (2012), pp. 729–733.

[15] Y. B. Ovchinnikov. “Longitudinal Zeeman slowers based on permanent magnetic dipoles”. In: *Optics Communications* 285.6 (2012), pp. 1175–1180.

[16] C. Chin, R. Grimm, P. Julienne, and E. Tiesinga. “Feshbach resonances in ultracold gases”. In: *Rev. Mod. Phys.* 82 (2010), p. 1225.

[17] V. Efimov. “Energy levels arising from resonant two-body forces in a three-body system”. In: *Phys. Lett. B* 33 (1970), pp. 563–564.

[18] P. Naidon and S. Endo. “Efimov physics: a review”. In: *Rep. Prog. Phys.* 80 (2017), p. 056001.

[19] C. H. Greene, P. Giannakeas, and J. Pérez-Ríos. “Universal few-body physics and cluster formation”. In: *Rev. Mod. Phys.* 89 (2017), p. 035006.

[20] J. P. D’Incao. “Few-body physics in resonantly interacting ultracold quantum gases”. In: *J. Phys. B: At. Mol. Opt. Phys.* 51 (2018), p. 043001.

[21] D. S. Petrov. “Three-boson problem near a narrow Feshbach resonance”. In: *Phys. Rev. Lett.* 93 (2004), p. 143201.

[22] A. O. Gogolin, C. Mora, and R. Egger. “Analytical solution of the bosonic three-body problem”. In: *Phys. Rev. Lett.* 100 (2008), p. 140404.

[23] L. Pricoupenko. “Crossover in the Efimov spectrum”. In: *Phys. Rev. A* 82 (2010), p. 043633.

[24] Y. Nishida. “New type of crossover physics in three-component Fermi gases”. In: *Phys. Rev. Lett* 109 (2012), p. 240401.

[25] Y. Nishida. “Polaronic atom-trimer continuity in three-component Fermi gases”. In: *Phys. Rev. Lett* 114 (2015), p. 115302.

[26] W. Yi and X. Cui. “Polarons in ultracold Fermi superfluides”. In: *Phys. Rev. A* 92 (2015), p. 013620.

[27] M. Pierce, X. Leyronas, and F. Chevy. “Few- versus many-body physics of an impurity immersed in a superfluid of spin 1/2 attractive fermions”. In: *Phys. Rev. Lett.* 123 (2019), p. 080403.

[28] F. Werner, L. Tarruell, and Y. Castin. “Number of closed-channel molecules in the BEC-BCS crossover”. In: *Eur. Phys. J. B* 68 (2009), pp. 401–415.

[29] M. Jona-Lasino and L. Pricoupenko. “Three resonant ultracold bosons: Off-resonance effects”. In: *Phys. Rev. Lett.* 104 (2010), p. 023201.

[30] L. Pricoupenko and M. Jona-Lasinio. “Ultracold bosons in the vicinity of a narrow resonance: shallow dimer and recombination”. In: *Phys. Rev. A* 84 (2011), p. 062712.

[31] Y. Wang and P. S. Julienne. “Universal van der Waals physics for three cold atoms near Feshbach resonances”. In: *Nat. Phys.* 10 (2014), pp. 768–773.

[32] K. Kato, Y. Wang, J. Kobayashi, P. S. Julienne, and S. Inouye. “Isotopic Shift of Atom-Dimer Efimov Resonances in K-Rb Mixtures: Critical Effect of Multichannel Feshbach Physics”. In: *Phys. Rev. Lett.* 118 (2017), p. 163401.

[33] R. Chapurin, X. Xie, M. J. Van de Graaff, J. S. Popowski, J. P. D’Incao, P. S. Julienne, J. Ye, and E. A. Cornell. “Precision Test of the Limits to Universality in Few-Body Physics”. In: *Phys. Rev. Lett.* 123 (2019), p. 233402.

[34] X. Xie, M. J. Van de Graaff, R. Chapurin, M. D. Frye, J. M. Hutson, J. P. D’Incao, P. S. Julienne, J. Ye, and E. A. Cornell. “Observation of Efimov Universality across a Non-Universal Feshbach Resonance in 39K”. In: *Phys. Rev. Lett.* 125 (2020), p. 243401.

[35] T. Secker, D. J. M. Ahmed-Braun, P. M. A. Mestrom, and S. J. J. M. F. Kokkelmans. “Multichannel effects in the Efimov regime from broad to narrow Feshbach resonances”. In: *Phys. Rev. A* 103 (2021), p. 052805.

[36] J.-L. Li, T. Secker, P. M. A. Mestrom, and S. J. J. M. F. Kokkelmans. “Strong spin-exchange recombination of three weakly interacting ^{7}Li atoms”. In: *Phys. Rev. Res.* 4 (2022), p. 023103.

[37] K.-M. Tempest and S. Jonsell. “Multichannel hyperspherical model for Efimov physics with van der Waals interactions controlled by a Feshbach resonance”. In: *Phys. Rev. A* 107 (2023), p. 053319.

[38] J. van de Kraats, D. J. M. Ahmed-Braun, J.-L. Li, and S. J. J. M. F. Kokkelmans. “Emergent Inflation of the Efimov Spectrum under Three-Body Spin-Exchange Interactions”. In: *Phys. Rev. Lett.* 132 (2024), p. 133402.

[39] Y. Yudkin and L. Khaykovich. “Efimov scenario for overlapping narrow Feshbach resonances”. In: *Phys. Rev. A* 103 (2021), p. 063303.

[40] A. Li, Y. Yudkin, P. S. Julienne, and L. Khaykovich. "Efimov resonance position near a narrow Feshbach resonance in a ^{6}Li$-^{133}$Cs mixture". In: *Phys. Rev. A* 105 (2022), p. 053304.

[41] Y. Yudkin. "Laser Cooling at Resonance". Master's Thesis PDF. Master's thesis. Bar-Ilan University, 2018.

[42] P. Petrov. "Quantum Noise Limited Light Interferometry with Cold Trapped Atoms". Ph.D. Thesis PDF. PhD thesis. University of Copenhagen, 2006.

[43] J. Kluge. "Design of a Zeeman slower for a second generation experimental setup on quantum degenerate Dysprosium gases". Master's Thesis PDF. Master's thesis. Universität Stuttgart, 2019.

[44] J. Steinmann. "Multiphoton Ionization of Laser Cooled Lithium". Ph.D. Thesis PDF. PhD thesis. University of Heidelberg, 2007.

[45] N. Ramsey. *Molecular Beams.* Oxford University Press, 1985.

[46] F. Serwane. "The setup of a Magneto Optical Trap for the preparation of a mesoscopic degenerate". Master's Thesis PDF. Master's thesis. Max-Planck-Institute for Nuclear Physics, 2007.

[47] K. Halbach. "Design of Permanent Multipole Magnets with Oriented Rare Earth Cobalt Material". In: *Nucl. Instrum. Meth.* 169 (1980), p. 1.

[48] T. Meyrath. "Experiments with Bose-Einstein Condensation in a Optical Box". Ph. D. Thesis PDF. PhD thesis. University of Maryland, 2005.

[49] C. Chin, R. Grimm, P. Julienne, and E. Tiesinga. "Feshbach resonances in ultracold gases". In: *Rev. Mod. Phys.* 82 (2010), pp. 1225–1286.

[50] G. F. Gribakin and V. V. Flambaum. "Calculation of the scattering length in atomic collisions using the semiclassical approximation". In: *Phys. Rev. A* 48 (1993), pp. 546–553.

[51] J. P. D'Incao. "Few-body physics in resonantly interacting ultracold quantum gases". In: *Journal of Physics B: Atomic, Molecular and Optical Physics* 51.4 (2018), p. 043001.

[52] K. Jachymski and P. S. Julienne. "Analytical model of overlapping Feshbach resonances". In: *Phys. Rev. A* 88 (2013), p. 052701.

[53] G. V. Skorniakov and K. A. Ter-Martirosian. "Three body problem for short range forces. I. Scattering of low energy neutrons by deuterons". In: 1957.

[54] C. Langmack, R. Schmidt, and W. Zwerger. "Efimov states near a Feshbach resonance and the limits of van der Waals universality at finite background scattering length". In: *Phys. Rev. A* 97 (2018), p. 033623.

[55] P. S. Julienne and J. M. Hutson. “Contrasting the wide Feshbach resonances in 6Li and 7Li”. In: *Phys. Rev. A* 89 (2014), p. 052715.

[56] N. Gross, Z. Shotan, S. J. J. M. F. Kokkelmans, and L. Khaykovich. “Observation of universality in ultracold ^{7}Li three-body recombination”. In: *Phys. Rev. Lett.* 103 (2009), p. 163202.

[57] N. Gross, Z. Shotan, O. Machtey, S. J. J. M. F. Kokkelmans, and L. Khaykovich. “Study of Efimov physics in two nuclear-spin sublevels of ^{7}Li”. In: *C.R. Physique* 12 (2011), pp. 4–12.

[58] O. Machtey, D. A. Kessler, and L. Khaykovich. “Universal dimer in a collisionally opaque medium: experimental observables and Efimov resonances”. In: *Phys. Rev. Lett.* 108 (2012), p. 130403.

[59] Z. Shotan, O. Machtey, S. J. J. M. F. Kokkelmans, and L. Khaykovich. “Three-Body Recombination at Vanishing Scattering Lengths in an Ultracold Bose Gas”. In: *Phys. Rev. Lett.* 113 (2014), p. 053202.

[60] Y. Yudkin, R. Elbaz, P. Giannakeas, C. H. Greene, and L. Khaykovich. “Coherent Superposition of Feshbach Dimers and Efimov Trimers”. In: *Phys. Rev. Lett.* 122 (2019), p. 200402.

[61] Y. Yudkin, R. Elbaz, J. P. D’Incao, P. S. Julienne, and L. Khaykovich. “Reshaped three-body interactions and the observation of an Efimov state in the continuum”. In: *Nature Communications* 15.1 (2024), p. 2127.

[62] N. Gross, Z. Shotan, S. J. J. M. F. Kokkelmans, and L. Khaykovich. “Nuclear-spin-independent short-range three-body physics in ultracold atoms”. In: *Phys. Rev. Lett.* 105 (2010), p. 103203.

[63] S. E. Pollack, D. Dries, and R. G. Hulet. “Universality in three- and four-body bound states of ultracold atoms”. In: *Science* 326 (2009), p. 1683.

[64] P. Dyke, S. E. Pollack, and R. G. Hulet. “Finite-range corrections near a Feshbach resonance and their role in the Efimov effect”. In: *Phys. Rev. A* 88 (2013), p. 023625.

תקציר

התזה הנוכחית מחולקת לשני חלקים עיקריים, כל אחד מהם מוקדש לחקירה של היבטים שונים במחקר של גזים אטומיים אולטרה-קרים. החלק הראשון מתאר את הפיתוח של מערך ניסוי חדש לייצור וחקר גזים אטומיים אולטרה-קרים של ליתיום בוזוני. העבודה הנוכחית כוללת בנייה ואופטימיזציה של מאט זימן עשוי ממגנטים קבועים שמייצר שדה מגנטי רוחבי, ותכנון מלכודת אופטית-מגנטית. החלק השני מתמקד בחקירת השפעת אורך פיזור הרקע על תרחיש Efimov לתהודות Feshbach צרות חופפות.

החלק הראשון מציג את התכן החדשני, האופטימיזציה וההרכבה של מבנה מאט Zeeman מסוג spin flip העשוי ממגנטים קבועים, שנחשב למרכיב מרכזי בייצור ובמחקר של גזים אטומיים אולטרה-קרים. שיטות מסורתיות להאטת אלומות אטומיות לקירור ולכידה מסתמכות לרוב על סלילים חשמליים נושאי זרם הדורשות קירור מתמשך באמצעות מים. הגישה שלנו שונה בכך שמאט ה Zeeman מבוסס על מגנטים קבועים, דבר המבטל את הצורך בהספקת חשמל וקירור באמצעות מים, ובכך מפשט את המורכבות התפעולית ודרישות התחזוקה. התכן המוצע מקל על תחזוקת הוואקום בכך שהוא מאפשר הרכבה ופירוק קל של מאט Zeeman.

בהתמקדות באטומי ^{7}Li, מאט ה-Spin Flip Zeeman שפיתחנו מסוגל להפחית ביעילות את המהירות של קרן אטומית חמה מכמה מאות מטרים לשנייה לעשרות מטרים לשנייה. הפחתה משמעותית זו במהירות משפרת את יעילות הטעינה וממקסמת את מספר האטומים שניתן להשיג בתוך מלכודת מגנטו-אופטית. שימוש בקונפיגורציית Halbach למגנטים קבועים מבטיח שדה מגנטי חלק. ובנוסף ניתן לכוונן את השדה המגנטי הכללי על ידי הוספה אסטרטגית של טבעות Halbach מסביב למאט הזימן במידת הצורך.

יתרון מרכזי בגישתנו הוא קבלת שדה המגנטי יציב ומתכוונן בקלות, ומאפשר האטה בקרבת גבולות ההאטה התיאורטיים. דבר שמאפשר קבלת מערכת קומפקטית ויעילה יותר. בנוסף לכך השימוש בטכנולוגיית ההדפסה התלת-ממדית לבניית מאט ה-Zeeman, מאפשר השגת פתרון חסכוני שניתן להתאים אותו בקלות על ידי קבוצות מחקר אחרות לניסויים שונים של אטומים קרים. השימוש החדשני שלנו במגנטים קבועים סולל את הדרך להתקדמות עתידית ביצירת שדות מגנטיים אחידים ויציבים ביותר שנצטרך בהמשך סביב התא המדעי, המאפשרים השגת יציבות יוצאת דופן של פחות מ-1 מ"ג בתוך שדה מגנטי של 850 גאוס.

תוך שיתוף בתכנון ובתובנות המכאניות שלנו, אנו שואפים להקל על מאמצי מחקר רחבים יותר בתחום, לשפר את ההבנה והיישום של מערכות מבוססות מגנטים קבועים במחקרים אטומיים אולטרה-קרים. בנוסף, העבודה הנוכחית כוללת גם תכנון ואופטימיזציה של מלכודת מגנטו-אופטית.

החלק השני עוסק בפיזיקה של Efimov בקרבת שתי תהודות Feshbach צרות חופפות, אותן ניתן לחקור במסגרת מודל תלת-ערוצים שבו ערוץ פתוח שאינו מאפשר אינטראקציה מחובר לשני ערוצים מולקולריים סגורים. כאן, אנו קובעים כיצד הוא משתווה למודל דו-ערוצי מורחב, הכולל ערוץ פתוח עם פיזור רקע סופי וערוץ מולקולרי אחד. אנו מזהים את טווח הפרמטרים בו המודל התלת-ערוצים עולה על המודל הדו-ערוצי המורחב. בנוסף לכך אנחנו מרחיבים את מודל התלת-ערוצים כך שיכלול פיזור רקע, ואז שני המודלים מיושמים על מערכת הניסוי הרלוונטית של אטומי ליתיום בוזוני המקוטבים בשתי רמות אנרגיה שונות, עם תהודה מבודדת ושתי תהודות חופפות צרות של Feshbach, בהתאמה. אנו מאשרים, בהסכמה עם מחקרים קודמים, שבהיותו קטן, לאורכו של פיזור הרקע בליתיום יש השפעה זניחה על תכונות Efimov במקרה של תהודה מבודדת. לעומת זו, במקרה של תהודות Feshbach חופפות, הכללת פיזור רקע משפרת את ביצועי המודל התיאורטי ביחס למיקום תהודת Efimov הנמדד בניסוי.

תוכן עניינים

תקציר אנגלית **i**

1 הקדמה ומוטיבציה **1**

שדה רוחבי ממאט זימן ^{7}Li העשוי ממגנטים קבועים **5**

2 קירור ולכידת אטומים בלייזר 6

2.1 כוח ספונטני 6

2.2 קירור דופלר 7

2.3 היסט זימן 9

2.4 מאט זימן 10

2.5 מלכודת מגנטית אופטית 13

3 תכנון ובניית ניסוי בליתיום 16

3.1 רמות אנרגיה של ^{7}Li: מבנה ותכונות 17

3.2 תנור ליתיום: התפלגות מהירות 18

3.3 קצב טעינה 19

4 מאט זימן ממגנטים קבועים: תכנון וסימולציה 23

4.1 שדה מגנטי של תיבה העשויה ממגנט קבוע 23

4.2 סידור מרחבי של מגנטים קבועים 26

4.3 חישוב השדה המגנטי של המאט 29

4.4 תהליך האופטימיזציה של המאט 31

4.5 פרמטרים של השדה המגנטי המחושב 33

4.6 פרמטרים של השדה המגנטי האידיאלי 34

4.7 תוצאות האופטימיזציה 35

4.8 ניתוח הפרופילים של השדה המגנטי במאט זימן: אידיאלי לעומת מחושב 37

5 בניית מאט זימן: תכנון מכני ותוצאות המדידה של השדה המגנטי 40
5.1 תכן מכני 40
5.2 סטייות המדידה האפשריות של השדה המגנטי 46
5.3 השוואה בין השדה המגנטי הנמדד והשדה המחושב במאט זימן 47

6 בדיקה ואפיון של המאט: סימולציית מונטה-קרלו 50
6.1 פתרון נומרי לאורך ציר Z 52
6.2 פתרון נומרי כללי (תנועה תלת-מימדית) 54

7 ביצועי מאט זימן: מדידות המהירות 56
7.1 צפיפות אופטית 56
7.2 מערכת המדידה 57
7.3 תוצאות המדידה 59

8 מלכודת מגנטית אופטית 62
8.1 השדה המגנטי של לולאת זרם 62
8.2 קונפיגורציית סליל אנטי-הלמהולץ 62
8.3 תכן מלכודת מגנטית אופטית 63

השפעת פיזור הרקע על תרחיש Efimov של שני תהודות Feshbach צרות חופפות 66

9 משטרי תהודה בפיזיקה של גופים מעטים 67
9.1 תהודות Feshabch 67
9.2 תהודות Efimov 69
9.3 מודל דו-ערוצי 70

10 מודל תלת-ערוצים 74
10.1 פנומנולוגיה של מודל תלת ערוצים 74

10.2 המילטוניאן 74
10.3 מגזר דו-גופי 75
10.4 מגזר תלת-גופים: Efimov טרימר 77

11 מודל דו-ערוצי עם פיזור רקע 79
11.1 המילטוניאן 79
11.2 מגזר דו-גופי 80
11.3 מגזר תלת-גופים: Efimov טרימר 82

12 מודל דו-ערוצי עם פיזור רקע מול מודל תלת-ערוצים 85
12.1 הגדרה של מערכות המודל 85
12.2 קירוב של מערכות המודל על ידי מודל דו-ערוצי עם פיזור רקע 87
12.3 מגזר דו-גופי 88
12.4 מגזר תלת-גופים 89

13 מודל תלת-ערוצים עם פיזור רקע 91
13.1 המילטוניאן 91
13.2 מגזר דו-גופי 92
13.3 מגזר תלת-גופים: Efimov טרימר 94

14 תרחישי Efimov בליתיום בוזוני 96
14.1 ערוץ ^{7}Li bb 96
14.2 ערוץ ^{7}Li aa 99

15 סיכום ומסקנות 101

ביבליוגרפיה 103

תקציר עברית א

עבודה זו נעשתה בהדרכתו של

פרופ' לב חייקוביץ

מן המחלקה לפיסיקה

של אוניברסיטת בר-אילן.

פיתוח מאט זימן עשוי ממגנטים קבועים וחקירת השפעת פיזור הרקע על תרחישי אפימוב

חיבור לשם קבלת התואר "דוקטור לפילוסופיה"

מאת:

פאטמה חמודה-גזאל

המחלקה לפיזיקה

הוגש לסנט של אוניברסיטת בר-אילן

רמת גן   אייר, תשפ"ד